

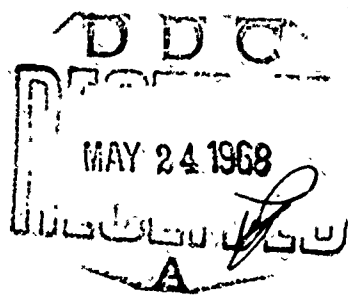
AD 669217



# BOEING



"DISTRIBUTION OF THIS DOCUMENT IS UNLIMITED: IT MAY BE  
RELEASED TO THE GENERAL PUBLIC.



**COMMERCIAL  
AIRPLANE DIVISION**

Reproduced by the  
**CLEARINGHOUSE**  
for Aeronautical Scientific & Technical  
Information Springfield, VA 22151

AD 669 217

**TEST RESULTS FROM THE BOUNDARY LAYER FACILITY  
(THEORY AND EXPERIMENTAL COMPARISON)**

L. Maestrello

Boeing Company  
Renton, Washington

11 May 1966

AD 669217

REV LTR

THE **BOEING** COMPANY

AIRPLANE DIVISION  
P.O. BOX 787  
RENTON, WASHINGTON 98055

CODE IDENT. NO. 81285

NUMBER D6-9944 - VOL. III

TITLE: TEST RESULTS FROM THE BOUNDARY LAYER FACILITY  
(THEORY AND EXPERIMENTAL COMPARISON)

FOR LIMITATIONS IMPOSED ON THE USE OF THE INFORMATION  
CONTAINED IN THIS DOCUMENT AND ON THE DISTRIBUTION  
OF THIS DOCUMENT, SEE LIMITATIONS SHEET.

MODEL \_\_\_\_\_ CONTRACT \_\_\_\_\_  
ISSUE NO. 52 ISSUED TO: ADL

"DISTRIBUTION OF THIS DOCUMENT IS UNLIMITED: IT MAY BE  
RELEASED TO THE GENERAL PUBLIC.

PREPARED BY	<u>L. Mastrolia</u>	<u>5/11/66</u>
SUPERVISED BY	<u>J. Mastrolia</u>	<u>5/12/66</u>
APPROVED BY	<u>J. B. Lange</u>	<u>5/12/66</u>
APPROVED BY	<u>F. S. Holman</u>	<u>5/13/66</u>

**LIST OF ACTIVE PAGES**

SECTION	PAGE NUMBER	REV SYM	ADDED PAGES						SECTION	PAGE NUMBER	REV SYM	ADDED PAGES					
			PAGE NUMBER	REV SYM	PAGE NUMBER	REV SYM	PAGE NUMBER	REV SYM				PAGE NUMBER	REV SYM	PAGE NUMBER	REV SYM		
	Title								22								
	A								23								
	B								24								
	C								25								
	1								26								
	2								27								
	3								28								
	4								29								
	5								30								
	6								31								
	7								32								
	8								33								
	9								34								
	10								35								
	11								36								
	12								37								
	13								38								
	14								39								
	15								40								
	16								41								
	17								42								
	18								43								
	19								44								
	20								45								
	21								46								

REV SYM

TD 4572B

**BOEING**

NO. D6-9944 - VOL. III

PAGE

A

6-7000

**LIST OF ACTIVE PAGES**

SECTION	PAGE NUMBER	REV SYM	ADDED PAGES						SECTION	PAGE NUMBER	REV SYM	ADDED PAGES					
			PAGE NUMBER	REV SYM	PAGE NUMBER	REV SYM	PAGE NUMBER	REV SYM				PAGE NUMBER	REV SYM	PAGE NUMBER	REV SYM		
	47								72								
	48								73								
	49								74								
	50								75								
	51								76								
	52								77								
	53								78								
	54								79								
	55								80								
	56								81								
	57								82								
	58								83								
	59								84								
	60																
	61																
	62																
	63																
	64																
	65																
	66																
	67																
	68																
	69																
	70																
	71																

REV SYM  
TD 4572B

REVISIONS			
LTR	DESCRIPTION	DATE	APPROVAL

SHEET C

TABLE OF CONTENTS

	Page
SUMMARY	2
LIST OF FIGURES	3
LIST OF TABLES	5
REFERENCES	6
NOMENCLATURE	9
TEST RESULTS FROM THE BOUNDARY LAYER FACILITY (THEORY AND EXPERIMENTAL COMPARISON)	11
I Introduction	11
II Properties of the Wall Pressure Fluctuation	14
III Measurement of the Pressure Fluctuation	20
IV Structural Response to a Turbulent Boundary Layers	23
A. Response of Simple Panels	23
B. Theoretical Approach	24
C. Example	29
V Experimental Results on the Reflection and Transmission of Flexural Wave on the Panel	32
VI Radiation of Sound from Flexible Panel	33
VII Radiation of Sound from Honeycomb Panels	35
VIII Contribution of Panel Boundaries to Sound Power Radiation	36
IX Effect of Cabin Pressurization on the Response of a Sidewall Panels	38
X Conclusions	38
APPENDICES	40
Appendix A	40
Appendix B	41
FIGURES	51
TABLES	83

## SUMMARY

The problem of acoustic radiation of panels excited by random pressure fluctuation of the turbulent boundary layer has been further investigated. In the past, experimental investigators have concentrated only on certain phases of the general problem; for example, the statistical behavior of the pressure field (Ref. 1), or the motion of the panel (Ref. 26). Recently the author presented a comprehensive set of experimental results (Refs. 4 and 5) that include all statistical information concerning both the forcing function; that is, pressure fluctuation and the response functions of the panel motion as well as the radiation field.

The main purpose of this paper is to show by using a relatively simple functional representation of the space-time correlation of the wall pressure fluctuation, and by the use of Lyons-Dyer method (Ref. 20), that motion and radiation intensity of a simply-supported panel agree reasonably well with the author's experimental results.

The most striking feature of the excitation mechanism is the so-called coincidence which has profound effects on the response of the structure and power radiations. If, under certain conditions, a mismatch occurs between wave speeds on the panel and the pressure field, panel displacement and acoustic radiation should be reduced. Such a mismatch is caused by a turbulence pressure eddy which decays faster than the mode's wavelength on the structure.

LIST OF FIGURES

<u>Figure</u>	<u>Title</u>	<u>Page</u>
1	Moving Frame Spectrum and Eddy Lifetime . . . . .	51
2	Dimensionless Power Spectrum and Auto-Correlation of the Wall Pressure Fluctuations . .	52
3	Comparison of the Co-power Spectral Density, $M = 0.52$ , $\delta^* = 0.155$ In., $R_h = 6.5 \times 10^5$ . . . . .	53
4	Comparison Between Co-quad - Absolute Power Spectral Density . . . . .	54
5	Map of Longitudinal Cross Power Spectrum Density.	55
6	Contour Map of the Longitudinal Cross Power Spectrum Density From Theory . . . . .	56
7	Total Pressure Probe . . . . .	57
8	Total Pressure Fluctuation . . . . .	58
9	Power Spectra of Total and Wall Pressures . . . . .	59
10	Wall Pressure Fluctuation on the 727 Airplane . .	60
11	Wall Pressure Fluctuations . . . . .	61
12	Mean Square Displacement of 12" x 7" x 0.040" Simple Supported Panel From Theory . . . . .	62
13	Mean Square Displacement of 12" x 7" x 0.040" Panel . . . . .	63
14	Mean Square Displacement From Measure of 36" x 6.5" x 0.040" Panel . . . . .	64
15	Mean Square Displacement From Theory of a 36" x 6.5" x 0.040" Panel . . . . .	65
16	Broadband Displacement Space-Time Correlation, $M = 0.52$ , $\delta^* = 0.155$ Inch . . . . .	66
17	Longitudinal Space-Time Correlation of the Displacement of a 36" x 6.5" x 0.040" Panel ( $\gamma = 0.34$ ) . . . . .	67
18	Experimental Co-power Spectral Density for Turbulence and Panel, $M = 0.52$ , $\delta^* = 0.155$ Inch, $R_h = 6.5 \times 10^5$ . . . . .	68

<u>Figure</u>	<u>Title</u>	<u>Page</u>
19	Displacement of a 36" x 6.5" x 0.040" Panel With Downstream End Damped ( $M = 0.34$ ) . . . . .	69
20	Correlation Across a Stringer and Correlation Between Stringers . . . . .	70
21	Modal Radiation in K-Space . . . . .	71
22	Sound Power Level for 36" x 6.5" x 0.040" Panel $M = 0.47$ , $M = 0.30$ . . . . .	72
23	Sound Power Level for 36" x 6.5" x 0.080" Panel $M = 0.52$ . . . . .	73
24	Sound Power Level of 36" x 6.5" x 0.040" Panel With Two Equally Spaced Stringers, $M = 0.47$ . . . . .	74
25	Sound Power Level for 7" x 12" Panels at $M =$ $0.47$ . . . . .	75
26	Total Acoustic Power (7" x 12" Panels) . . . . .	76
27	Total Acoustic Power (36" x 6.5" Panels) . . . . .	77
28	Total Acoustic Power (36" x 6.5" Panels) . . . . .	78
29	Sound Power Level for 36" x 6.5" x 0.040" Panel $M = 0.47$ . . . . .	79
30	Effects of Cabin Pressurization of SPL and Skin Acceleration (1/3 Octave Band) . . . . .	80
31	Space-Time Correlation of the Wall Pressure . . . . .	81

LIST OF TABLES

<u>Table</u>	<u>Title</u>	<u>Page</u>
1	Eigenvalues for 36" x 6.5" Panels With Rigid Boundary . . . . .	82

REFERENCES

1. Wilmarth and Wooldridge, "Measurements of the Correlation Between the Fluctuating Velocities and the Fluctuating Wall Pressure in a Thick Turbulent Boundary Layer," AGARD Report 456, April 1963.
2. Hodgson, T. H., "Pressure Fluctuation in Shear Flow Turbulence," College of Aeronautics Note 129, 1962.
3. Bull, M. K. and J. C. Willis, "Some Results of Experimental Investigations of the Surface Pressure Fields Due to a Turbulent Boundary Layer," University of Southampton AASU Report 199, 1961.
4. Maestrello, L., "Measurement of Noise Radiated by Boundary Layer Excited Panels," Journal of Sound and Vibration, 2, 1965.
5. Maestrello, L., "Measurements and Analysis of the Response Field of Turbulent Boundary Layer Excited Panels," Journal of Sound and Vibration, 2(3), 1965.
6. Serafini, J. S., "Wall Pressure Fluctuations and Pressure Velocity Correlation in a Turbulent Boundary Layer," NASA TR-R-165, 1963.
7. Hodgson, T. H. and G. M. Lilley, "On the Surface Pressure Fluctuation in Turbulent Boundary Layer," AGARD Report No. 276, April 1960.
8. Kistler, A. L. and W. S. Chen, "The Fluctuating Pressure Field in a Supersonic Turbulent Boundary Layer," Jet Propulsion Laboratory TR 32-277, 1962.
9. Corcos, G. M., "Pressure Fluctuation in Shear Flows," University of California Institute of Engineering Research Report Series 183, No. 2, July 1962.
10. Wills, J. A. B., "On Pressure Fluctuations Under Turbulent Boundary Layers," National Physical Laboratory AERO Report 1131, December 1964.
11. Kraichnan, R. H., "Noise Transmission From Boundary Layer Pressure Fluctuations," Journal of the Acoustical Society of America, Vol. 29, No. 65, 1957.
12. Ffowcs-Williams, J. E., "Surface Pressure Fluctuations Induced by Boundary Layer Flow at Finite Mach Numbers," Journal of Fluid Mechanics, Vol. 22, Part 3, 1965.
13. Ribner, H. S., "Boundary Layer Induced Noise in the Interior of Aircraft," UTIA Report 37, 1965.
14. Corcos, G. M. and H. W. Liepmann, "On the Transmission Through a Fuselage Wall of Boundary Layer Noise," Douglas Aircraft Company Report SM 19570, 1958.

15. Dyer, I. , "Sound Radiated into a Closed Space From Boundary Layer Turbulence," Bolt, Beranek and Newman Report 620, 1958.
16. Powell, A. , "On the Fatigue Failure of Structures Due to Vibrations Excited by Random Pressure Fields," The Journal of the Acoustical Society of America, December 1958.
17. Rattayya, J. V. and M. C. Junger, "Flow Excitation of Cylindrical Shell and Associated Coincidence Effects," Journal of the Acoustical Society of America, Vol. 36, No. 5, 1964.
18. Lvamshev, L. M. , "Sound Radiation From Elastic Shells Excited by Turbulent Aerodynamic Flow," Soviet Phys. - Acoust., Vol. 7 No. 1, 1961.
19. Lyon, R. H. , "Boundary Layer Noise Response Simulation With a Sound Field," Acoustic Fatigue in Aerospace Science, Syracuse University Press, 1965.
20. Lambert, R. F. and D. H. Tucker, "Response of Bars and Plates to Boundary Layer Turbulence," Journal of Aerospace Sciences, Vol. 29, 1962.
21. el Baroudi, M. Y. , Turbulence Induced Panel Vibrations, UTIAS Report 98, 1964.
22. Lyon, R. H. , "Response of String to Random Noise Field," Journal of the Acoustical Society of America, Vol. 28, No. 5, May 1956.
23. White, P. H. , "The Transduction of Boundary Layer Noise by Rectangular Panels," Journal of the Acoustical Society of America, (To be Published).
24. Maestrello, L. , The Effect of Length and Thickness on the Panel Response Due to Turbulent Boundary Layer Excitation, Presented at the 5th International Congress of Acoustics, Liege, Belgium, September 1965.
25. Maidanik, G. , "Response of Ribbed Panels to Reverberant Acoustic Fields," Journal of the Acoustical Society of America, Vol. 34, 1962.
26. Lyon, R. H. and G. Maidanik, Statistical Methods in Vibration Analysis, AIAA Journal, 2, 1964.
27. Smith, P. W. , Jr. , "Response and Radiation of Structural Modes Excited by Sound," Journal of the Acoustical Society of America, Vol. 24, 1962.
28. Phillips, O. M. , "On the Generation of Waves by Turbulent Wind," Journal of Fluid Mechanics, Vol. 2, No. 417, 1957.
29. Phillips, O. M. , "On the Generation of Sound By Supersonic Turbulent Shear Flow," Journal of Fluid Mechanics, Vol. 9, No. 1, 1960.

30. Ribner, H. S. , Aerodynamic Sound From Fluid Dilations, UTIA Report No. 86, 1962.
31. Ffowes-Williams, J. E. , The Noise From Turbulence Convected at High Speed, Phil. Trans. Roy. Soc. (London) A 255, 469, 1963.
32. Laufer, J. , Aerodynamic Noise in Supersonic Wind Tunnel, J. Aerospace Sciences, Vol. 28, No. 685, 1961.
33. Nikiforov, A. S. , "Radiation From a Plate of Finite Dimensions With Arbitrary Boundary Conditions," Soviet Physics Acoustics, Oct-Dec, 1964.
34. Warburton, G. B. , "The Vibration of Rectangular Plates," Proc. Instn. Mech. Engrs. London 186, 371, 1954.
35. Apostol, T. M. , Mathematical Analysis, Addison Wesley, 1957.
36. Fuller, J. R. , A Theoretical Approach for the Determination of Acoustic Transmission Losses Through Loaded Rectangular Skin Panels. Boeing Technical Note D6-7606 TN, February 1964.

## NOMENCLATURE

$A_{m,n}$	- plate model damping
a, b	- lengths of panel sides
A, K, N	- constant
B	- bending stiffness
E	- Young's modulus
f or $\omega$	- frequency ( $\omega = 2\pi f$ )
h	- panel thickness
K	- wave number
m, n	- mode number
M	- Mach number
$m_0$	- plate mass
$\sqrt{\frac{2}{\rho}}$	- rms wall pressure fluctuations
P( )	- power spectral density of the wall pressure fluctuations
PWL	- total sound power level
R( )	- correlation coefficient
U	- free stream velocity
$U_c$	- convection velocity
x, y	- coordinates
Y	- panel displacement
$\theta$	- eddy lifetime
$\phi$	- wave form
$\delta^*$	- boundary layer displacement thickness
$\tau = t - t'$	- time delay
$\eta = y - y'$	- lateral partial separation

- $\xi$   $y - y'$  - longitudinal partial separation
- $\tau_w$  - wall shear stress
- $\sigma$  - standard deviation
- $\beta_{AC}, \beta_{ST}$  - acoustic and structural damping
- $\Gamma_{m,n}$  - eigenvalue
- $\delta_{m,n}$  - total damping ratio

TEST RESULTS FROM BOUNDARY LAYER FACILITY  
(THEORY AND EXPERIMENTAL COMPARISON)

1. INTRODUCTION

The exterior surface of an aircraft is excited directly by turbulence as well as by sound generated by the turbulent boundary layer. The aircraft skin is flexible and the fluctuating pressure in the boundary layer (forcing field) causes the surface to vibrate. This surface vibration acts as a radiator of sound. Measurements of the wall pressure fluctuation, panel response, and acoustic radiation characteristics of typical panels have been reported by many investigators. The intention in this paper is to discuss some of these measurements (primarily those made by the author) and to develop a theoretical model for comparison with experiments.

Consider the surface pressure fluctuation, since the fluctuation force on the wall in any frequency band causes the panel structure to vibrate at wavelengths of the order of the scale of the pressure field. Typical wall pressure power spectra and correlation fields can be seen in Refs. 1 through 7 for subsonic flow and in Ref. 8 for supersonic flow. These data show that the mean square pressure fluctuation is a slowly varying function of Mach number. These spectra are in good agreement for Strouhal numbers  $\omega\delta^+ / U > 0.2$ . At lower values, the various measurements do not agree well. The differences in results, may possibly be due to variations in Reynolds number or Mach number or to extraneous noise. It is not possible to find the characteristic length and velocity that eliminates the Reynold's number effect. Reference 9 shows for instance that the ratio  $\sqrt{p^2} / \tau_w$  approaches a constant only for very high Reynold's number. Furthermore, the non-dimensional power spectrum  $p(\omega)U / \tau_w^2 \delta^+$  shows similar behavior only in a limited nondimensional wave number range. The Mach number range of the various experiments extend from zero to almost five, and it is not surprising that differences in the shape of the spectrum are found.

Interference at low frequencies due to extraneous noise sources is commonly encountered in wind tunnel facilities. The cause of this noise in the various types of wind tunnels depends on type of blower system and on the air control, and installation environment. In the present test facility, 15 feet of acoustic muffler are used ahead of the settling chamber. Each component is mounted on an independent concrete pad floating on sand. However, interference still occurs at frequencies of 100 cps and lower and varies somewhat with the flow speed and diffuser setting (Ref. 4). Evidence of acoustic interference is shown by the narrow band spatial correlation measurements of the wall pressure made at low frequencies (Ref. 10). These measurements clearly show a very strong acoustic pressure superimposed on the turbulent pressure. It may only be practical to limit low frequency power spectrum measurements to flight tests.

The response of panels to turbulence has also been the subject of various papers from both experimental and theoretical aspects (Refs. 11 to 23). These papers are concerned primarily with the vibration correlation response near the free bending wave length of the panel, which accounts for most of the excitation. Theory in Ref. 16 is based on the acceptance of the pressure field by the beam, indicating the influence on the displacement response and, hence, the stress of the structure. These resonant effects of matching the bending wave number and frequency of the panel with the turbulence wave number and frequency (aero-dynamic coincidence) have been observed experimentally (Refs. 5, 20, 21, and 22). Reference 5 extends the experimental results for the conditions below and above coincidence both in terms of model displacement, panel stresses and acoustic radiation. Reference 21 includes a brief resumé of the behavior of the panel displacement obtained by space-time correlation over a complex panel. These results are associated with the measured total mean square displacement and total acoustic power radiated.

It turns out that the amount of energy fed into the structure will depend on the wave number component and amplitude of the pressure field. On the other hand, the amount of energy accepted by the structure will depend on how many structural modes the pressure field will excite. However, not all the energy accepted by the structure will be converted into displacement amplitude but will be partially dissipated internally and partially radiated back. This loss corresponds to the total damping consisting of acoustic and structural damping.

Finally, the acoustic power radiated has been the subject of considerable investigation, especially by the Bolt, Beranek, and Newman Corporation (Refs. 25 to 27). Their analysis has shown that the sound power radiated from a reverberant field for simply-supported panels is proportional to the perimeter of the panel for vibration up to the critical frequency. When comparing simply-supported or clamped boundaries, it was found that the clamped case was the most efficient radiator. Measurements of the acoustic damping for various modes of vibration have been made and reported by the author, (Ref. 4). The change in radiated power with velocity has shown the effect of aerodynamic coincidence, as well as a marked cancellation effect which reduces the acoustic power law from a  $M^5$  to a  $M^{2.3}$  dependence. The change is caused by a progressive increase in wave number for coincidence where a similar wave number of the panel mode becomes larger than the corresponding wave number of the turbulent pressure field.

Owing to the complexity of the problem, a measured input covariance was used in predicting panel response due to turbulence. The panel is flat, rectangular and has either simply-supported or clamped edges. The vibration of the surface is coupled to the turbulent pressure field beneath the panel and to the radiation field.

## II. PROPERTIES OF THE WALL PRESSURE FLUCTUATION

We have proposed in the previous work Ref (5) two functional representations of the wall pressure covariances based on experimental observations of data from a turbulent channel flow. Since the structural panel is excited randomly, i. e. by turbulence, the flow model is useful in studying coupling between the wall pressure and the panel surface. The model consists of a convected wall pressure pattern with space and time dependence. It retains the characteristics of the superposition of a wave system with phase and amplitude related to wave number and frequency spectrum. This model may not be sufficiently rigorous to insure a detailed description of the flow field, but it proves to be useful in describing the response of the panel structure to turbulence because it provides a means for studying the effect of pressure fluctuations on the motion of the panel.

The representation chosen here to describe the wall pressure fluctuation in a moving frame is given by the linear combination of two Gaussian distributions, each of which has a maximum value that decays in time and changes in separation with time. The behavior in the moving frame reference of the cross-correlation function  $R(\xi, \eta, \tau)$  has been represented by:

$$R(\xi, \eta, \tau) = \frac{\langle p(x, y, t) p(x+\xi, y+\eta, t+\tau) \rangle}{p^2}$$

$$= e^{-\frac{|\xi|}{U_c \theta}} \left\{ \Lambda_1 e^{-\left[ \frac{(\xi - U_c \tau)^2 + \eta^2}{2\sigma_1^2} \right]} + \Lambda_2 e^{-\left[ \frac{(\xi - U_c \tau)^2 + \eta^2}{2\sigma_2^2} \right]} \right\} \quad (1)$$

After decomposing each individual correlation  $R(\xi, \eta, \tau)$  into two Gaussian distributions, an "upper" one and a "lower" one, a single decay rather than an individual decay for each of the Gaussian distributions was used. The decay of the cross-correlation is given by  $\exp(-|\xi|/U_c \theta)$  rather than by  $\exp(-|\tau|/\theta)$ , as in the previous

\*Appendix A discussed the choice using one of two forms of decay.

paper. The panel does not respond similarly for all frequencies and wave numbers of the turbulence; certain combinations of wave number and frequency are excited more strongly than others. When the wall pressure matches both the wave number and the frequency of a particular panel mode, a condition called coincidence occurs. This results in a very strong excitation of running flexural waves on the panel. Then the amplitudes of any Fourier components of the panel displacement depend on the amplitudes of the characteristic lengths of the pressure fields,  $U_c \theta$ . The characteristic length or correlation length is a function of both wave number and frequency, implying that  $U_c(K_1, \omega)$ . The moving frame spectrum shows that a very uniform energy content up to the wave number  $K_1 = 1/U_c \theta$  exists, beyond which the energy diminishes rapidly. The following spectrum was obtained from a Fourier transform of the envelope of the correlation maxima  $\exp -|\xi|/U_c \theta$ . Figure 1 shows the eddy lifetime and the moving frame spectrum.

$$P(K_1, U_c) = \frac{U_c \theta}{\pi} (1 + K_1^2 U_c^2 \theta^2)^{-1} \quad (2)$$

The equivalent representation in terms of the wave number and frequency spectrum is obtained from the triple Fourier transform.

$$P(K_1, K_2, \omega) = \frac{1}{(2\pi)^3} \iiint_{-\infty}^{\infty} R(\xi, \eta, \tau) e^{-i(K_1 \xi + K_2 \eta + \omega \tau)} d\xi d\eta d\tau \quad (3)$$

The problem is to integrate (3). Let us first obtain from (1) the power spectrum.

$$P(\theta, \omega) = \frac{\Lambda_1 \sigma_1}{U_c \sqrt{2\pi}} e^{-\frac{\sigma_1^2 \omega^2}{2U_c^2}} + \frac{\Lambda_2 \sigma_2}{U_c \sqrt{2\pi}} e^{-\frac{\sigma_2^2 \omega^2}{2U_c^2}} \quad (4)$$

and the autocorrelation

$$R(\theta, \theta, \tau) = \Lambda_1 e^{-\left(\frac{U_c \tau^2}{2\sigma_1}\right)^2} + \Lambda_2 e^{-\left(\frac{U_c \tau^2}{2\sigma_2}\right)^2} \quad (5)$$

The power spectrum of equation (4) is plotted in Fig. 2 and compared with the measured spectrum. A good fit is obtained at the lower frequencies for  $\omega \delta^+ / U < 1.5$ ; at the higher frequencies the Gaussian spectrum distribution falls off much faster than the measured spectrum. These differences in the power spectrum were discussed previously in Ref. 5 where an exponential space-time correlation was obtained containing higher frequency components than the model described by Eq. 1. Also a comparison is made in Fig. 2 between the measured autocorrelation and the one described in equation (5).

From equations (1) and (3), the longitudinal cross spectral density becomes:

$$P(K_1, \theta, \omega) = \frac{P(\omega)}{2\pi} \left\{ \left[ \frac{1/U_c \theta}{(1/U_c \theta)^2 + (\omega/U_c + K_1)^2} + \frac{1/U_c \theta}{(1/U_c \theta)^2 + (\omega/U_c - K_1)^2} \right] - i \left[ \frac{\omega/U_c + K_1}{(1/U_c \theta)^2 + (\omega/U_c + K_1)^2} - \frac{\omega/U_c - K_1}{(1/U_c \theta)^2 + (\omega/U_c - K_1)^2} \right] \right\} \frac{P(\omega)}{2\pi} (\alpha - i\beta) \quad (6)$$

Since the cross spectral density is complex, giving information about the amplitude and phase, equation (6) can also be written as

$$P(K_1, 0, \omega) = |P(K_1, 0, \omega)| e^{-i\phi(K_1, \omega)} \quad (6')$$

Then the phase angle is given by

$$\phi(K_1, 0, \omega) = \tan^{-1} \beta/\alpha \quad (7)$$

Similarly, the lateral spectral density

$$P(0, K_2, \omega) = \frac{A_1 \sigma_1^2}{2\pi U_c} e^{-\sigma_1^2 \omega^2 / 2U_c^2} e^{-\sigma_1^2 K_2^2 / 2} + \frac{A_2 \sigma_2^2}{2\pi U_c} e^{-\sigma_2^2 \omega^2 / 2U_c^2} e^{-\sigma_2^2 K_2^2 / 2}$$

On combining (6) and (8), one obtains the two dimensional cross power spectrum  $P(K_1, K_2, \omega)$  between the vectors  $K_1$  and  $K_2$ .

The cross power spectral density shows the rate of transfer of energy from small to large wave numbers. The most coherent pattern of the pressure eddy moves with the convection velocity at different frequencies and wave numbers. Useful definition of the convection velocity has been given by Refs. 12 and 28, where it is shown that the integral time scale is the maximum in the frame of reference moving downstream with this velocity. Since only the lateral correlation shows no moving axis,  $\exp(-\eta/U_c \theta) = 1$ ; the time scale  $\theta$  is constant and very small along  $\eta$  axes. In all other components, the value of  $\theta$  is large. The eddy lifetime  $\theta$  were assumed to correspond to the time in which the value of the correlation coefficient obtained from the envelope of the correlation

maxima dropped to  $1/e$ . Since it is known that the convection velocity is not the same for different wavelengths and frequencies, it is convenient to define a convection velocity  $\omega_0/K_1^* = U_c^*(\omega_0, K_1^*)$  such that when  $K_1 = K_1^*$ , then  $|P(K_1, 0, \omega)|^2$  is a maximum.

The magnitude of the spectrum given by Eq. 6 is:

$$|P(K_1, 0, \omega)|^2 = \frac{[P(\omega)]^2}{(2\pi)^2} \frac{4 U_c^2 \theta^2 (1 + \omega^2 \theta^2)}{\left[1 + \omega^2 \theta^2 (1 + U_c K_1 / \omega)^2\right] \left[1 + \omega^2 \theta^2 (1 - U_c K_1 / \omega)^2\right]} \quad (9)$$

By maximizing  $|P(K_1, 0, \omega)|^2$  with respect to  $K_1$ , where  $U_c$  and  $\theta$  are constant. We observed the following:

$$|P(K_1, 0, \omega)|_{\max}^2 = \begin{cases} |P(\omega)|^2 (4 U_c^2 \theta^2); & \text{at } K_1^* = 0 \text{ when } \omega\theta = 0 \\ |P(\omega)|^2 \frac{4}{(1/U_c \theta)^2 + (\omega/U_c)^2}; & \text{at } K_1^* = 0 \text{ when } \omega\theta < 1 \\ |P(\omega)|^2 \frac{2 U_c^2 \theta^2}{(2\pi)^2}; & \text{at } K_1^* = 0 \text{ when } \omega\theta = 1; \\ |P(\omega)|^2 U_c^2 \theta^2 \frac{1 + \omega^2 \theta^2}{\omega\theta \sqrt{\omega^2 \theta^2 - 1}} & \text{at } K_1^* = \sqrt{\omega^2 / U_c^2 - 1} / U_c \theta^2 < \frac{\omega}{U_c}, \text{ and when } \omega\theta > 1; \end{cases} \quad (10)$$

From (10) the convection velocity  $U_c^*$  is given by:

$$U_c^* = U_c \sqrt{\frac{\omega^2 \theta^2}{\omega^2 \theta^2 - 1}}$$

The first three conditions simply mean that the notion of convection velocity is not a useful concept. It is of considerable significance that in the region  $\omega\theta \gg 1$  the peak amplitude varies like  $K_1^{\dagger} \approx \omega/U_c$ . In this case  $U_c = U_c^{\dagger}$ . It can be seen that the convection velocity increases rapidly with decreasing wavenumber until its speed relative to the free stream velocity will be larger than the sound velocity. This region corresponds to the Mach wave radiation discussed in Refs. 29 through 32.

A plot of the measured (real part) one-dimensional wave number spectrum is shown in Fig. 3. It is compared with the real part of Equation (6). The measured real part is obtained by the Fourier transform of the narrow band spatial correlation which also gives the phase information. The differences in the lower frequency region are due to variation in  $U_c^{\dagger}$ ; at high frequencies the differences are introduced by a measuring technique which uses a wider effective bandwidth filter.

Figure 4 shows the computation of the real, imaginary, and absolute value of the longitudinal spectrum. The phase information is obtained from the ratio of the real and imaginary part. This figure shows that energy decreases with increasing frequency and wave number. Furthermore, it can be seen that in the lowest wave number region there exists a noticeable difference between the maximum of the absolute value of the spectrum and that of the real part.

Figure 5 clearly shows that the average convection velocity corresponds to that range of wave numbers where the disturbances are coherent ( $U_c^{\dagger} = \text{constant}$  independent of wave number). On the other hand, the lowest wave number disturbances are incoherent, moving with significantly different convection velocity. The results summarized in Fig. 5 confirm the conjecture of Ref. 32 that the lowest wave number disturbance can produce Mach wave radiation even in a subsonic boundary layer. Figure 6 shows the region of supersonic and subsonic wave velocity.

### III. MEASUREMENT OF THE PRESSURE FLUCTUATION

Either static pressure fluctuation at a wall or total pressure in the stream have been measured. However, measurement of the stream total pressure fluctuation in a channel flow has been associated with the measurement of the wall pressure fluctuation. The total pressure fluctuation is useful in studying the impingement effect of the turbulent flow on the surface. It is also presently used to measure the radiated acoustic energy from the boundary layer by mounting the transducer in the unperturbed region of the free stream.

The sensing element in the total pressure transducer is a solid piezoelectric ceramic cylinder with an effective diameter of 0.04 in. It is mounted on a cone tip of a 3/16-inch diameter tube (Fig. 7). The signal output due to vibration of the transducer when mounted on the duct was found to be very small compared to the pressure signal. The vibration increase as the transducer was moved into the stream; however, up to an extension of 1.5 inches from the wall, the vibration output was considerably lower than the signal due to pressure fluctuations.

To facilitate the comparison of the wall pressure with the stream pressure fluctuations, the stream pressure transducers were made to be adaptable for flush mounting in the duct wall. It was ascertained that the measured wall pressure corresponds to the power spectrum distribution measured previously with different transducers. As expected, the root mean square stream pressure fluctuation is higher than the wall pressure (Fig. 8). The distribution of the pressure across the duct shows a maximum near the wall in the region of higher shear fluctuation. The pressure level decreased towards the center of the duct, indicating a behavior similar to that of the velocity fluctuation. Figure 9 is a plot of the stream pressure spectrum and wall spectrum. The stream pressure spectrum has a shape similar to the usual velocity spectrum.

Space-time correlation measurements of the wall pressure fluctuation were made over the fuselage skin of the 727 airplane to determine the wall pressure covariance to be used for structural and acoustic response study. The power spectrum distribution with frequency is similar to the one obtained previously, Reference 4, on the 707 prototype airplane. Considerable attention was given in the measurement of the lowest frequency region in an attempt to clarify the argument about the behavior of the power spectrum in this range.

Five Bruel and Kjaer Type 4136, 0.25-inch diameter microphones were mounted on 1/4-inch thick plates at various distances apart in the direction of flow. The plate was flush mounted on a cutout portion of the airplane panel above the wing level approximately 71 feet from the nose. In the vicinity of the transducers, a Preston tube was mounted on the plate for the local skin friction measurement.

The wall pressure spectra was recorded for frequencies as low as 20 cps and up to 20,000 cps. A typical spectrum is shown in Fig. 10 at Mach number 0.77. This power spectrum does not roll off with decreasing frequency like the Hodgson spectrum measurement over the wing of a glider (Ref. 2) for very low speed. The differences between spectrum on the 727 airplane and the one obtained in the Boeing boundary layer facility occurs at a lower frequency which shows that the duct spectrum slightly increases in amplitude while the airplane spectrum remains constant.

Figure 11 shows that the ratio of the root mean square pressure fluctuation with the wall shear stress plotted in terms of Mach number for the 727 airplane compares with the previous measurement in the duct flow and with the boundary layer flow of Refs. 1 and 7. As expected, the 727 data are slightly lower than the wind tunnel spectra because of bandwidth limitation of the instrumentation.

However, the overall picture shows the trend of the variation of the ratio

$\sqrt{\frac{\overline{p'^2}}{\tau_w}}$  with Mach number for relatively high Reynold's-number.

Since the study of the structural response to turbulence requires not only the mean square value of the pressure field but also the energy contained in a specific frequency band corresponding to a resonant frequency of the structural panel, the filter center frequency and the bandwidth has to be selected to fit the particular mode of interest. A narrow band spacial correlation measurement of the wall pressure reported in Ref. 5 has shown that the correlation coefficient has a unique dependendency on  $\omega\xi/U_c$  and it decays as  $\exp(-(|\xi|/U_c)\theta)$  for the longitudinal correlation equation obtained from (1) after taking the transform with respect to  $\tau$ ,

the longitudinal cross power spectrum becomes:

$$P(\xi, 0, \omega) = P(\omega) e^{-\frac{|\xi|}{U_c} \theta} \left[ \cos \frac{\omega\xi}{U_c} - i \sin \frac{\omega\xi}{U_c} \right] \quad (12)$$

The real part  $P(\xi, 0, \omega)_R$  is identical to experimental data obtained by a narrow band spacial correlation. The imaginary part can be obtained experimentally by shifting the phase of one signal 90-degrees at frequency  $\omega$  before correlating the two signals.

Assuming that the filter characteristics are constant within  $(\omega_1 - \Delta\omega$  to  $\omega_1 + \Delta\omega)$  and zero elsewhere, the amount of energy per bandwidth is related to the amount of energy per cycle by:

$$\int_{\omega_1 - \Delta\omega}^{\omega_1 + \Delta\omega} P(\xi, 0, \omega) d\omega = R_{\Delta\omega}(\xi, 0) \quad (13)$$

where

$$P(\xi, 0, \omega) = \frac{1}{2\pi} \int_{-\infty}^{\infty} R(\xi, 0, \tau) e^{-i\omega\tau} d\tau \quad (14)$$

The measured spectrum obtained from equation (13) can be compared with the single frequency spectrum of either equation 12 or 14.

#### IV. THE STRUCTURAL RESPONSE TO A TURBULENT BOUNDARY LAYER

Since the pressure field over the panel is responsible for generating the motion of the panel, which consists of a multimode vibration, a Fourier analysis in two space dimensions  $\xi$  and  $\eta$  and one time  $\tau$  dimension would determine how extensive is the influence of the pressure field in controlling the response of the panel. This response would not be uniform since certain combinations of wave numbers and frequencies in the component of the surface displacement are excited more than others (Ref. 5). The phase relationship for a particular frequency and wave number remains fixed so that the resultant excitation will continually grow causing a buildup of displacement wave amplitude inversely to the panel damping. The panel tends to respond with running wave ripples having trace speeds equal to the eddy convection speeds of the turbulent boundary layer (Refs. 13 and 14).

##### a. Response of Simple Panel

The vibration response of simple panels excited by turbulent boundary layers is considered. The panel loading is described by one of two models of the pressure covariances obtained from experimental data from turbulent channel flow (Ref. 5). Numerical computation of the response for simply supported panels has been made (Ref. 21) using an idealized model (Refs. 15 and 22) with pressure covariances having a delta function frequency spectrum with exponential decay. Since the results are qualitatively descriptive of the panel behavior in a convected field, it was felt that the improvement of this model by an accurate assessment of the pressure field may have a numerical importance on the prediction of the structures response to turbulence.

Since relatively large numbers of modes are present in a simple panel, the response behavior in each one of the modes depend on the flow characteristics ( $\omega$ ,  $K$ ,  $U_c$ , and  $\theta$ ) and on the panel characteristics ( $a$ ,  $b$ ,  $h$ ,  $a_{m,n}$  and  $E$ ). For certain combinations, only a few modes dominate the spectrum; for others, the overall response is controlled by relatively large numbers of modes. A practical example is given by 7 x 12 x .01 inch panels excited by flow Mach number  $M = 0.52$  with the boundary layer displacement thickness  $\delta^* = 0.155''$ . Results show that above the 6th mode ( $m = 6$ ,  $n = 1$ ) the response is so small that any contribution to the total response is negligible. Instead, for a longer

panel 36 x 6-1/2 x 0.04 inches at the same flow environment, the mean square of the 20th mode ( $m = 20, n = 1$ ) is only 2 decays below the first few modes. It is difficult and extremely lengthy in such situations to compute the response of each single mode. A model that is applicable for a large number of degrees of freedom becomes very useful.

For a practical airplane structure, a panel is divided into bays of panels with a frame stiffener around the edges and stringers along opposite edges. Preliminary measurements show that the response of such structures behaves as a running wave ripple, which favors the type of deformation corresponding to higher order modes. Each adjacent panel becomes independent. Previous work on multiple panels given in Ref. 24 shows that two adjacent panels separated by stringers are uncorrelated by running waves but correlated for low frequency modes corresponding mainly to those modes near the fundamental frequency of the entire bay of panels. This section of the paper is directed toward accurate assessment of the panel response to turbulence in terms of model shape, cross-spectral density, and mean square displacement.

#### b. Theoretical Approach

The correlation function of the displacement covariance due to a random force  $P(x_0, y_0, t_0)P(x'_0, y'_0, t'_0)$  has been given by Ref. 15.

$$\overline{Y(x, y, t)Y(x', y', t')} = \int_{-\infty}^t dt_0 \int_{-\infty}^{t'} dt'_0 \int_0^a dx_0 \int_0^b dy_0 \int_0^a dx'_0 \int_0^{b'} dy'_0 g(x, y, t | x_0, y_0, t_0) \cdot g(x', y', t' | x'_0, y'_0, t'_0) < \overline{p(x_0, y_0, t_0)p(x'_0, y'_0, t'_0)} > \quad (15)$$

The pressure covariance has been reported primarily in Ref. 5 for broad band response:

$$\langle p(x_0, y_0, t_0) p(x'_0, y'_0, t'_0) \rangle = p^2 e^{-\frac{(t_0 - t'_0)}{\theta}}$$

$$\cdot \left\{ \sum_{\nu=1}^3 \frac{A_\nu K_\nu}{K_\nu^2 + \left(\frac{1}{FU}\right)^2 \left[ (|x_0 - x'_0| - U_c |t_0 - t'_0|)^2 + (y_0 - y'_0)^2 \right]} \right\} / \sum_{\nu=1}^3 \frac{A_\nu}{K_\nu} \quad (16)$$

The plate input response function  $g(x, y, t | x'_0, y'_0, t'_0)$  was evaluated in terms of eigen-functions or orthogonal modes of plate oscillation which are of the form

$$Y_{m,n}(x, y, t) \sim \phi_{m,n}(x, y) \exp \left[ -a_{m,n} t + i\omega_{m,n} t \right] \quad (17)$$

The normal mode satisfied the equation:

$$B \nabla^4 Y(x, y, t) + \mathcal{M} \frac{\partial^2 Y(x, y, t)}{\partial t^2} + (\beta_{AC} + \beta_{ST}) \frac{\partial Y(x, y, t)}{\partial t} = 0 \quad (18)$$

it shows explicit division of the damping into acoustic and structural damping. Substituting (17) into (18),

$$\nabla^4 \phi(x, y) - \Gamma_{m,n}^4 \phi(x, y) = 0 \quad (19)$$

where

$$\Gamma_{m,n}^4 = \frac{\mathcal{M} (a_{m,n} + i\omega_{m,n})^2 - (\beta_{AC} + \beta_{ST}) (a_{m,n} + i\omega_{m,n})}{B} \quad (20)$$

and

$$a_{m,n} = \frac{\delta_{m,n} \omega_{m,n}}{2} \quad \omega_{m,n}^2 = \frac{B}{M} \Gamma_{m,n}^4$$

The impulse response function for low damping was found to be:

$$g(x,y,t|x_0,y_0,t_0) \propto \sum_{m,n} \frac{\phi_{m,n}(x,y)\phi_{m,n}(x_0,y_0)}{\omega_{m,n}} \cdot \exp \left[ -a_{m,n}(t-t_0) \sin \omega_{m,n}(t-t_0) \right] \quad (21)$$

and the eigenfunction solution to the homogeneous wave equation of the plate in the case of freely supported boundaries is

$$\phi_{m,n}(x,y) = \frac{2}{(ab)^{1/2}} \sin \frac{m\pi x}{a} \sin \frac{n\pi y}{b} \quad (22)$$

An attempt has been made to evaluate the integral (15) using two methods of integration; the Gaussian quadrature and the Monte Carlo method. The problem was too lengthy to handle with the standard interaction technique. After some survey, both the Monte Carlo method and the Gaussian quadrature methods proved unfeasible because an estimation of the maximum value of the integrand (over six dimensional space) is necessary, and the extreme demands on computer time made it impossible to proceed with this type of computation. Engineering judgement suggests that certain coupling terms may be eliminated in the integrand, thus, considerably reducing the time of integration. Both Dyer and el Baroudi use a relatively simple input response for pressure correlation. One can deduce in the case of the delta function, any term in the integral which includes the product of two identical eigenmodes effectively vanishes when the integration is performed.

With the present type of cross-correlation function, the closed form solution may be impossible or extremely lengthy using numerical computer techniques. Therefore, an assumption is made based on el Baroudi's results, that the cross-modal effect be eliminated. This reduces equation (15) to

$$\overline{Y(x, y, t) Y(x', y', t')} = \frac{\overline{p^2}}{\sum_{\nu=1}^3 \frac{A_{\nu}}{K_{\nu}}} \pi^2 \sum_{m,n} \frac{\phi_{m,n}(x, y) \phi_{m,n}(x', y')}{\omega_{m,n}^2}$$

$$\cdot \int_{-\infty}^t dt_0 \int_{-\infty}^{t'} dt'_0 \int_0^a dx_0 \int_0^b dy_0 \int_0^a dx'_0 \int_0^b dy'_0 e^{-\alpha_{m,n}(t-t'_0)} \left[ \sin \omega_{m,n}(t-t'_0) u(t-t'_0) \right]$$

$$\cdot e^{-|(t-t'_0)/\theta|} \left\{ \frac{\sum_{\nu=1}^3 \frac{A_{\nu} K_{\nu}}{K_{\nu}^2 + \left(\frac{1}{FU}\right)^2 \left[ \left( (x-x'_0) - U_c(t-t'_0) \right)^2 + (y_0-y'_0)^2 \right]} \right\} / \sum_{\nu=1}^3 \frac{A_{\nu}}{K_{\nu}}$$

(23)

By changing the variables of integration (see Appendix B), integral (23) is reduced to:

$$\overline{Y(x, y, t) Y(x', y', t')} = \frac{\overline{abp^2}}{2\pi^2 \sum_{\nu=1}^3 \frac{A_{\nu}}{K_{\nu}}} \pi^2 \sum_{m,n} \frac{\phi_{m,n}(x, y) \phi_{m,n}(x', y')}{m,n \omega_{m,n} (a_{m,n}^2 + \omega_{m,n}^2)}$$

$$\cdot \int_{-m\pi}^{m\pi} f(\bar{z}) \left[ \int_0^{n\pi} f(\bar{y}) \left[ \int_0^{\infty} g(\bar{x}) \sum_{\nu=1}^3 \left\{ \frac{A_{\nu} K_{\nu} e^{-|(\tau-\bar{x})|/\theta}}{K_{\nu}^2 + \left(\frac{1}{FU}\right)^2 \left[ \left( \left| \frac{a\bar{z}}{m\pi} - U_c \tau \right| + U_c \bar{x} \right)^2 + \left( \frac{b\bar{y}}{n\pi} \right)^2 \right]} \right. \right. \right]$$

$$\left. \left. \frac{A_{\nu} K_{\nu} e^{-|(\tau+\bar{x})|/\theta}}{K_{\nu}^2 + \left(\frac{1}{FU}\right)^2 \left[ \left( \left| \frac{a\bar{z}}{m\pi} - U_c \tau \right| - U_c \bar{x} \right)^2 + \left( \frac{b\bar{y}}{n\pi} \right)^2 \right]} \right\} d\bar{x} \right] d\bar{y} \right] d\bar{z}$$

(24)

where

$$f(\bar{z}) = \cos \bar{z} + \frac{1}{m\pi} (-|\bar{z}| \cos \bar{z} + \sin |\bar{z}|)$$

$$f(\bar{y}) = \cos \bar{y} + \frac{1}{n\pi} (\sin \bar{y} - \bar{y} \cos \bar{y})$$

$$g(\bar{x}) = e^{-a_{m,n}\bar{x}} \left[ \sin \omega_{m,n}\bar{x} + \frac{\omega_{m,n}}{a_{m,n}} \cos \omega_{m,n}\bar{x} \right]$$

It is easier now to obtain further information. The numerical result from (21) gives both the modal and broad band correlation.

The normalized correlation function is defined as

$$R_y(\xi, \eta, \tau) = \frac{Y(x, y, t) Y(x', y', t')}{\left[ Y(x, y, t)^2 Y(x', y', t')^2 \right]^{1/2}} \quad (25)$$

and the normalized cross power spectral density of the panel displacement,

$$\frac{P_y(K_1, K_2, \omega)}{P(\omega)} = \frac{1}{(2\pi)^3} \iiint_{-\infty}^{\infty} R_y(\xi, \eta, \tau) e^{-i(K_1\xi + K_2\eta + \omega\tau)} d\xi d\eta d\tau \quad (26)$$

The panel and turbulent spectra are related by

$$\left| \Gamma(K_1, K_2, \omega) \right|^2 = \left| P_y(K_1, K_2, \omega) \right|^2 \left| P(K_1, K_2, \omega) \right|^2 \quad (27)$$

The transfer function  $\Gamma(K_1, K_2, \omega)$  can now be easily computed since both input and output spectra are known. From acoustic interest one would like to determine the modal volume displacement since it is related to the acoustic power.

$$\text{Vol}_{m,n} = \sqrt{2} \bar{Y} \int_0^a \int_0^b \phi(x) \phi(y) dx dy \quad (28)$$

c. Example:

The above results, Equations (24) to (26) and (28), are numerically evaluated for two panel sizes, 12 x 7 x 0.04 inches and 36 x 6-1/2 x 0.04 inches, corresponding to the panel sizes used in the laboratory experiment. Results can be compared only qualitatively with experiment, because the experimental panels are clamped rather than simply supported as assumed in the theory.

Let it be assumed that  $U_c/U_\infty = 0.8$  and  $\delta^* = 0.155$  inch. The mean square displacement is obtained from Equation (25) by setting  $\tau = 0$ ;  $x = x'$ ;  $y = y'$ ;  $t = t'_0$ . The value of  $x, y$  are chosen such that the displacement will be maximum.

The values of total damping for the 12 x 7 x 0.04 inch panels, assumed to be  $a_{m,n} = .5 (\omega_{m,n})^{1/3}$  and  $a_{m,n} = 5 (\omega_{m,n})^{1/3}$  for the 36 x 6-1/2 x 0.04 inch panels, has been measured on the same size panel with the clamped edges when excited by a turbulent boundary layer. One interesting point is that the modal damping is considerably different when the panel is excited by turbulent flow than when excited by pure tones.

The mean square displacement computed at the center of each mode is shown in Fig. 12 for the 12 x 7 x 0.04 inch panel. It increases with the convection velocity for the lower order modes while for the highest modes the mean square displacement levels off for large values of  $U_c$ . This result is quite consistent with the previous experimental work reported by the author in Ref. 5 which shows that the sudden change in slope is due to mismatch in wave number and frequency between the turbulent and panel spectra.

The experimental results indicated also that above the peak displacement the mean square amplitude decreases for further increases in Mach number. This pronounced reduction is not felt by the theoretical panel because the decay of the eddy lifetime  $\theta$  with increasing convection velocity  $U_c$  is not appreciable since  $\theta$  is a weighted average over a narrow bandwidth (Ref. 5, Fig. 5) due to

limited range of frequency component of the correlation measurement. Therefore the experimental panel favors a larger mismatch because the wall pressure spectrum  $P(K_1\omega)$  decays faster than the panel spectrum  $P_v(K_1\omega)$ . The comparison between theory and experiment for the 12 x 7 x .040 panel using the measured value of  $\theta$  is shown in Fig. 13. Figure 12 shows also the variation in mean square displacement with total damping. The change in damping contributed to an almost linear change in the mean square displacement. A more appropriate value of  $\theta$ , total damping  $a_{m,n}$ , and modal bandwidth has been selected from experimental observation in comparing the measured mean square displacement with the correlated one for the 36 x 6.5 x 0.40 inch panel reported in Figs. 14 and 15. Noticeable is the shift of the maximum mean square displacement with  $U_c$  due to the difference in frequency between the two panels because of the different edge conditions. The comparison is satisfactory to validate the reliability of the theory in predicting the response of a single panel, with a proper choice of the value of the damping and eddy lifetime.

The normalized theoretical and experimental broadband space time correlation for a 36 x 6.5 x .040 inch panel is shown in Fig. 16. The two autocorrelograms taken at the center of the panel are quite similar, implying that the number of modes contributing to the broadband response, 40 in all, that is  $m = (1 \text{ to } 20)$  and  $n = (1, 2)$  and the associate modal damping factors are close to those of the experimental panel.

Results can be extended to obtain the cross-correlation everywhere along the panel by simply multiplying by the eigenvalue of Equation (21).

Due to the complexity of the triple integration (Equation (24)), the rigorous validity of the numerical result may depend on the previous assumption that the cross modal effect is eliminated; however, experience obtained from this calculation has indicated that the complete problem can be solved including the cross-modal effect.

The transfer functions, defined in Equation (27) as the ratio between power spectral density of the turbulence and the panel in the wave number frequency scale, constitute the most important result. In the past, a similar approach was used (Ref. 14) expressing the transfer function in terms of frequency and wave number, but the integration proved to be a stumbling block. Theoretically, the one-dimensional wave number frequency spectrum of the exciting pressure field is obtained from Equation (6), (computed values are shown in Fig. 4) and the panel response spectrum can be obtained from the Fourier transform Equation (26) of the cross-correlation function (Equation 24). Experimental spectral densities of both turbulence and panel are shown in Fig. 18 while theoretical panel spectral density has not yet been computed. The effect of matching and mismatching the wave number for a constant frequency clearly shows the mechanism of the excitation of the structure by turbulence. The experimental results have been chosen such that a strong coincidence effect dominates. This is also indicated by the closely matching behavior of the two cospectra. An interesting point is that the turbulent eddy decays much faster than the wave on the panel. Therefore, the matching of the two spectra occurs only in a very narrow range of frequency and wave number.

The modal volume for the 36 x 6.5 x .040 inch and 36 x 6.5 x .08 inch panels has been computed from Equation (28) to predict the acoustic power radiated of Section VI, since the power radiated is proportional to the uncanceled volume velocity.

## V. EXPERIMENTAL RESULTS ON THE REFLECTION AND TRANSMISSION OF A FLEXURAL WAVE ON THE PANEL

Space time correlation for various panel displacements consistently indicates that the panel response is prominently excited by running flexural waves with the highest correlation occurring along lines  $\xi - U_c \tau = \text{constant}$  in the  $\xi, \tau$  plane as shown in Fig. 17 where  $\xi = x - x'$ . (Ref. 5 and 21). This demonstrates that the average convection velocity coincides with the average wave velocity in the panel. The correlograms also indicate that the surface waves have a phase velocity of  $\pm U_c$ . The symmetry in the positive and negative time delay is interpreted as waves, one moving with the flow and another opposite to the flow.

The reflection and transmission problem is experimentally investigated on a 36 x 6-1/2 x 0.04 inch panel by setting up two test configurations. In the first configuration the panel is damped at the downstream side. The damping material consists of a 1/2-inch thick layer of sand retained within 4 inches of the end by soft rubber wedges glued across the panel. The space time correlation of the displacement measured along the centerline from the center toward the damped side is shown in Fig. 19. The space time correlogram for the panel with damped edges is quite different from the correlogram for the bare panel. The wave moving with  $+U_c$  (downstream) is undamped for both panels while the wave moving with  $-U_c$  (upstream) the damped panel shows that the negative correlation is damped. The interpretation is that the sand has partially damped the incident wave at the downstream edge since no correlation and convection results with the negative delay.

The second configuration is made on the same size panels divided by two equally spaced stringers glued to the panel, as reported in Ref. 24. The correlation between stringers, (Fig. 20) shows the well known behavior of waves moving with  $\pm U_c$  while the correlation across the stringers indicates an unswept pattern in the time scale corresponding to a standing wave pattern. The interpretation of the correlogram is that running waves are reflected at the stringer boundaries while the standing waves are transmitted.

## VI. RADIATION OF SOUND BY FLEXIBLE PANELS

In the previous sections we have discussed the response of panels excited by turbulent boundary layers, and in this section we will explore the radiation resulting from the vibration of these panels. In the structural response to turbulence study, it was found that the structural response is in the form of a forced vibration and coincident vibration. If the structural panel has a mass law behavior (forced vibration), the response will then be computed easily since it depends on the weight per unit area of the structure; in the case of coincidence, the response is above the mass law and the problem becomes more complex since the pressure field on the panel becomes the controlling mechanism of the response. To estimate the sound power level, the modal volume displacement or an equivalent radiation efficiency must be ascertained. Theoretical prediction of the radiation efficiency and measurement of the acoustic damping have been reported in Refs. 25 through 27, and 5. The radiation property of the panel is related to the volume velocity in each mode, which often radiates like independent monopoles. For a finite panel, the major source of radiation below the critical frequency,  $f_c = 1/2\pi a^2 / KC\ell$ , arises from the interaction of the bending wave with the discontinuity of the boundary. The present panel sizes have modes that radiate mainly below the critical frequency where the radiation is somewhat less efficient than it is at the critical frequency or above. Below the critical frequency, the radiation from a 1/4 wavelength of the mode segment is cancelled by the radiation of the adjacent 1/4 wavelength which is out of phase. This process of cancellation is extended across the four boundaries of the panel and the effective radiation area lying between the panel edges and the nearest 1/4 wavelength. If the flexural wavelength component is larger than the acoustic wavelength, as in the case of the 17-1 and 19-1 modes, of the 36 x 6-1/2 x .040 inch panel (Fig. 21) the 1/4 wavelengths along the two side edges are acoustically uncoupled and combine to form an edge mode. Since the edge mode occurs at both ends of the panel whose corners are 36 inches apart, the edge mode radiation becomes uncoupled, because the distance between them is much larger than the acoustic wavelength. Each edge mode gives rise to an edge radiator which radiates independently. This cancellation process can be carried out for all m and n modes, which shows that the resulting sources are monopoles for the odd-odd

mode, dipole for the even-odd mode, and quadrupole for the even-even mode. Since power radiated by the dipole or quadrupole is much smaller than the monopole, one can neglect the power in the even-odd and even-even mode. In this analysis, the modal volume displacement has been measured for the odd-odd and for the even-odd modes associated with the acoustic power radiated in a reverberation room. Both measurements are useful in making an accurate assessment of the radiated power to be used with the response theory of the panel displacement of the previous section to predict the acoustic power radiated. The modal acoustic power radiated in a reverberant field in terms of modal velocity is given by

$$PWL_{m,n} = \frac{N\omega^2 \rho c K_a^2}{4\pi Y^2} \frac{2P_r + P_p}{P_p} \left[ \int_0^a \int_0^b |\phi_m(x)| |\phi_n(y)| dx dy \right]^2 \quad (30)$$

The value of N depends on the radiation mode which can be classified as an edge radiation or piston radiation. Here, piston radiation, for which  $N = 4$ , was assumed for the purpose of calculation. The value of N also depends on the distance between sources in relationship to the acoustic wavelengths as well as on the panel boundary (Refs. 25 and 27). The ratio  $(2P_r + P_p)/P_p$  is the contribution due to stringers mounted on the panel, following Ref. 25. Comparison of the radiated power is shown in Figs. 22, 23, and 24 by direct measurement and by Equation (30) using a measured value of the mean square displacement. The comparison is in satisfactory agreement for a simple panel for thicknesses .080-inch and .040-inch as well as for panels with stringer combinations using the idealized ratio suggested by Ref. 25. It is believed therefore that with the proper choice of damping, the total acoustic power is obtainable directly from the structural response of the panel given by Equation (24).

The eigenvalues for the lateral and longitudinal modes of the 36-inch by 6.5-inch panel with rigid boundaries are given in Table 4, following the same method used in Refs. 5 and 29.

\*The use of this equation has been suggested to the author by Dr. R. H. Lyon.

Another interesting method for predicting the radiated power has been recently reported by Ref. 23 using the modal density approach averaging over a bandwidth for vibration response and radiation. This approach shows good agreement with two different experiments, one of which is that made by the author.

The most relevant phenomena relevant to both power radiation and the response of the panel is the effect of coincidence, characterized by the peak in amplitude displacement, as well as in the acoustic power radiated. Above the peak displacement, the effect of rolling off in amplitude, appears to be associated with progressive decrease in wave length which contribute to the change in the power law from  $U^5$  to  $U^{2,3}$  discussed in the previous experiment Refs. 4 and 5. This change can be easily visualized from the cross-power spectrum of both turbulence and panel (Fig. 18). The mismatch both above and below coincidence in frequency and wave number is the cause of the changing power law and can be attributed to a rapid decay of the eddy in the turbulent boundary layer in relationship to the panel mode.

#### VII. RADIATION OF SOUND FROM HONEYCOMB PANELS

The honeycomb structure has recently received wide application by airframe manufacturers because of its integrity and light weight characteristics. Therefore, it became useful to determine the noise radiated from such a structure under boundary layer excitation. Measurements were conducted on a size 7 x 12 inch panel with 3 types of honeycomb: two having total thickness of 0.25 inch. One panel's surfaces was made of 0.01 inch aluminum; the other with 0.01 inch titanium. The third honeycomb panel was 0.1 inch thick with the surfaces made of an 0.01-inch aluminum sheet. All three panels have an aluminum core glued to the top and bottom panels. Since all three panels have a weight comparable to the common aircraft panel, a 0.040-inch thick aluminum panel is chosen for comparison of the acoustic power level radiated using a radiating area of 7 x 12 inches. The acoustic power is plotted in Fig. 25 in 1/3-octave bands. The level of the 0.040-inch panel dominates over the honeycomb panels with lower frequency characteristics. The second highest level is the aluminum honeycomb 0.1-inch thick which shows a shift in the fundamental mode from 300 to 600 cps with respect to the 0.040 panel. A considerably lower level results from the 0.25-inch aluminum and titanium panels which show a comparable level between them except for the 3 db differences at the peak. For the

aluminum panel the peak occurs at 1000 cps and for the titanium at the 1250 cps. A slight shift in the maximum response is expected due to the slight change in weight between the aluminum panel (0.33 pounds) and the titanium panel (0.26 pounds).

The structural response of the honeycomb panel has not yet been determined but the preliminary results indicate that the response predominates at a higher frequency than with the simple aluminum panel. The highest frequency sound radiation of the honeycomb can be very easily attenuated by the usual absorbent acoustic material whereas in the lower frequency region, the simple aluminum panel is still a major problem for the transmission of sound. One can conclude from this experiment that the transmission loss through the honeycomb structure is a function of stiffness which is related to thickness. Figure 26 also shows the comparison of the change in power level with Mach number. At high speed, the honeycomb radiates more efficiently, however, the level is still lower than the usual skin panel. In the case of aircraft sidewall structure, a liner is used which satisfies a double purpose: thermal and acoustic insulation. This gives considerable sound attenuation in the higher frequencies and, therefore, improvement in level between the honeycomb panel and the normal sidewall panel structure.

#### VIII. CONTRIBUTION OF THE PANEL BOUNDARY TO SOUND POWER RADIATION

Experimental results have indicated that, for frequencies below the critical frequency, the power radiated by the panel changes with the edge conditions of the boundaries. Analyses made in Refs. 27 and 33 have indicated some sensitivity of the radiation efficiency to the edge conditions. The results computed in the previous chapter confirmed that the noise comes from the uncanceled edge half because of the interaction with the boundary. A series of experiments have been conducted with different edge boundaries to determine if there is any possibility of reducing the acoustic power radiated. An interesting result obtained demonstrates the possibility of minimizing the acoustic power radiated by modifying the panel boundaries. The best results show an average of 10 db reduction in the power level by using 15 percent additional

panel weight to modify the boundaries. Typical data using three boundary configurations on a 36 x 6-1/2 x 0.040 inch panel are shown in Figs. 27, 28, and 29.

The first configuration is made up of three layers of different lengths of 0.001 inch thick steel membranes glued to the upstream and downstream edges of the panel. Effectively, the membranes increased the panel stiffness gradually through the last wavelength toward the boundaries.

The second configuration consists of rubber wedges at both ends of the panel, Fig. 30. The rubber wedges are lighter than the membranes with an optimum reduction in acoustic power above 250 cps. Figures 27 and 28 show the results in terms of flow Mach number compared with a bare panel and a panel mounted on the two equally spaced stringers and Fig. 29 shows the results in 1/3-octave band level. The structural response of the first two configurations has not yet been made. However, it is expected that an increase in the frequency and decrease in the volume displacement will occur. This last decrease will contribute a lower radiation level. Speculation can be made that a reduction in level may have some contribution from the mismatch in the frequency and wave number scale from waves propagating toward the boundary of the panel due to low damping and from the wave length resulting from the corner interacting with the phase and amplitude of the local turbulent mode. The reduction in power level is significant enough to encourage further investigation.

The last configuration consists of damping the flexural wave on the panel propagating with the speed  $\pm U_c$ . The downstream side of the panel only is damped by sand to interpret more significantly the reflected part. This is the space time correlation case discussed in Section V and in Figs. 17 and 19 with and without damping. The waves that are not reflected from the downstream edge of the boundary contribute significantly to a reduction in acoustic power. This method, though impractical, shows the contribution of the running wave to the acoustic power radiated when it is reflected by the boundary.

#### IX. EFFECT OF PRESSURIZATION ON THE RESPONSE OF THE PANEL EXCITED BY A TURBULENT BOUNDARY LAYER

An aircraft flying at high altitude has a static pressure differential between the cabin pressure and the local atmosphere. This produces a static deflection on the fuselage panels which is related to the geometry and framework of the structure and loading. If the deflection is not small compared to the thickness of the panel, the stretching of the middle surface of the plate must be taken into account in calculating the modal frequency of vibration. Due to the resistance of the plate to stretching, the rigidity and frequency will increase with the pressure differential. Measurements made in the boundary layer facility have shown that the frequency of vibration and the radiation level shift to higher frequency with the increase in pressure differential across the panel. The correct magnitude of the displacement level and acoustic power level has not been validated because the curvature of the flexible panel joining the rigid one at each of the four boundaries will cause the flow to trip and generate additional noise. The sudden change in slope as the flow approached the larger static deflection of the boundaries which has superimposed on dynamic vibration is a source of additional noise.

Tests on the pressurization effect were possible on the 720 airplane both for the acceleration level on a sidewall panel and sound pressure level taken a few inches away from the side panel. Results shown in Fig. 31 reasonably indicate a shift due to change in pressurization from 3 to 8 psi differential at an altitude of 25,000 feet and Mach 0.87. The change in amplitude of the acceleration level with the pressurization cannot be regarded as a general increase since one has to obtain the space average of the mode rather than the rms value at a point. The frequency shift due to pressurization results of the order of the pressure ratio between the cabin and the pressure altitude. A freise prediction is given in Ref. 36 where agreement with the measurements is excellent.

#### X. CONCLUSIONS

Measurement and analysis of the statistical properties of the surface pressure fluctuation, the response of panel, and the resultant radiation field were carefully investigated and its most important feature, the response and acoustic radiation, can be reasonably predicted given the initial flow condition and panel damping.

The wave number and frequency spectrum of the pressure fluctuation show that the main energy is concentrated around the convection velocity with the highest level at the lowest frequency and wave number, indicating that each peak is convected at different velocities. For a given frequency a critical wave number exists, below which the wall pressure is part of an oscillatory field or sound field, and the eddy convection velocity becomes supersonic.

Comparison has been made of the cross power spectrum of the turbulence with the cross power spectra of the panel. The superposition of wave number and frequency spectra indicate the matching or mismatching of spectra, the most significant excitation of the panel by turbulence.

The acoustic power radiated comes from the uncancelled volume velocity at the panel boundary in agreement with Ref. 25. By modifying the boundary condition, considerable reduction in acoustic power radiated can be obtained.

APPENDIX A

Equation (1) shows that the decay of the broadband space-time correlation is given by  $\exp(-|\xi|/U_c\theta)$  rather than the more common form shown in previous reference  $\exp(-|\tau|/\theta)$ . It is rather difficult to see the implication of the choice of the exponential without performing the transform with respect to  $\tau$ , as well as by comparing the cross correlation using both exponential forms. Therefore, rewriting Equation (1) using the form  $\exp(-|\tau|/\theta)$  we obtained:

$$R(\xi, \eta, \tau) = e^{-|\tau|/\theta} \left[ A_1 e^{-\left[ (\xi - U_c \tau)^2 + \eta^2 \right] / 2\sigma_1^2} + A_2 e^{-\left[ (\xi - U_c \tau)^2 + \eta^2 \right] / 2\sigma_2^2} \right] \quad (1')$$

Taking the Fourier transform respect to  $\tau$  Equation (1') becomes

$$\begin{aligned} P(\xi, \eta, \omega) &= \frac{1}{2\pi} \int_{-\infty}^{\infty} R(\xi, \eta, \tau) e^{-i\omega\tau} d\tau = \\ &= \frac{e^{-i\omega(|\xi|/U_c - \sigma_1^2/U_c^2\theta)}}{\sqrt{2\pi} U_c} \left[ A_1 \sigma_1 e^{-\frac{-(\eta^2 + \xi^2)/2\sigma_1^2}{U_c^2/2\sigma_1^2} (\xi/U_c - \sigma_1^2/U_c^2\theta)^2} \right. \\ &\quad \left. e^{-\sigma_1^2\omega^2/2U_c^2} \right] + \frac{e^{-i\omega(|\xi|/U_c - \sigma_2^2/U_c^2\theta)}}{\sqrt{2\pi} U_c} \left[ A_2 \sigma_2 e^{-\frac{-(\eta^2 + \xi^2)/2\sigma_2^2}{U_c^2/2\sigma_2^2} (\xi/U_c - \sigma_2^2/U_c^2\theta)^2} \right. \\ &\quad \left. e^{-\sigma_2^2\omega^2/2U_c^2} \right] \quad (2') \end{aligned}$$

The power spectrum on (2') is of the same type as the one given by Equation (13) using  $\exp(-|\xi|/U_c\theta)$  form. The differences, however, are in the phase change, by the factor  $\sigma^2/U_c^2\theta$  which is constant. The comparison of the cross correlation is given by Equations (1) and (1') as well as shown in Fig. 32.

Since excellent agreement indicates the functional form of the wall pressure correlation fits the experimental cross correlation distribution, either one of two forms of exponential may be used to describe the decay of the wall pressure correlation.

APPENDIX B

DERIVATION OF THE CROSS-CORRELATION - INTEGRAL 24

In order to simplify the computation of Equation (24), an attempt is made to change the variable of integration, thus reducing the number of operations for the integral. Rewriting Equation (24)

$$\overline{Y(x, y, t) Y(x', y', t')} = \frac{\overline{p^2}}{\sum_{\nu=1}^3 \frac{A_\nu}{K_\nu} K_\nu^2} \sum_{m, n} \frac{\phi_{m, n}(x, y) \phi_{mn}(x', y')}{\omega_{mn}^2}$$

$$\cdot \int_{-\infty}^t dt_0 \int_{-\infty}^{t'} dt'_0 \int_0^a dx_0 \int_0^b dy_0 \int_0^a dx'_0 \int_0^b dy'_0 e^{-a_{m, n}(t' - t'_0)}$$

$$\cdot \left[ \sin \omega_{mn} (t' - t'_0) u(t' - t'_0) \right]$$

$$\cdot \left\{ \sum_{\nu=1}^3 \frac{A_\nu K_\nu e^{-\left| \frac{t_0 - t'_0}{\theta} \right|}}{K_\nu^2 + \left( \frac{1}{FU} \right)^2 \left[ \left( (x_0 - x'_0) - U_c [t_0 - t'_0] \right)^2 + (y_0 - y'_0)^2 \right]} \right\} \frac{1}{\sum_{\nu=1}^3 \frac{A_\nu}{K_\nu}} \quad (1B)$$

The mode shape which satisfies the eigen function equation subject to the panel boundary condition for simply supported edges is

$$\phi_{m, n}(x, y) = \frac{2}{(ab)^{1/2}} \sin \frac{m\pi x}{a} \sin \frac{n\pi y}{b}$$

and

$$\phi_{m, n}(x, y) \phi_{m, n}(x'_0, y'_0) = \frac{1}{ab} \left[ \cos \frac{m\pi(x_0 - x'_0)}{a} - \cos \frac{m\pi(x_0 - x'_0)}{a} \right]$$

$$\left[ \cos \frac{n\pi(y_0 - y'_0)}{b} - \cos \frac{n\pi(y_0 - y'_0)}{b} \right] \quad (2B)$$

Considering the space integrals in (1B) and using the product in (2B)

$$I_{\nu} = \int_0^a dy_0 \int_0^b dy'_0 \int_0^a dx_0 \int_0^a dx'_0 \cdot \frac{1}{ab} \left[ \cos m\pi \frac{(x_0 - x'_0)}{a} - \cos m\pi \frac{(x_0 + x'_0)}{a} \right] \left[ \cos n\pi \frac{(y_0 - y'_0)}{b} - \cos n\pi \frac{(y_0 + y'_0)}{b} \right] \frac{1}{K_{\nu}^2 \left( \frac{1}{FU} \right)^2 \left[ \left| (x_0 - x'_0) - U_c (t_0 - t'_0) \right|^2 + (y_0 - y'_0)^2 \right]} \int_0^a dy_0 \int_0^b dy'_0 \int_0^a dx_0 \int_0^a dx'_0 f(y_0, y'_0, x_0, x'_0) \quad (3B)$$

Setting the new limits and finding the Jacobian

$$\begin{aligned} \eta' &= y_0 + y'_0 & \eta' + \eta &= 2y_0 & y_0 &= (\eta' + \eta)/2 & g_1 &= g_1(\eta, \eta', \xi, \xi') \\ \eta &= y_0 - y'_0 & \eta' - \eta &= 2y'_0 & y'_0 &= (\eta' - \eta)/2 & g_2 &= g_2(\eta, \eta', \xi, \xi') \\ \xi' &= x_0 + x'_0 & \xi' + \xi &= 2x_0 & x_0 &= (\xi' + \xi)/2 & g_3 &= g_3(\eta, \eta', \xi, \xi') \\ \xi &= x_0 - x'_0 & \xi' - \xi &= 2x'_0 & x'_0 &= (\xi' - \xi)/2 & g_4 &= g_4(\eta, \eta', \xi, \xi') \end{aligned}$$

From Ref. 35, Page 271

$$I_{\nu} = \int_{\underline{X}} f(x) dx = \int_{q^{-1}(\underline{X})} f[g(t)] |J_g(t)| dt \quad (4B)$$

$$J_g(t) = \partial(g_1, g_2, g_3, g_4) / \partial(\eta, \eta', \xi, \xi')$$

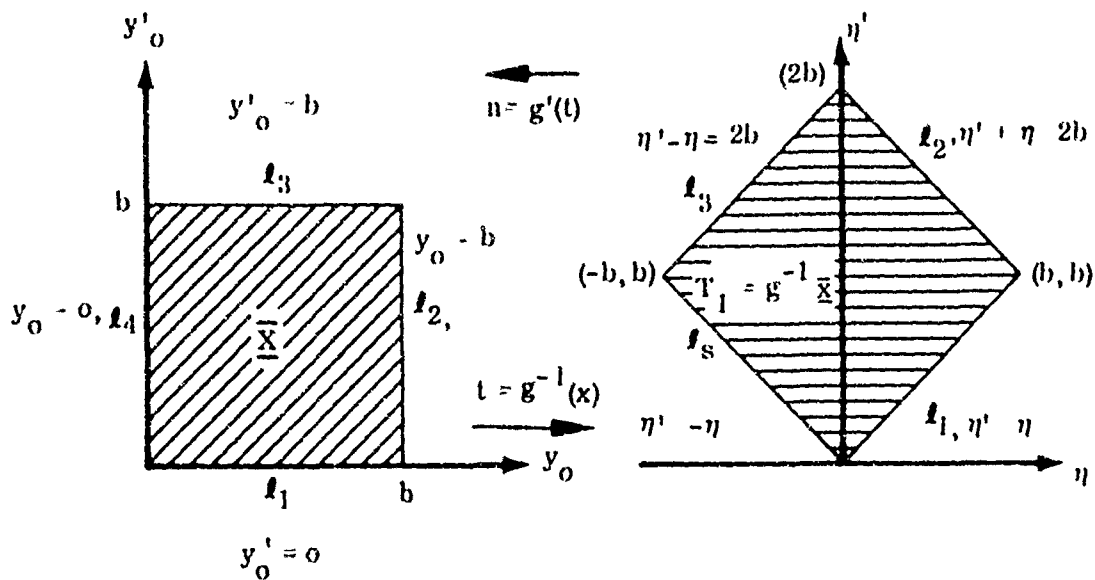
$$\begin{vmatrix} \partial g_1 / \partial \eta & \partial g_1 / \partial \eta' & \partial g_1 / \partial \xi & \partial g_1 / \partial \xi' \\ \partial g_2 / \partial \eta & \partial g_2 / \partial \eta' & \partial g_2 / \partial \xi & \partial g_2 / \partial \xi' \\ \partial g_3 / \partial \eta & \partial g_3 / \partial \eta' & \partial g_3 / \partial \xi & \partial g_3 / \partial \xi' \\ \partial g_4 / \partial \eta & \partial g_4 / \partial \eta' & \partial g_4 / \partial \xi & \partial g_4 / \partial \xi' \end{vmatrix} \quad 1/4 \quad (5B)$$

Then

$$f[g(t)] = f\left[g_1(\eta, \eta', \xi, \xi'), g_2(\eta, \eta', \xi, \xi'), g_3(\eta, \eta', \xi, \xi'), g_4(\eta, \eta', \xi, \xi')\right]$$

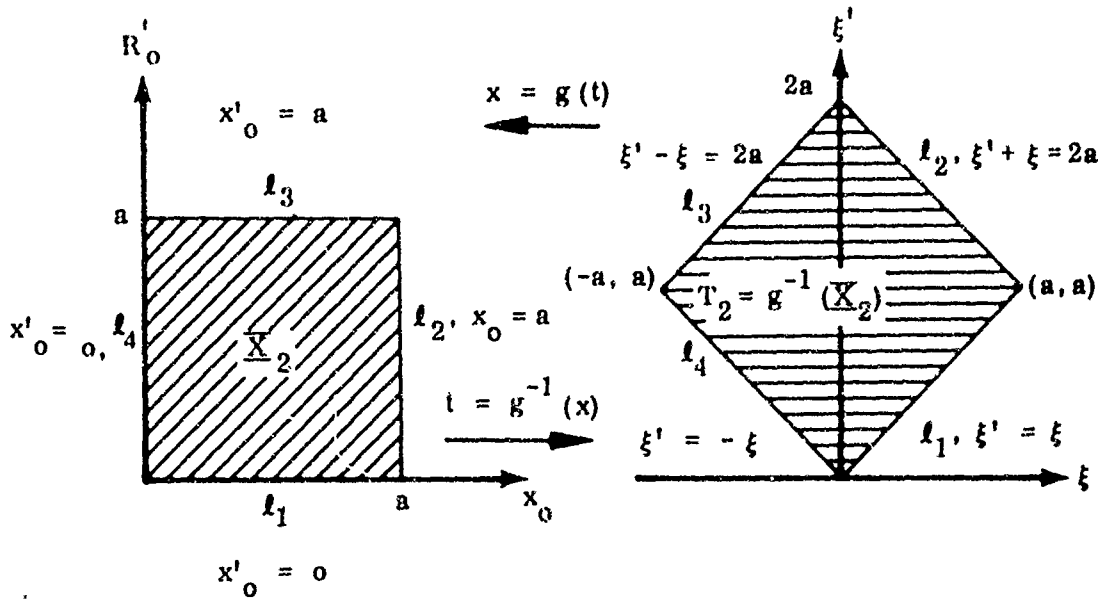
$$f\left[\frac{(\eta' + \eta)/2, (\eta' - \eta)/2, (\xi' + \xi)/2, (\xi' - \xi)/2}{\frac{1}{ab} \left| \cos \frac{m\pi\xi}{a} - \cos \frac{m\pi\xi'}{a} \right| \left| \cos \frac{n\pi\eta}{b} - \cos \frac{n\pi\eta'}{b} \right|} \right]$$

$$K_\nu^{-2} \left( \frac{1}{F(t)} \right)^2 \left[ \left[ \xi - U_c(t_0 - t'_0) \right]^2 + \eta^2 \right] \quad (6B)$$



- $\ell_1 : y'_0 = 0 \longleftrightarrow \eta' = \eta$
  - $\ell_2 : y_0 = b \longleftrightarrow \eta' + \eta = 2b$
  - $\ell_3 : y'_0 = b \longleftrightarrow \eta' - \eta = 2b$
  - $\ell_4 : y_0 = 0 \longleftrightarrow \eta' = -\eta$
- $$\eta' = y_0' - y'_0 = g_1^{-1}(y_0', y'_0, x_0, x'_0)$$
- $$\eta = y_0 - y'_0 = g_2^{-1}(y_0, y'_0, x_0, x'_0)$$

Similarly for longitudinal coordinates



- $l_1: x'_0 = 0 \longleftrightarrow \xi' = \xi$
  - $l_2: x_0 = a \longleftrightarrow \xi' + \xi = 2a$
  - $l_3: x'_0 = a \longleftrightarrow \xi' - \xi = 2a$
  - $l_4: x_0 = 0 \longleftrightarrow \xi' = -\xi$
- $$\xi' = x_0 + x'_0 = y_3^{-1}(y_0, y'_0, x_0, x'_0)$$
- $$\xi - x_0 - x'_0 = y_4^{-1}(y_0, y'_0, x_0, x'_0)$$

The limit for the  $\bar{X}$  to T planes are set to

$$\bar{X} = g(t) \left\{ (y_0, y'_0, x_0, x'_0): 0 \leq y_0 \leq b, 0 \leq y'_0 \leq b, 0 \leq x_0 \leq 0, 0 \leq x'_0 \leq a \right\}$$

$$T = g + (\bar{X}) = \left\{ (\eta, \eta', \xi, \xi'): -b \leq \eta \leq b, |\eta| \leq \eta' \leq 2b - |\eta|, -a \leq \xi \leq a, \right.$$

$$\left. |\xi| \leq \xi' \leq 2a - |\xi| \right\} \quad (7B)$$

Using the definition of 4B

$$I_p \int_X f(x) dx = \int_T f(g(t)) |J_y(t)| dt$$

Then after integrating with respect to  $\xi'$  and  $\eta'$  (6B) is reduced to:

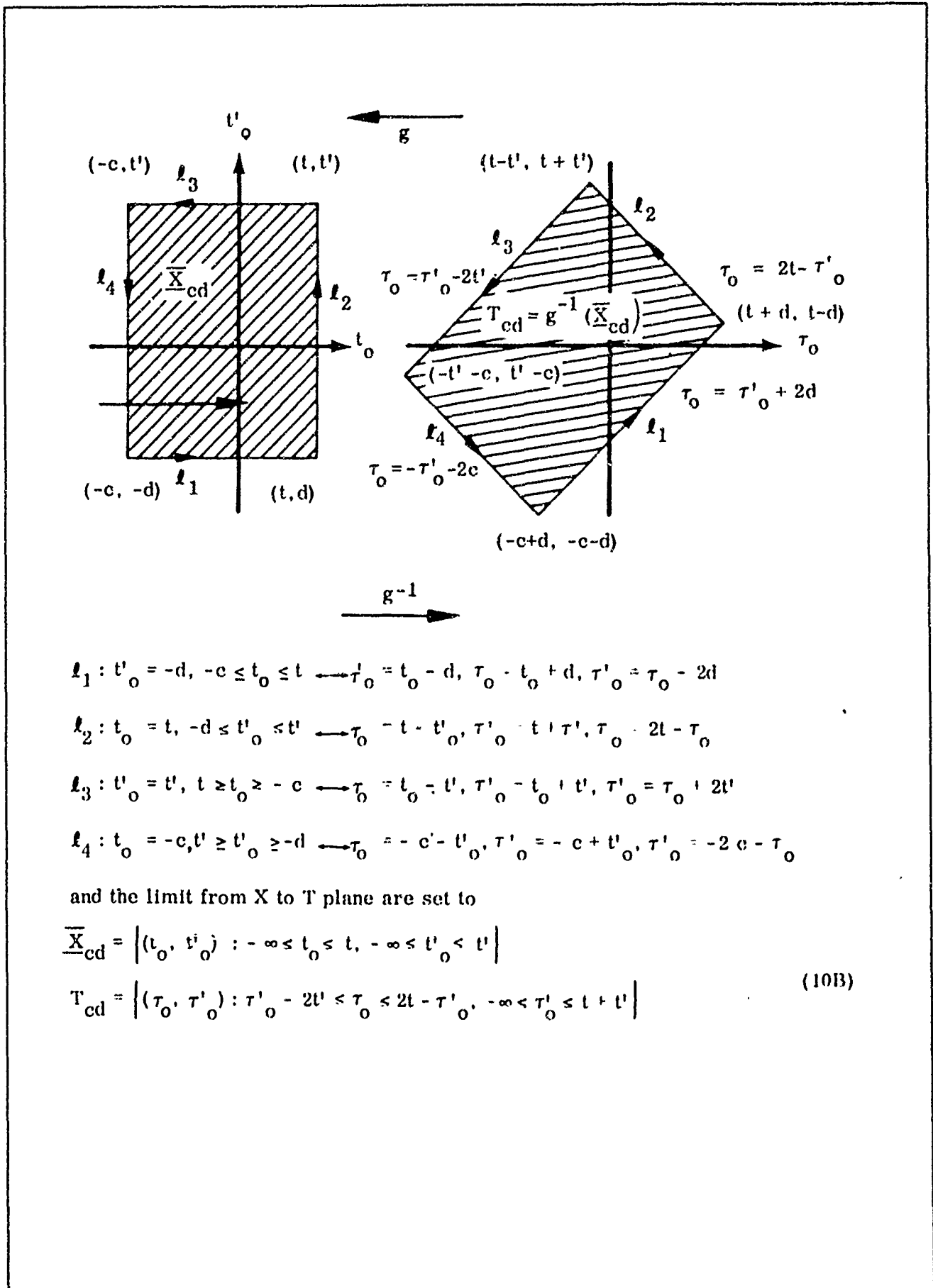
$$I_\nu \frac{z}{ab} \int_a^b \left[ \int_{-0}^b \frac{b(a-|\xi|) \cos \frac{m\pi\xi}{a} + \frac{a}{m\pi} \sin \frac{m\pi|\xi|}{a} \left[ (b-\eta) \cos \frac{n\pi\eta}{b} + \frac{b}{n\pi} \sin \frac{n\pi\eta}{b} \right]}{K_\nu^2 + \left( \frac{1}{FU_c} \right)^2 \left[ \left[ \xi - U_c(t_0 - t'_0) \right]^2 + \eta^2 \right]} d\eta \right] d\xi \quad (8B)$$

Using the new limits Equation (1B) can be written as:

$$\begin{aligned} Y(x, y, t) Y(x', y', t') &= \frac{v^2}{\sum_{\nu=1}^3 (\Lambda_\nu / K_\nu)^2 \pi^2} \sum_{m,n} \frac{\phi_{m,n}(x, y) \phi_{m,n}(x', y')}{\omega_{m,n}^2} \\ &\cdot \int_{-\infty}^t dt_0 \int_{-\infty}^{t'} dt'_0 \left\{ e^{-a_{m,n}(t-t_0)} \left[ \sin \omega_{m,n}(t-t_0) \right] u(t-t_0) e^{-a_{m,n}(t'-t'_0)} \right. \\ &\cdot \left. \left[ \sin \omega_{m,n}(t'-t'_0) \right] u(t'-t'_0) \right\} \sum_{\nu=1}^3 \left[ \Lambda_\nu K_\nu \int_0^a dx_0 \int_0^b dy_0 \int_0^a dx'_0 \int_0^b dy'_0 \right. \\ &\cdot \left. \frac{\phi_{m,n}(x_0, y_0) \phi_{m,n}(x'_0, y'_0) e^{-|(t_0 - t'_0)/\theta|}}{K_\nu^2 + \left( \frac{1}{FU_c} \right)^2 \left[ \left[ (x_0 - x'_0) - u_c(t_0 - t'_0) \right]^2 + (y_0 - y'_0)^2 \right]} \right] \quad (9B) \end{aligned}$$

Setting the new time limit and finding the Jacobian

$$\begin{aligned} t'_0 &= t_0 + t'_0 & 2t_0 &= \tau_0 + \tau'_0 & t_0 &= (\tau'_0 + \tau_0)/2 & g_1(\tau_0, \tau'_0) \\ \tau_0 &= t_0 - t'_0 & 2t'_0 &= \tau'_0 - \tau_0 & t'_0 &= (\tau'_0 - \tau_0)/2 & g_2(\tau_0, \tau'_0) \\ J(\tau_0, \tau'_0) &= \partial(g_1, g_2) / \partial(\tau_0, \tau'_0) = \begin{vmatrix} \partial g_1 / \partial t_0 & \partial g_1 / \partial t'_0 \\ \partial g_2 / \partial \tau_0 & \partial g_2 / \partial \tau'_0 \end{vmatrix} = 1/2 \end{aligned}$$



Substituting the new limit in equation (9B) and interpreting with respect  $\tau'_0$  after a long manipulation the cross correlation is reduced to:

$$\overline{Y(x, y, t) Y(x', y', t)} = \frac{p^2}{\sum_{\nu=1}^3 (A_{\nu}/K_{\nu})^2} \sum_{m,n} \frac{\phi_{m,n}(x, y) \phi_{m,n}(x', y')}{\omega_{m,n}^2} \frac{A_{\nu} K_{\nu}}{2ab} [I_1 + I_2] \quad (11B)$$

where

$$I_1 = \frac{\omega_{m,n}}{a_{m,n}^2 + \omega_{m,n}^2} \int_{-a}^a f_1(\xi) \left[ \int_0^b f_2(\eta) \cdot \left[ \int_{-\infty}^{\tau} \frac{e^{-a_{m,n}(\tau-\tau_0)} \left| \sin \omega_{m,n}(\tau-\tau_0) + \frac{\omega_{m,n}}{a_{m,n}} \cos \omega_{m,n}(\tau-\tau_0) \right| e^{-|\tau_0/\theta|}}{K_{\nu}^2 + \left(\frac{1}{FU}\right)^2 \left| (\xi - U_c \tau_0)^2 + \eta^2 \right|} d\tau_0 \right] d\eta \right] d\xi$$

$$I_2 = \frac{\omega_{m,n}}{a_{m,n}^2 + \omega_{m,n}^2} \int_{-a}^a f_1(\xi) \left[ \int_0^b f_2(\eta) \cdot \left[ \int_{\tau}^{\infty} \frac{e^{-a_{m,n}(\tau_0-\tau)} \left| \sin \omega_{m,n}(\tau_0-\tau) + \frac{\omega_{m,n}}{a_{m,n}} \cos \omega_{m,n}(\tau_0-\tau) \right| e^{-|\tau_0/\theta|}}{K_{\nu}^2 + \left(\frac{1}{FU}\right)^2 \left| (\xi - U_c \tau_0)^2 + \eta^2 \right|} d\tau_0 \right] d\eta \right] d\xi$$

where

$$f_1(\xi) = (a - |\xi|) \cos \frac{m\pi\xi}{a} + \frac{a}{m\pi} \sin \frac{m\pi|\xi|}{a}$$

$$f_2(\eta) = (b - \eta) \cos \frac{n\pi\eta}{b} + \frac{b}{n\pi} \sin \frac{n\pi\eta}{b}$$

Let the time integral be simplified by changing the limit of integration.  
From (11B),  $I_1$ ,

$$\bar{K}_1 = \int_{\infty}^{\tau} \frac{e^{-a_{m,n}(\tau-\tau_0)} \left| \sin \omega_{m,n}(\tau-\tau_0) + \frac{\omega_{m,n}}{a_{m,n}} \cos \omega_{m,n}(\tau-\tau_0) \right|}{K_\nu^2 + \left( \frac{1}{FU_c} \right)^2 \left[ (\xi - U_c \tau)^2 + \eta^2 \right]} d\tau_0$$

Set

$$\bar{x} = \tau - \tau_0, \tau_0 = \tau - \bar{x}, d\bar{x} = -d\tau_0$$

Then

$$\bar{K}_1 = \int_0^{\infty} \frac{e^{-a_m \bar{x}} \left| \sin \omega_{m,n} \bar{x} + \frac{\omega_{m,n}}{a_{m,n}} \cos \omega_{m,n} \bar{x} \right|}{K_\nu^2 + \left( \frac{1}{FU_c} \right)^2 \left[ \left( |\xi - U_c \tau| + U_c \bar{x} \right)^2 + \eta^2 \right]} d\bar{x}$$

Similarly

$$\bar{K}_2 = \int_{\tau}^{\infty} \frac{e^{-a_{m,n}(\tau_0-\tau)} \left| \sin \omega_{m,n}(\tau_0-\tau) + \frac{\omega_{m,n}}{a_{m,n}} \cos \omega_{m,n}(\tau_0-\tau) \right|}{K_\nu^2 + \left( \frac{1}{FU_c} \right)^2 \left[ \left( |\xi - U_c \tau| - U_c \bar{x} \right)^2 + \eta^2 \right]} d\bar{x}$$

Set

$$\bar{x} = \tau_0 - \tau, \tau_0 = \tau + \bar{x}, d\bar{x} = d\tau_0$$

$$\bar{K}_2 = \int_0^{\infty} \frac{e^{-a_{m,n} \bar{x}} \left| \sin \omega_{m,n} \bar{x} + \frac{\omega_{m,n}}{a_{m,n}} \cos \omega_{m,n} \bar{x} \right|}{K_\nu^2 + \left( \frac{1}{FU_c} \right)^2 \left[ \left( |\xi - U_c \tau| - U_c \bar{x} \right)^2 + \eta^2 \right]} d\bar{x}$$

Substituting the above into (11B) for  $I_1$  and  $I_2$ :

$$\overline{Y(x, y, t) Y(x', y', t')} = \frac{p^2}{2ab \sum_{\nu=1}^3 (A_{\nu}/K_{\nu})^2} \sum_{m, n} \frac{\phi_{m, n}(x, y) \phi_{m, n}(x', y')}{\omega_{m, n} (a_{m, n}^2 + \omega_{m, n}^2)}$$

$$\cdot \int_{-a}^a f_1(\xi) \left[ \int_0^b f_2(\eta) \left[ \int_0^{\infty} g_1(\bar{x}) \sum_{\nu=1}^3 \left\{ \frac{e^{-|(\tau-\bar{x})/\theta|}}{K_{\nu}^2 + \left(\frac{1}{FU_c}\right)^2 \left[ \left( \left| \xi - U_c \tau \right| + U_c \bar{x} \right)^2 + \eta^2 \right]} \right. \right. \right. \right.$$

$$\left. \left. \left. + \frac{e^{-|(\tau+\bar{x})/\theta|}}{K_{\nu}^2 + \left(\frac{1}{FU_c}\right)^2 \left[ \left( \left| \xi - U_c \tau \right| + U_c \bar{x} \right)^2 + \eta^2 \right]} \right\} d\bar{x} \right] d\eta \right] d\xi$$

where

$$f_1(\xi) = (a + |\xi|) \cos \frac{m\pi\xi}{a} + \frac{a}{m\pi} \sin \frac{m\pi|\xi|}{a}$$

$$f_2(\eta) = (b - \eta) \cos \frac{n\pi\eta}{b} + \frac{b}{n\pi} \sin \frac{n\pi\eta}{b}$$

(12B)

$$g_1(\bar{x}) = e^{-a m \bar{x}} \left[ \sin \omega_{m, n} \bar{x} + \frac{\omega_{m, n}}{a_{m, n}} \cos \omega_{m, n} \bar{x} \right]$$

In Equation (12B) setting  $y = \frac{n\pi}{b}\eta$  and  $z = \frac{m\pi}{a}\xi$  will result in:

$$\overline{Y(x, y, t) Y(x', y', t')} = \frac{p^2}{2\pi^2 \left( \sum_{\nu=1}^3 (A_{\nu}/K_{\nu})^2 \right)} \sum_{m, n} \frac{\phi_{m, n}(x, y) \phi_{m, n}(x', y')}{m, n (a_{m, n}^2 + \omega_{m, n}^2)}$$

$$\cdot \int_{-m\pi}^m f_{11}(z) \left[ \int_0^{n\pi} f_{21}(\bar{y}) \left[ \int_0^{\infty} g_1(\bar{x}) \sum_{\nu=1}^3 \left\{ \frac{e^{-|(\tau-\bar{x})/\theta|}}{K_{\nu}^2 + \left(\frac{1}{FU_c}\right)^2 \left[ \left( \left| \frac{a\bar{z}}{m\pi} - U_c \tau \right| + U_c \bar{x} \right)^2 + \left(\frac{b\bar{y}}{n\pi}\right)^2 \right]} \right. \right. \right. \right.$$

$$\left. \left. \left. + \frac{e^{-|(\tau+\bar{x})/\theta|}}{K_{\nu}^2 + \left(\frac{1}{FU_c}\right)^2 \left[ \left( \left| \frac{a\bar{z}}{m\pi} - U_c \tau \right| + U_c \bar{x} \right)^2 + \left(\frac{b\bar{y}}{n\pi}\right)^2 \right]} \right\} d\bar{x} \right] d\bar{y} \right] dz$$

(13B)

$$f_{11}(\bar{z}) = f\left(\frac{a\bar{z}}{n\pi}\right)/b = \cos \bar{z} + \frac{1}{m\eta} (-|\bar{x}| \cos \bar{z} + \sin |\bar{z}|)$$

$$f_{21}(\bar{y}) = f\left(\frac{b\bar{y}}{n\pi}\right)/b = \cos \bar{y} + \frac{1}{n\pi} (\sin \bar{y} - \bar{y} \cos \bar{y})$$

$$g_1(\bar{x}) = e^{-a_{m,n}\bar{x}} \left[ \sin \omega_{m,n}\bar{x} + \frac{\omega_{m,n}}{a_{m,n}} \cos \omega_{m,n}\bar{x} \right]$$

$$-\left| \frac{x_0 - x'_0}{U_c \theta} \right|$$

Using the second kind of exponential  $e$  for the pressure correlation, and following the same procedure as in the above case, the final results becomes:

$$\left[ \overline{Y(x,y,t) Y(x',y',t')} \right] = \frac{\overline{p^2}}{2\pi^2 \sum_{\nu=1}^3 (A_{\nu}/K_{\nu}) \eta^2} \sum_{m,n} \frac{\phi_{m,n}(x,y) \phi_{m,n}(x',y')}{\omega_{mn} (a_{mn}^2 + \omega_{mn}^2)}$$

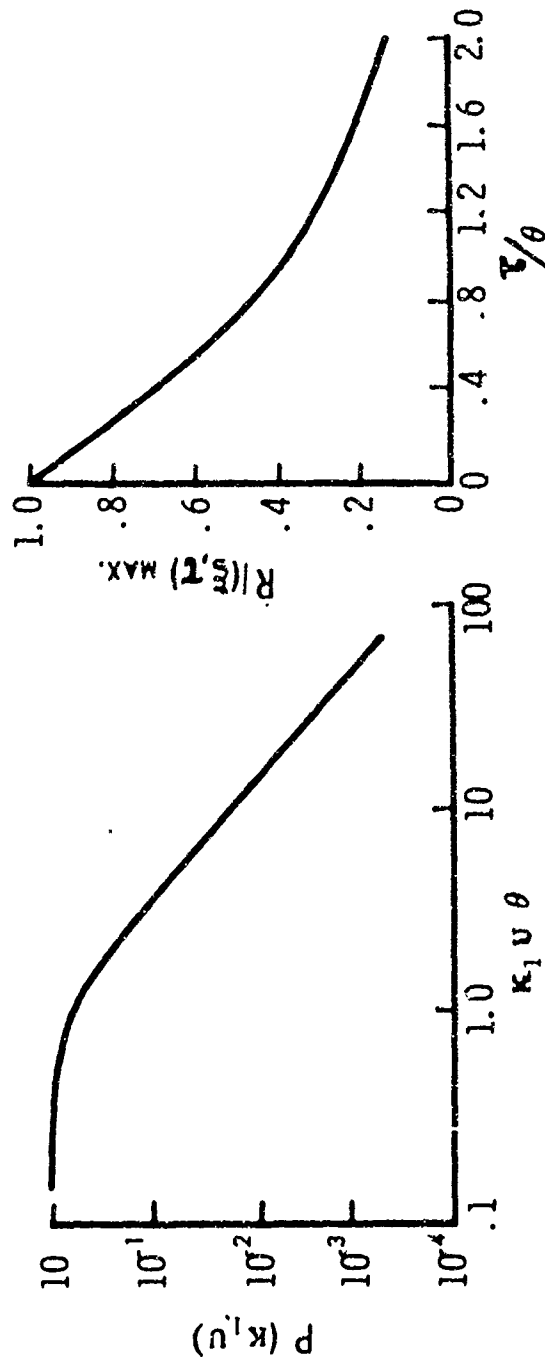
$$\cdot \int_{-m\pi}^{m\pi} f_{12}(\bar{z}) \left[ \int_0^{n\pi} f_{21}(\bar{z}) \left[ \int_0^{\infty} g_1(\bar{x}) \sum_{\nu=1}^3 \left\{ \frac{1}{K_{\nu}^2 + \left(\frac{1}{FU_c}\right)^2 \left[ \left(\left|\frac{a\bar{z}}{m\pi} - U_c \tau\right| + U_c \bar{x}\right)^2 + \left(\frac{b\bar{z}}{n\pi}\right)^2 \right]} + \frac{1}{K_{\nu}^2 + \left(\frac{1}{FU_c}\right)^2 \left[ \left(\left|\frac{a\bar{z}}{m\pi} - U_c \tau\right| - U_c \bar{x}\right)^2 + \left(\frac{b\bar{z}}{n\pi}\right)^2 \right]} \right\} d\bar{x} \right] d\bar{y} \right] d\bar{z}$$

where

$$f_{12}(\bar{z}) = f\left(\frac{a\bar{z}}{n\pi}\right)/b = \frac{\cos \bar{z} + \frac{1}{m\pi} (-|\bar{z}| \cos \bar{z} + \sin |\bar{z}|)}{e^{(a\bar{z}/m\pi U_c \theta)}}$$

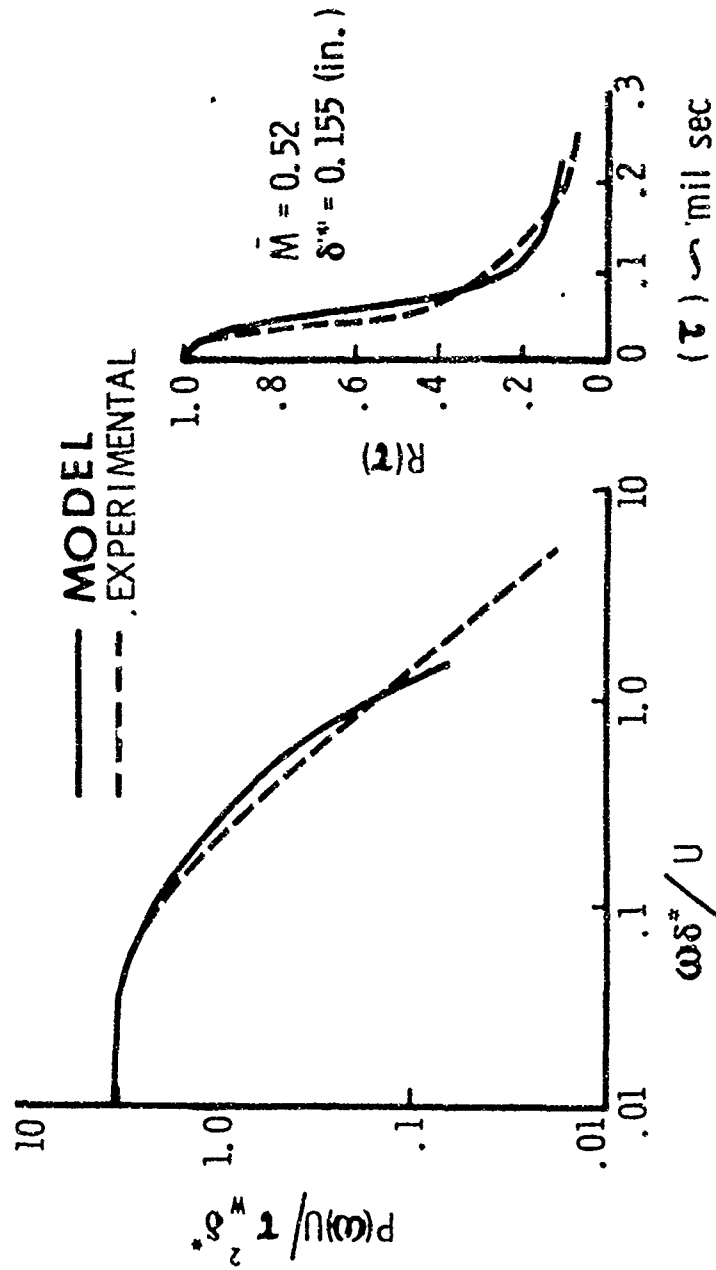
$$f_{21}(\bar{y}) = f\left(\frac{b\bar{y}}{n\pi}\right)/b = \cos \bar{y} + \frac{1}{n\pi} (\sin \bar{y} - \bar{y} \cos \bar{y}) \quad (14B)$$

$$g_1(\bar{x}) = e^{-a_{m,n}\bar{x}} \left[ \sin \omega_{m,n}\bar{x} + \frac{\omega_{m,n}}{a_{m,n}} \cos \omega_{m,n}\bar{x} \right]$$



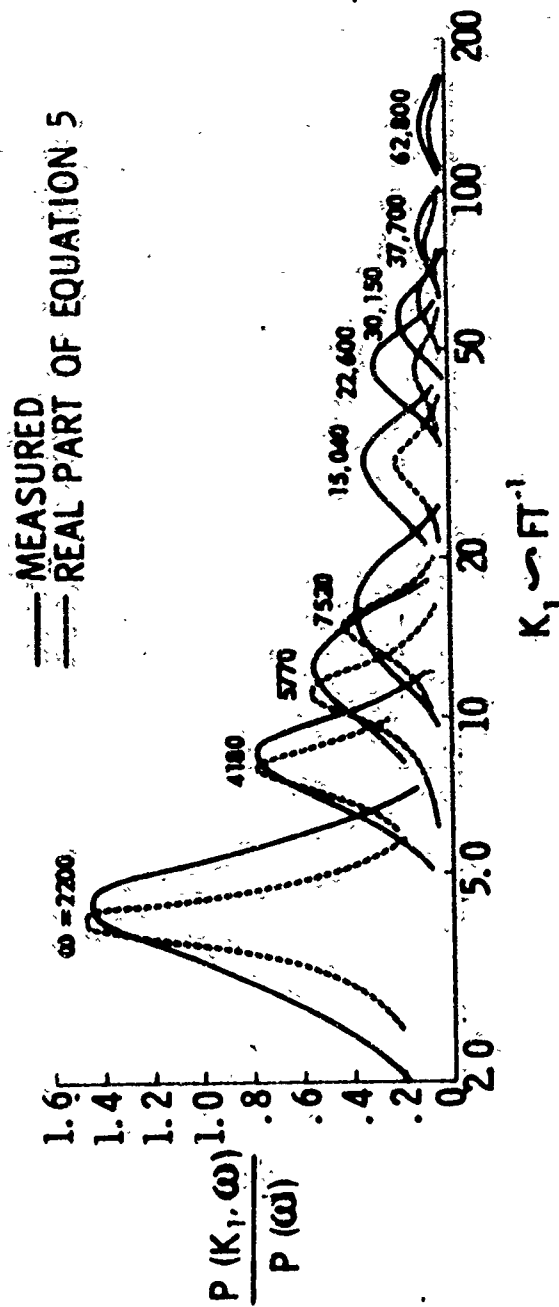
**Moving Frame  
Spectrum  
Eddy Lifetime**

FIGURE 1



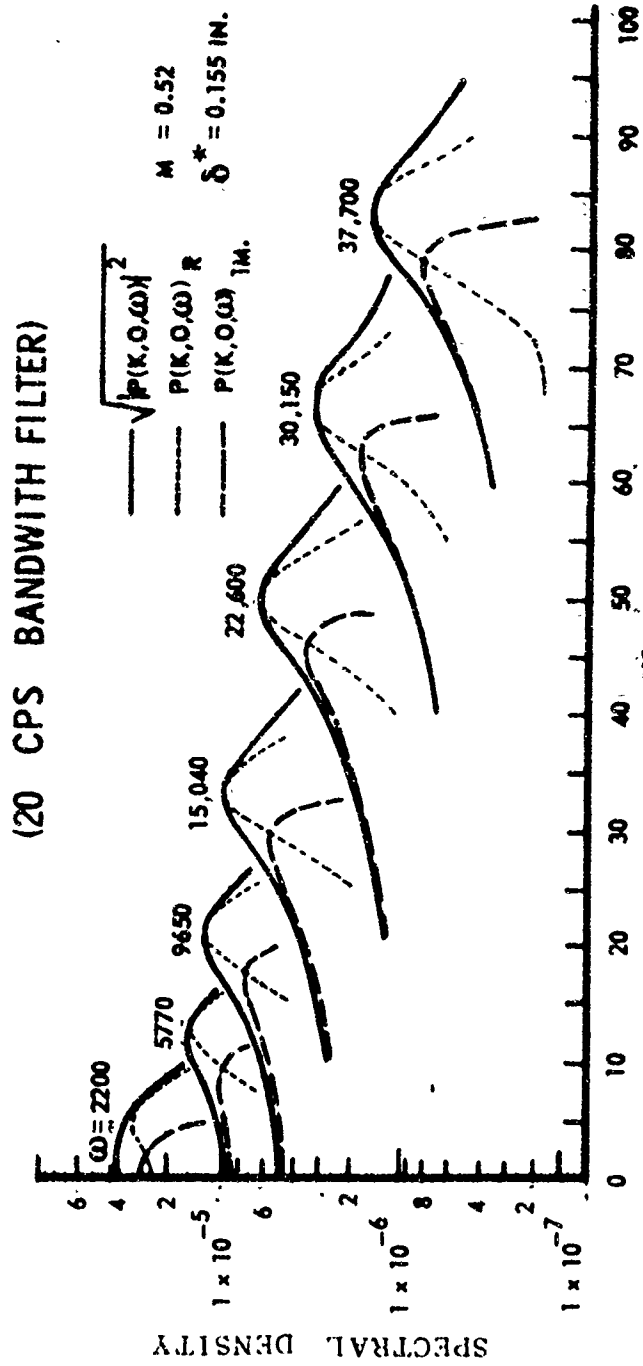
**Dimensionless Power Spectrum  
and Autocorrelation  
of the Wall Pressure Fluctuations**

FIGURE 2



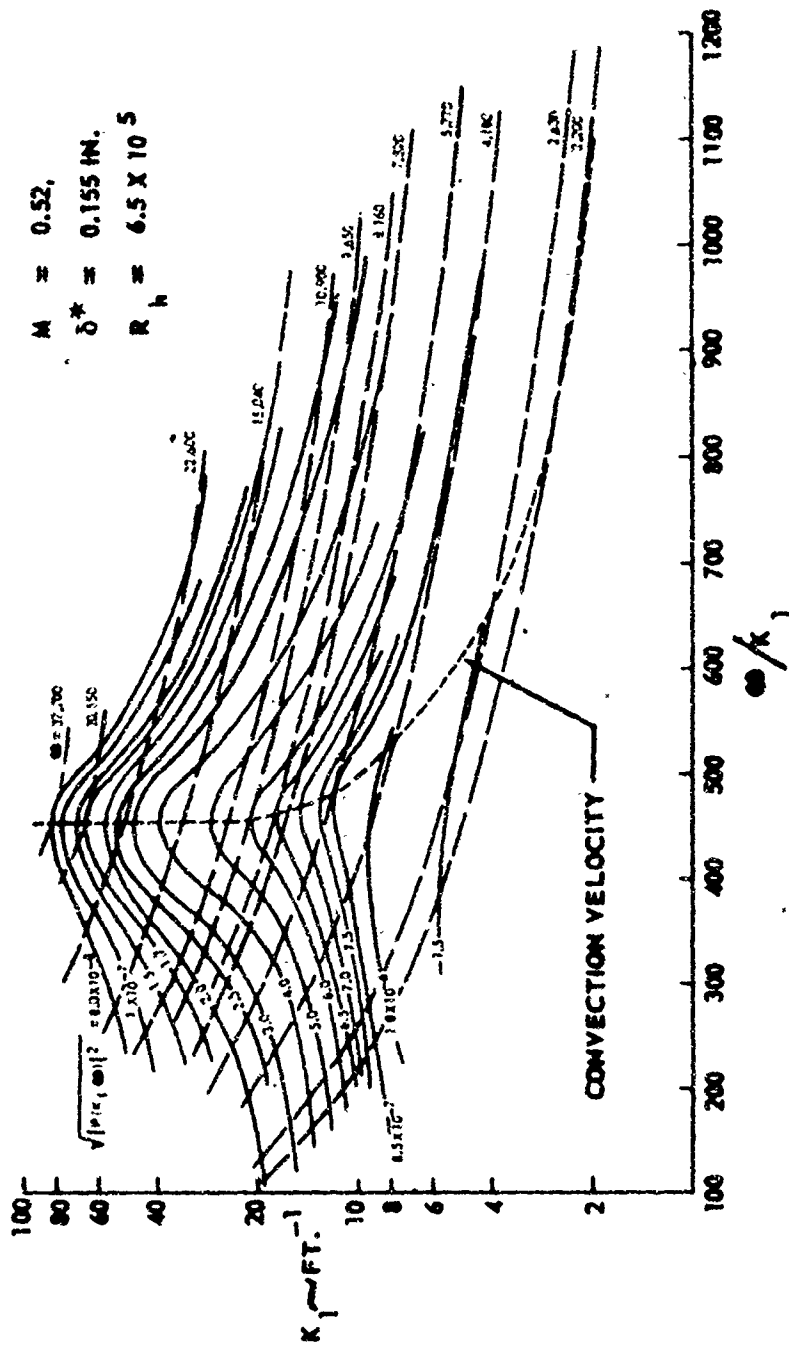
**Comparison of Co-Power Spectral Density,  
 $M = 0.52, \delta = 0.155 \text{ In.}, R_b = 6.5 \times 10^5$**

FIGURE 3



Comparison Between Co-Quad-Absolute  
Power Spectral Density from Model

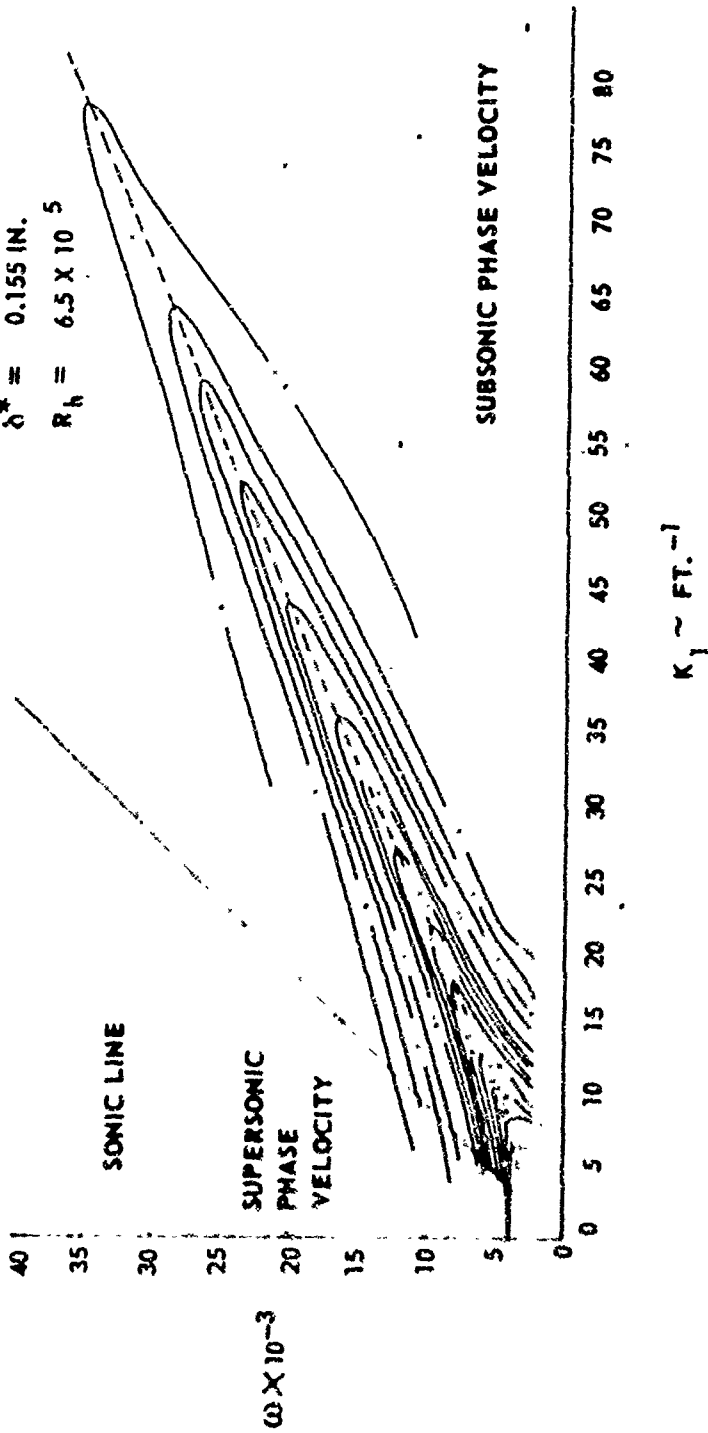
FIGURE 4



**Map of Longitudinal Cross Power  
 Spectrum Density from Model**

FIGURE 5

$M = 0.52$   
 $\delta^* = 0.155 \text{ IN.}$   
 $R_h = 6.5 \times 10^5$



## Contour Map of the Longitudinal Cross Power Spectrum Density from Model

FIGURE 1

SHEET 1

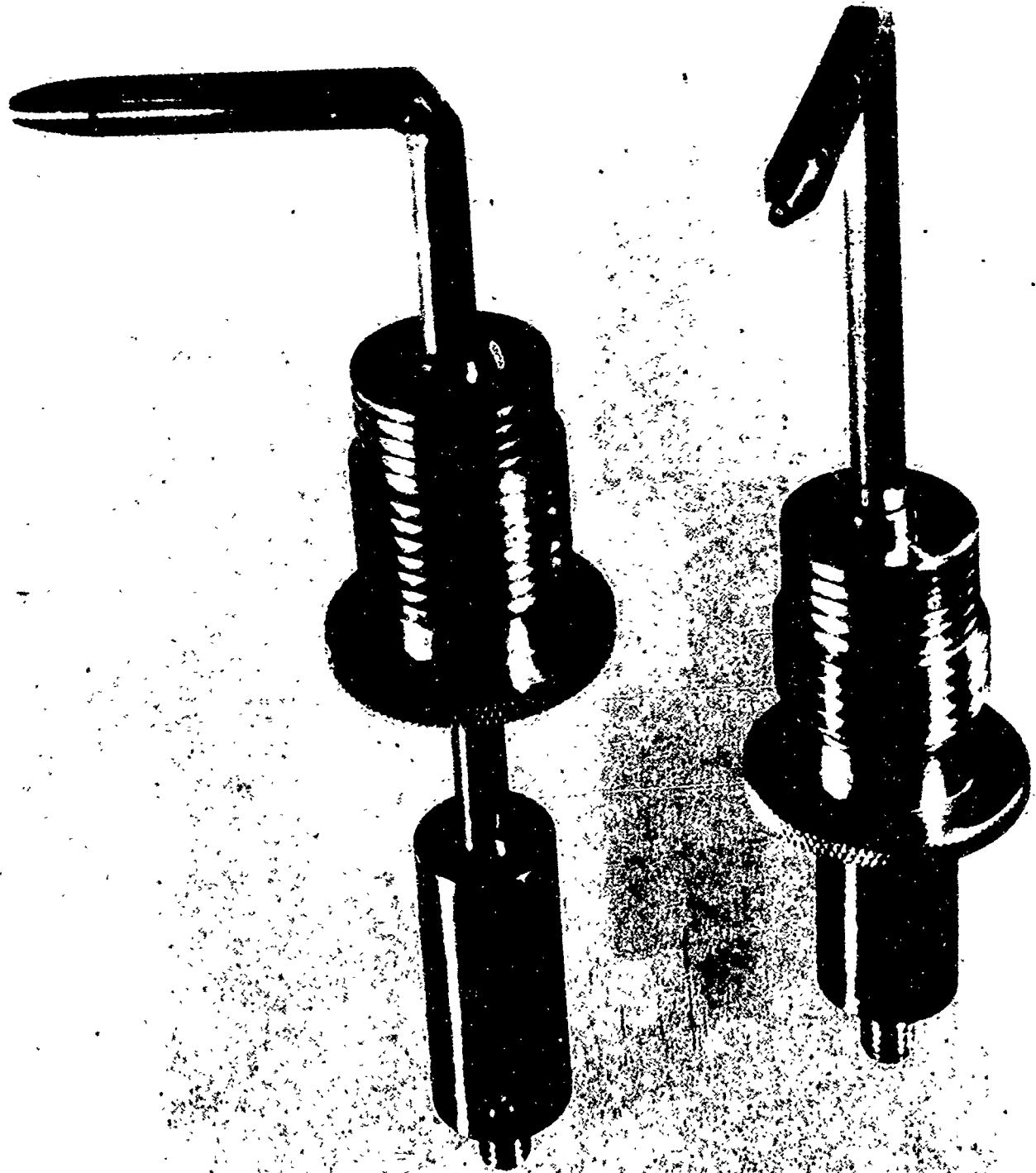
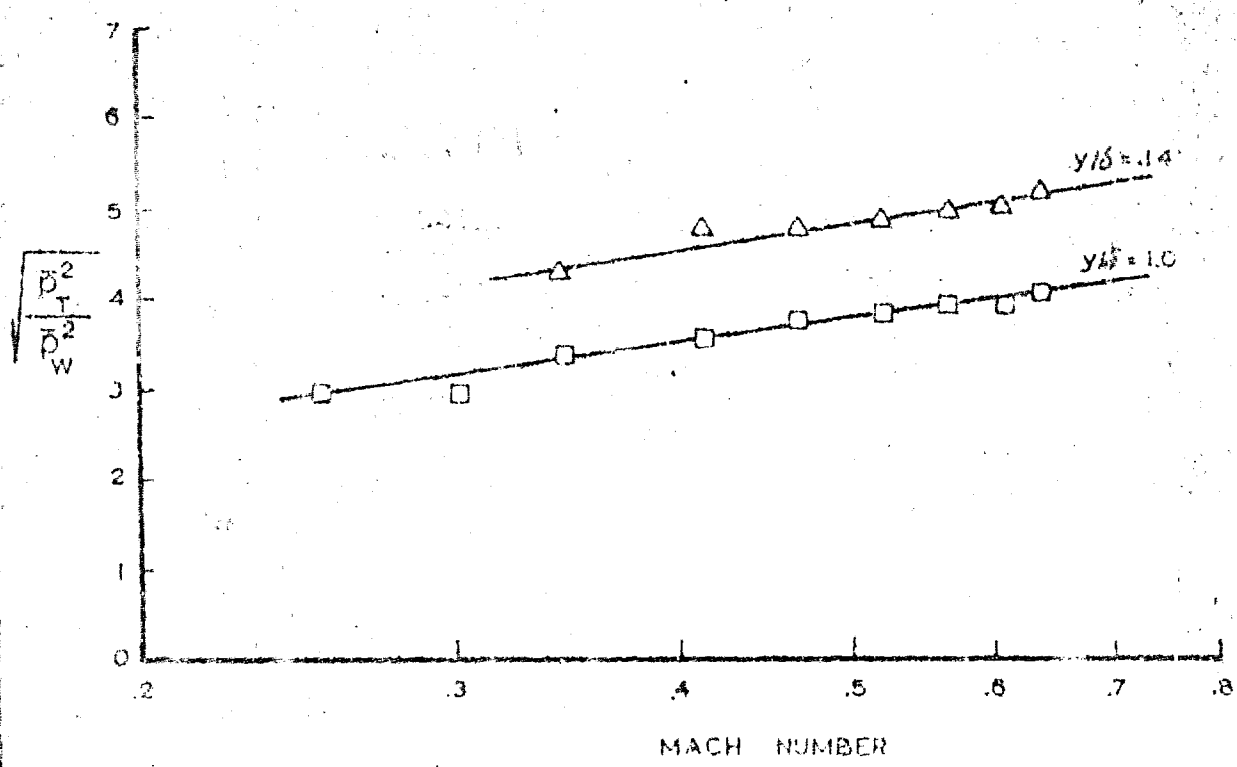
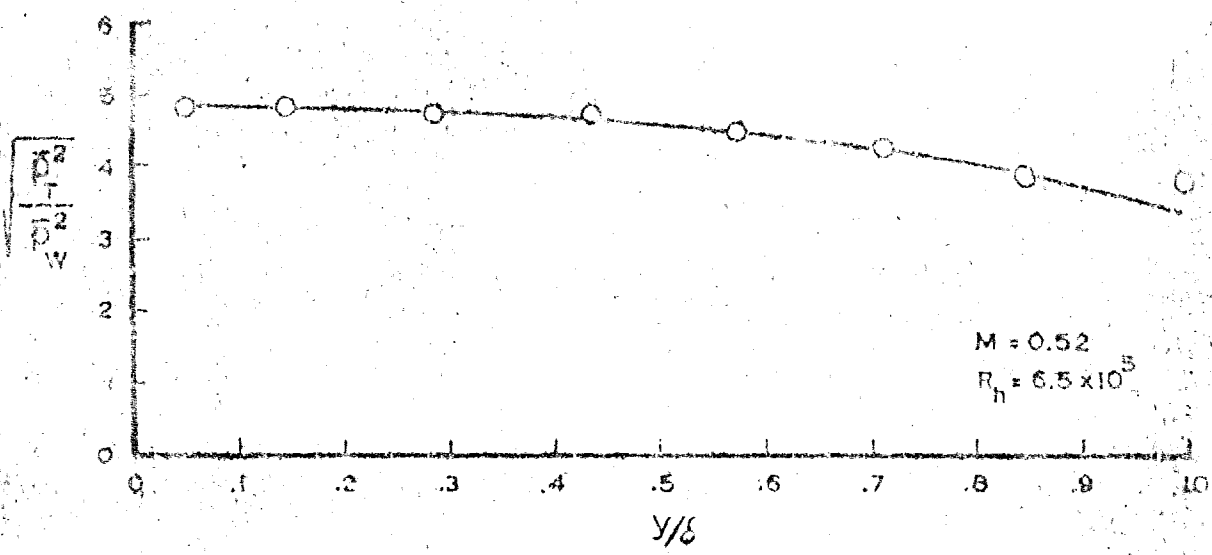


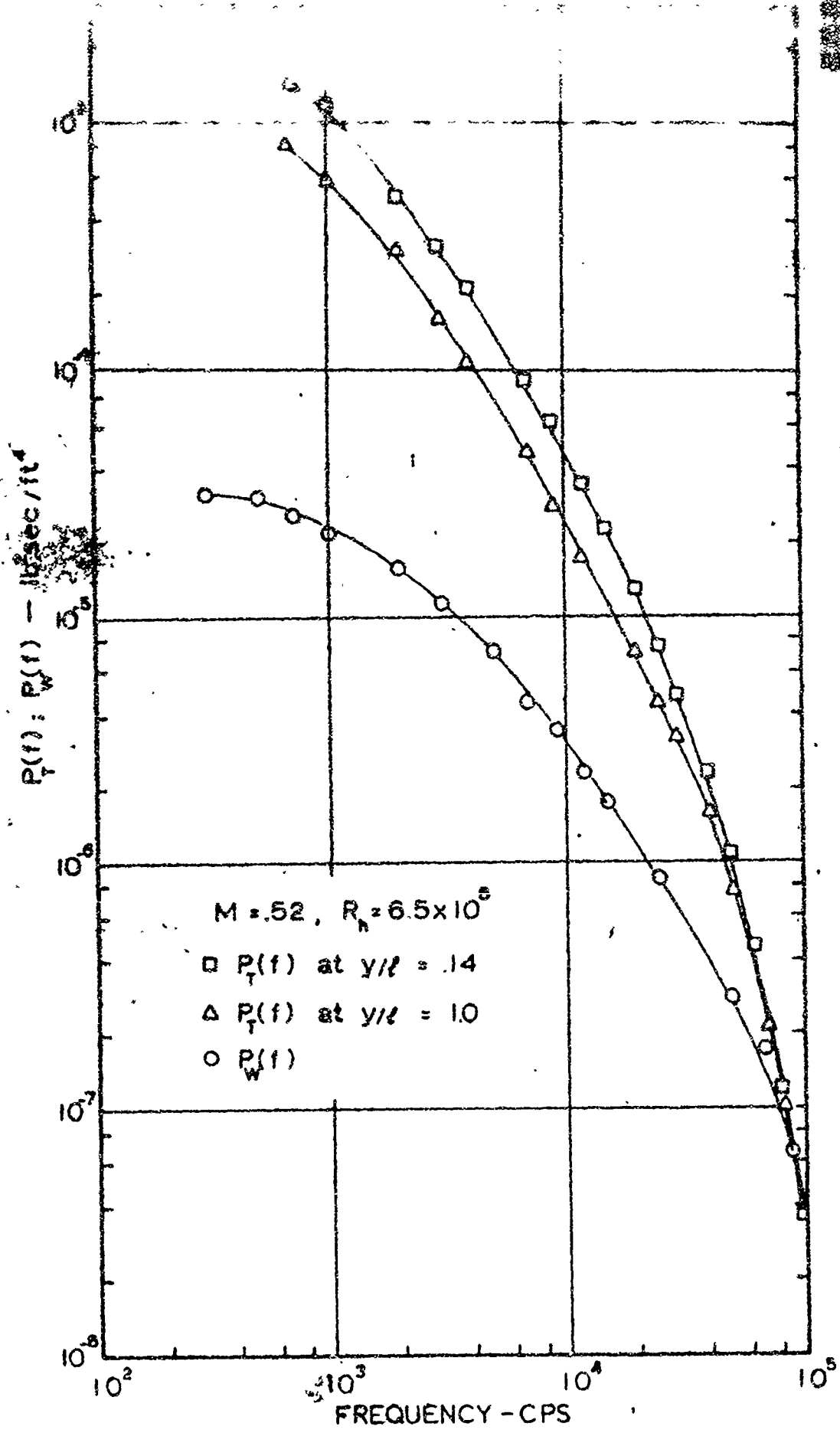
FIG.7

TOTAL PRESSURE PROBE

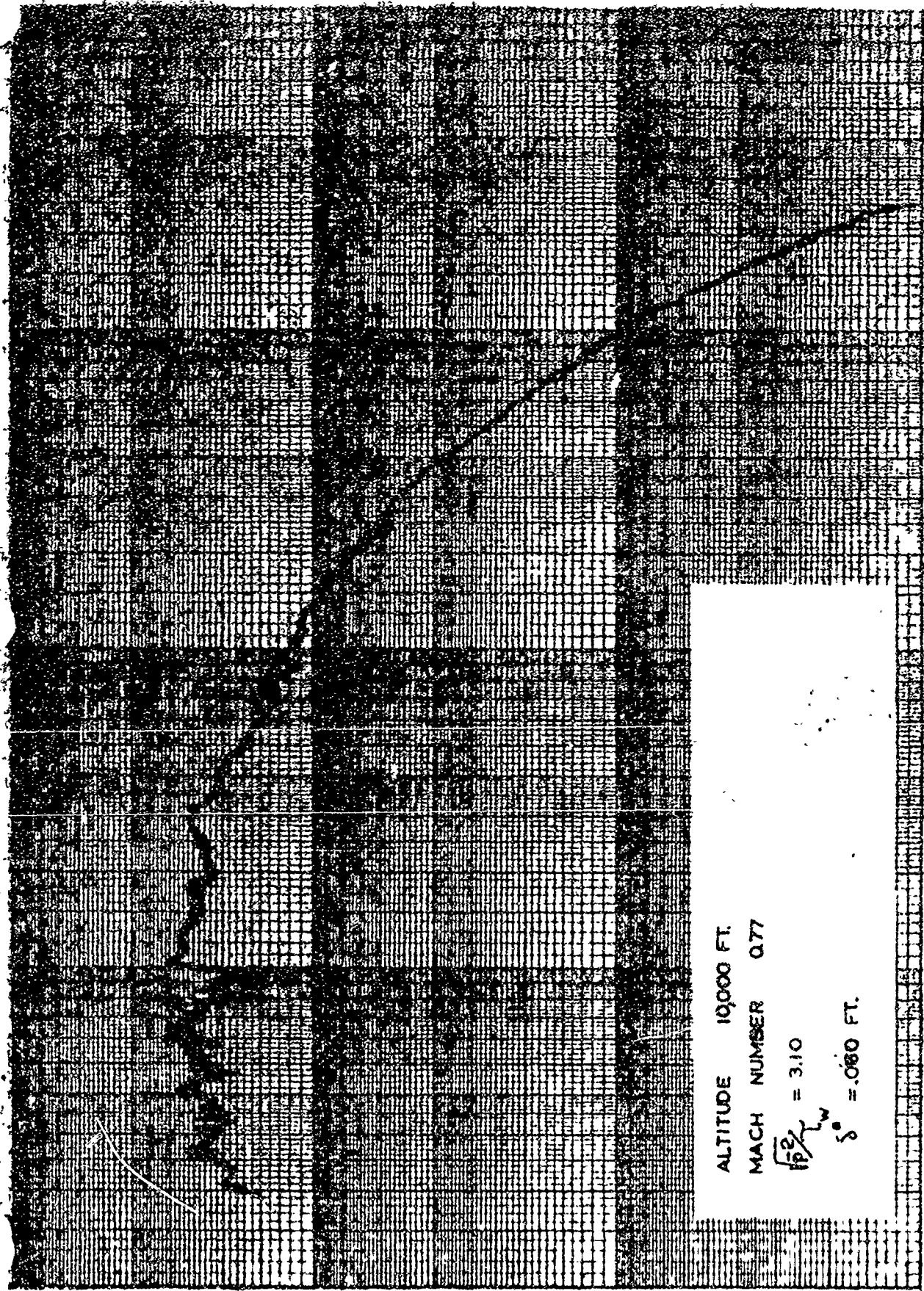


CALC		REVISED	DATE	TOTAL PRESSURE FLUCTUATION	DO-0941 -
CHECK					VOL. III
APPD					FIG. 8
APPD					PAGE 53
				THE <del>RESEARCH</del> COMPANY RENO, WASHINGTON	5-1000

**BEST  
AVAILABLE COPY**



POWER SPECTRA OF TOTAL & WALL PRESSURES



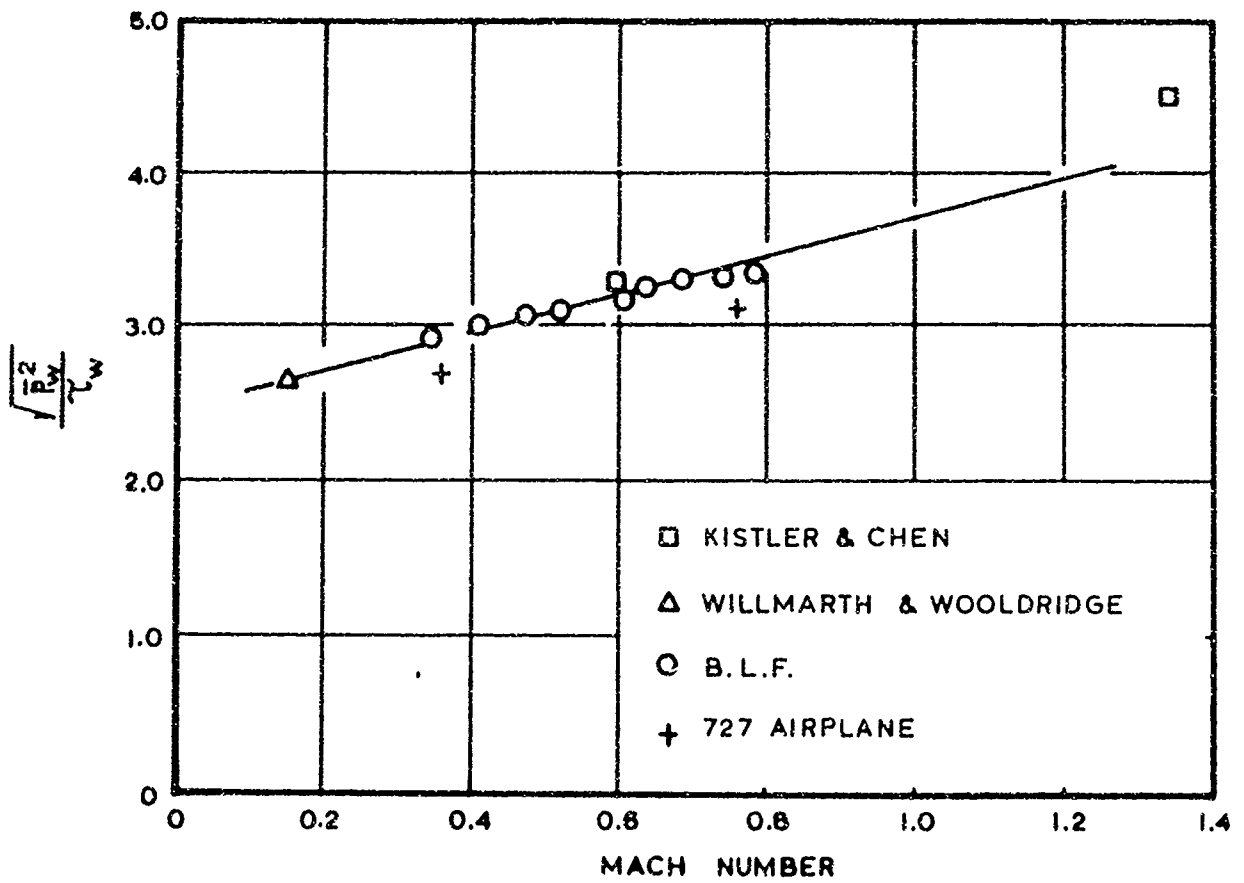
ALTITUDE 10000 FT.  
 MACH NUMBER 0.77  
 $\sqrt{\frac{2}{\rho}} L_w = 3.10$   
 $\delta = .060$  FT.

100000 10000 1000 100 0

FREQUENCY — CPS  
 WALL PRESSURE FLUCTUATION ON THE 727 AIRPLANE

$P(f) \sim (\frac{lb}{ft^2})^2 / cps$

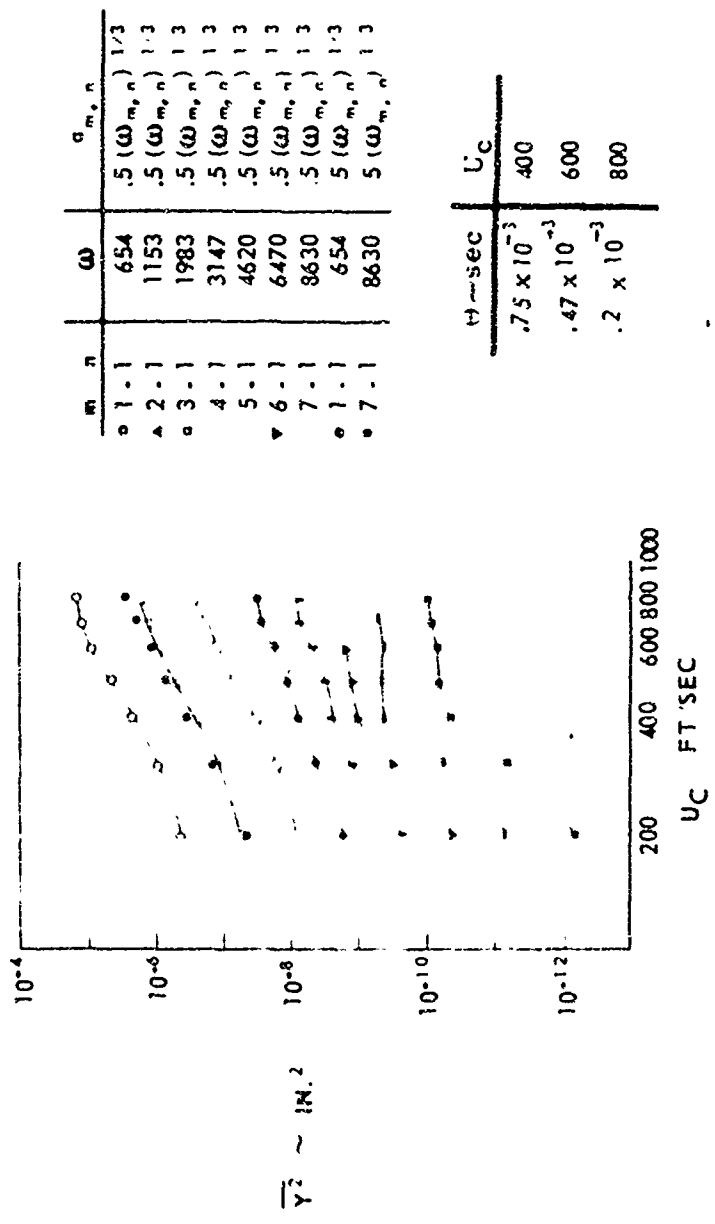
100000 10000 1000 100 0



WALL PRESSURE FLUCTUATION

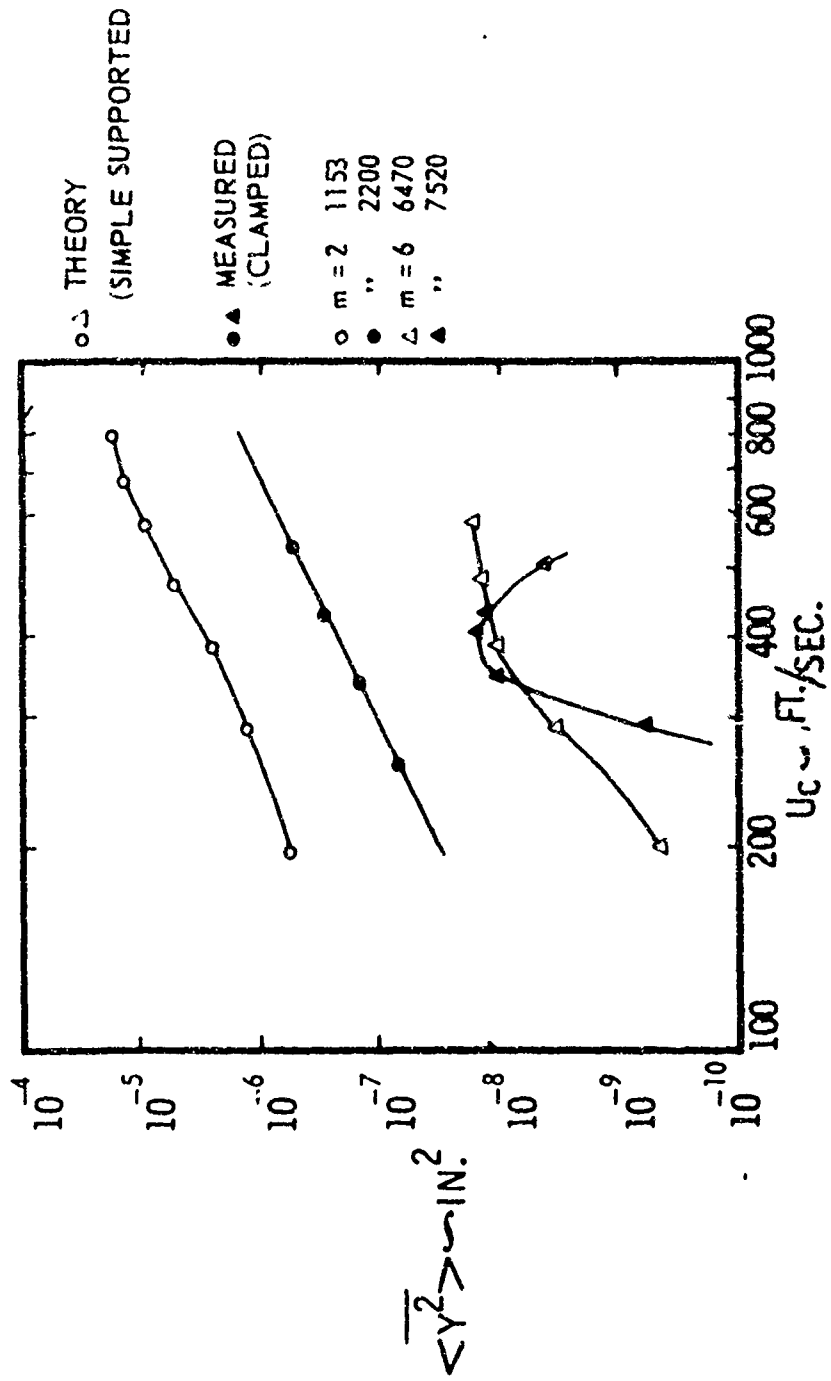
FIGURE 11

SHEET 61



Mean Square Displacement of  
 12" x 7" x .040"  
 Simple Supported Panel from Theory

FIGURE 12



**Mean Square Displacement  
of 12" x 7" x .040" Panel**

FIGURE 13

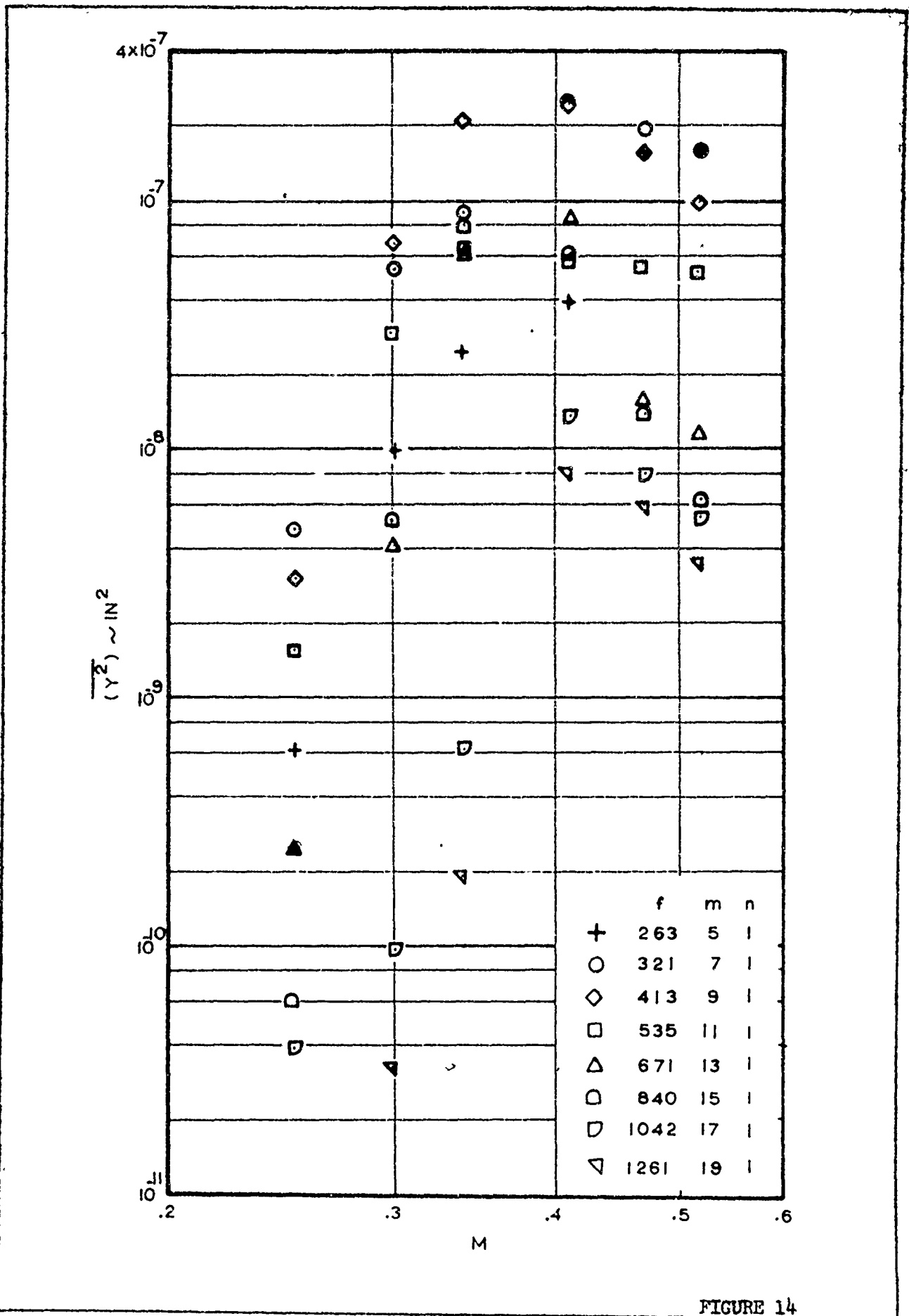


FIGURE 14

TD 1544 L-R3

MODAL MEAN SQUARE DISPLACEMENT  
OF A 36x6.5x0.04" PANEL FROM EXPERIMENT

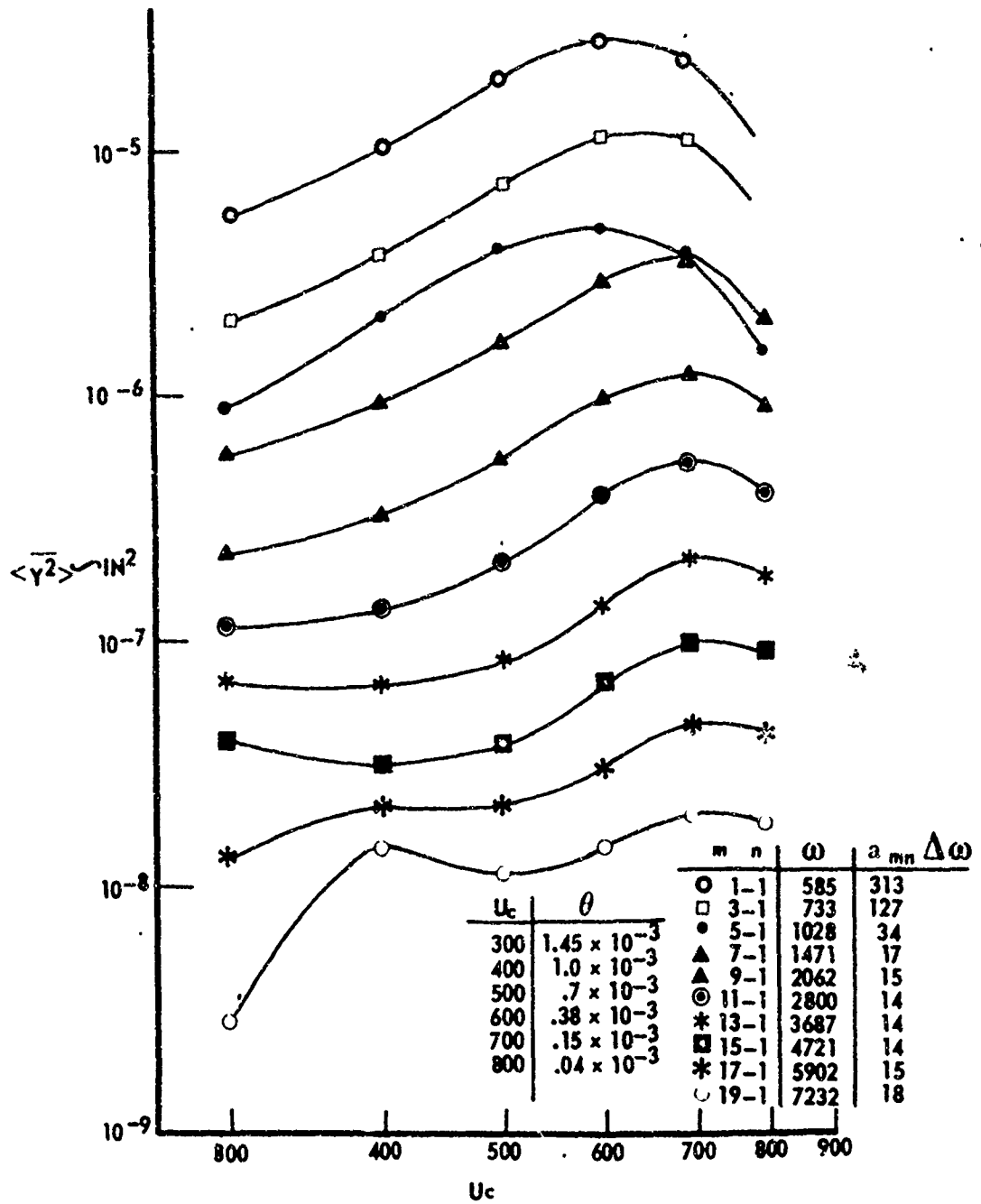
**BOEING**

NO. D6-9944 - VOL. III

PAGE 64

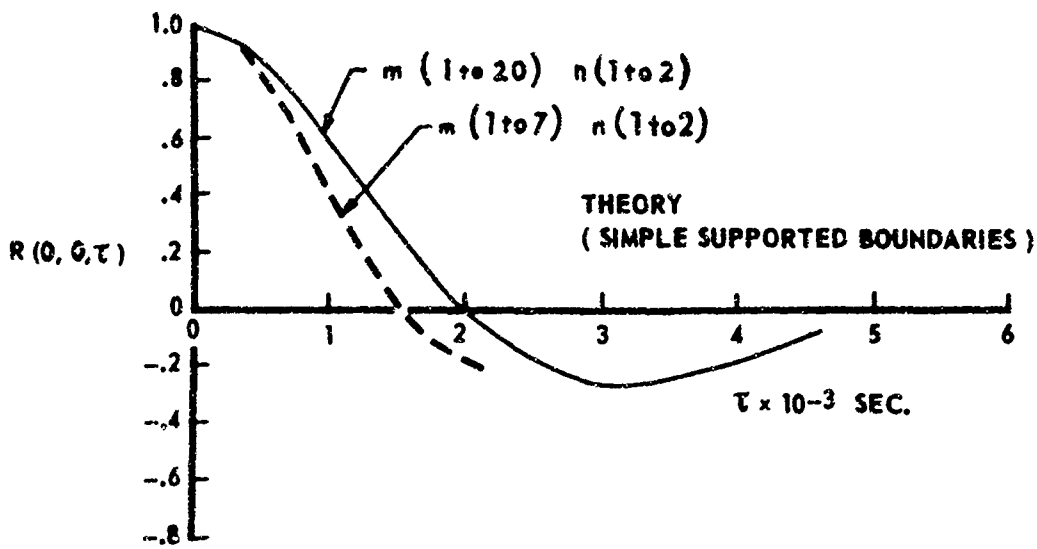


6-7000



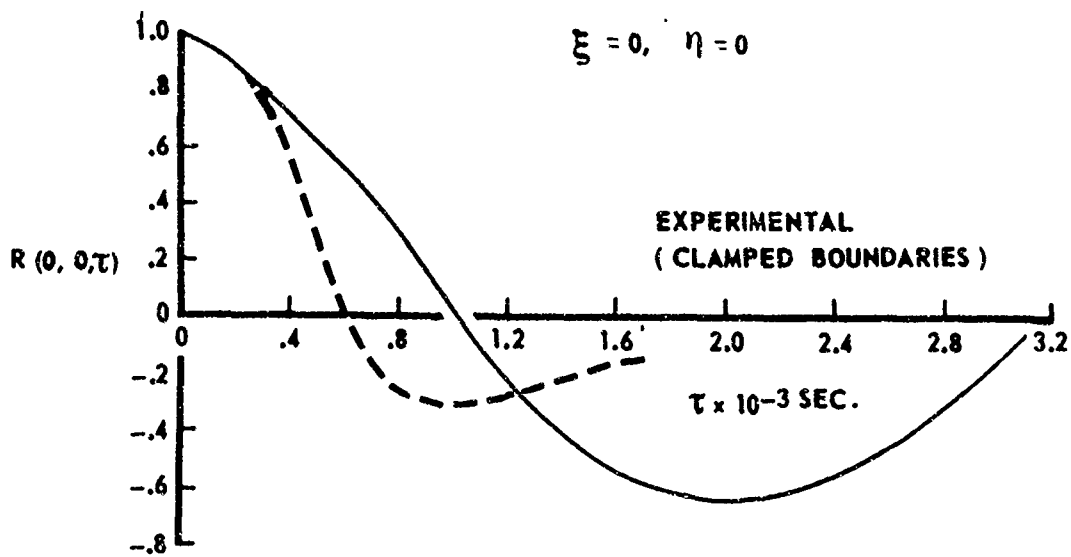
Mean Square Displacement From  
Theory Of a 36" x 6.5" x .040 Panel

FIGURE 15



---  $12'' \times 7'' \times .040'' \quad x = x' = 6'' \quad y = y' = 3.5''$   
—  $36'' \times 6.5'' \times .040'' \quad x = x' = 18'' \quad y = y' = 3.25''$

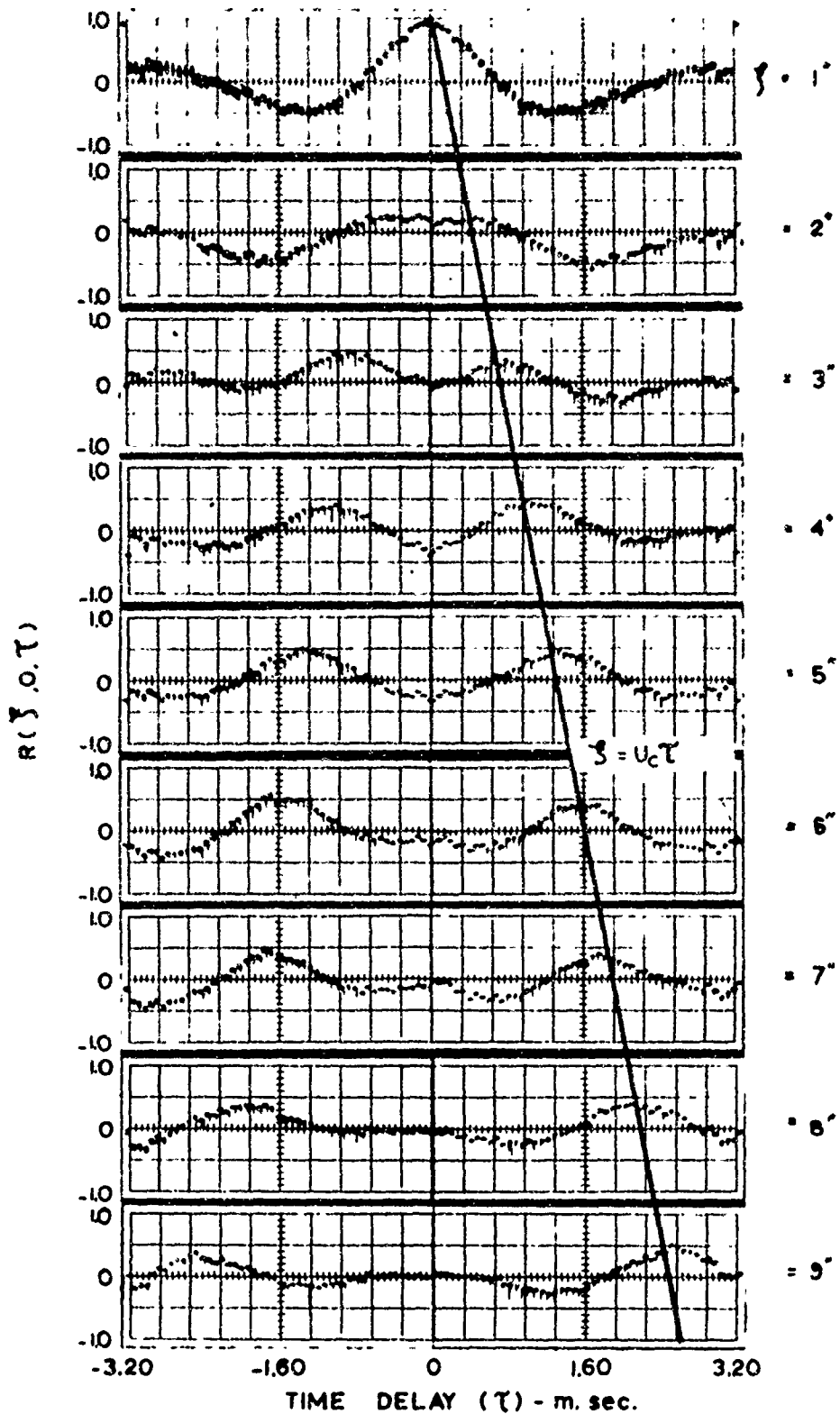
$\xi = 0, \quad \eta = 0$



## Broad Band Displacement Space - Time Correlation

$M = 0.52 \quad S^* = 0.155 \text{ IN.}$

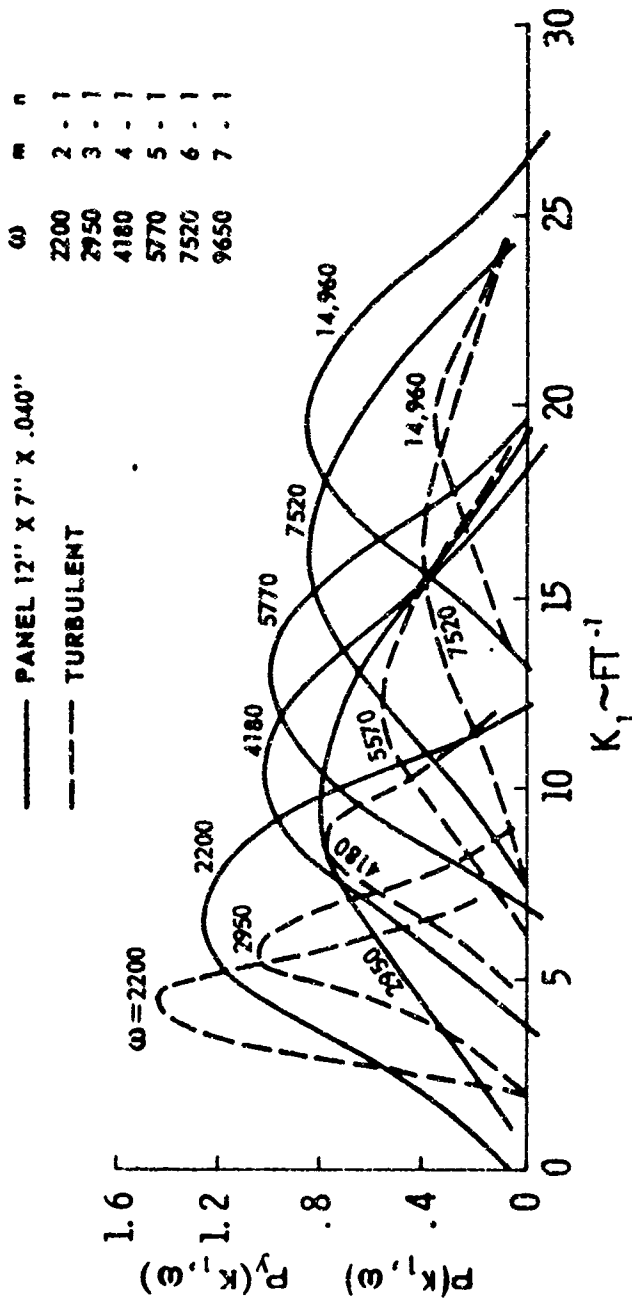
FIGURE 16



LONGITUDINAL SPACE-TIME CORRELATION  
OF THE DISPLACEMENT OF A 36x6.5x0.04" PANEL  
(M=0.34)

FIGURE 17

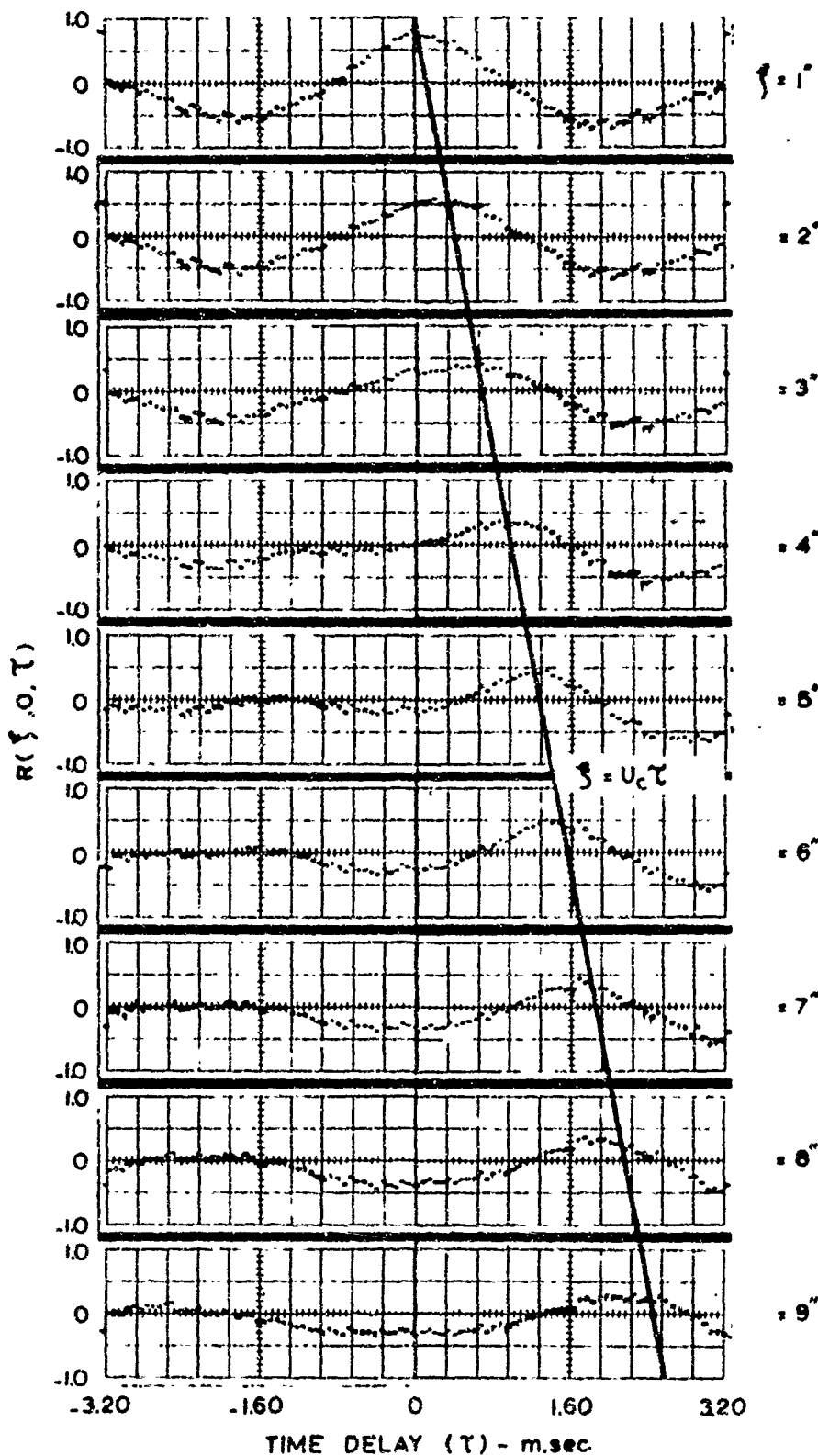
SHEET 67



**Experimental Co-Power Spectral  
Density For Turbulence And Panel,  
 $M = 0.52, \delta^* = 0.155$  In.,  $R_h = 6.5 \times 10^5$**

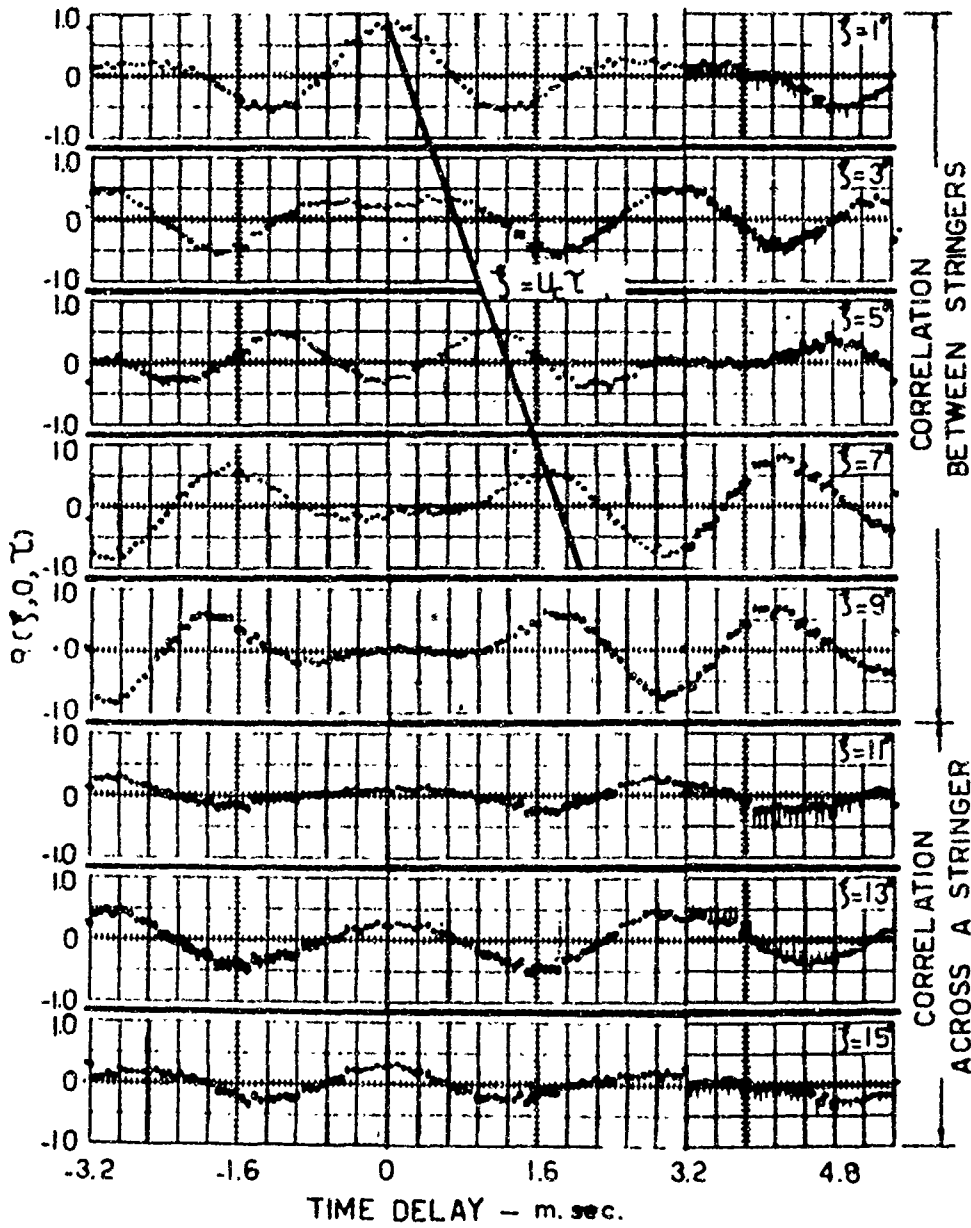
FIGURE 1F

SHEET 63



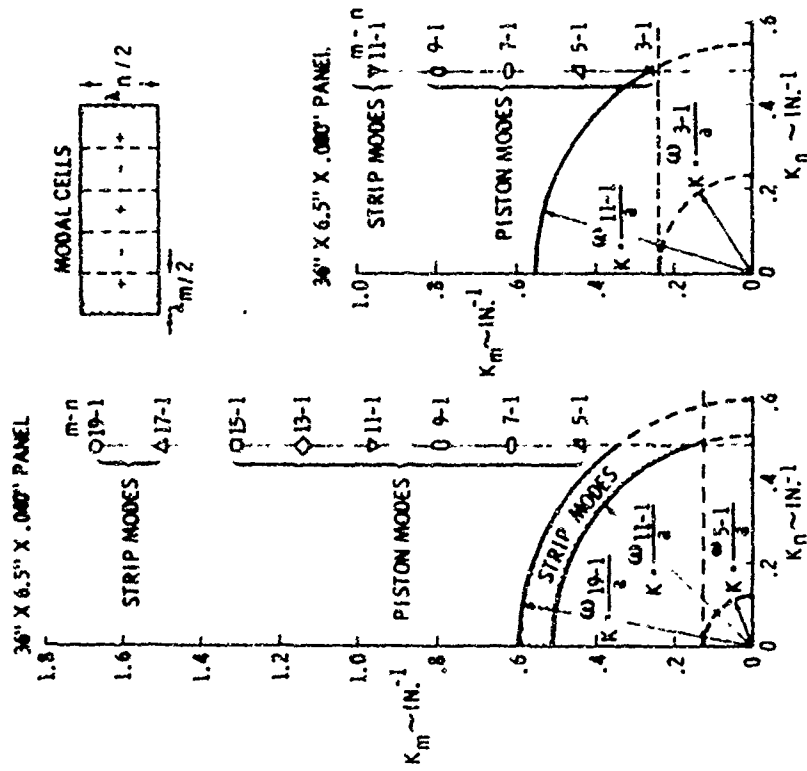
LONGITUDINAL SPACE-TIME CORRELATION  
OF THE DISPLACEMENT OF A 36x6.5x0.04 PANEL  
WITH DOWNSTREAM END DAMPED (  $M = 0.34$  )

FIGURE 19



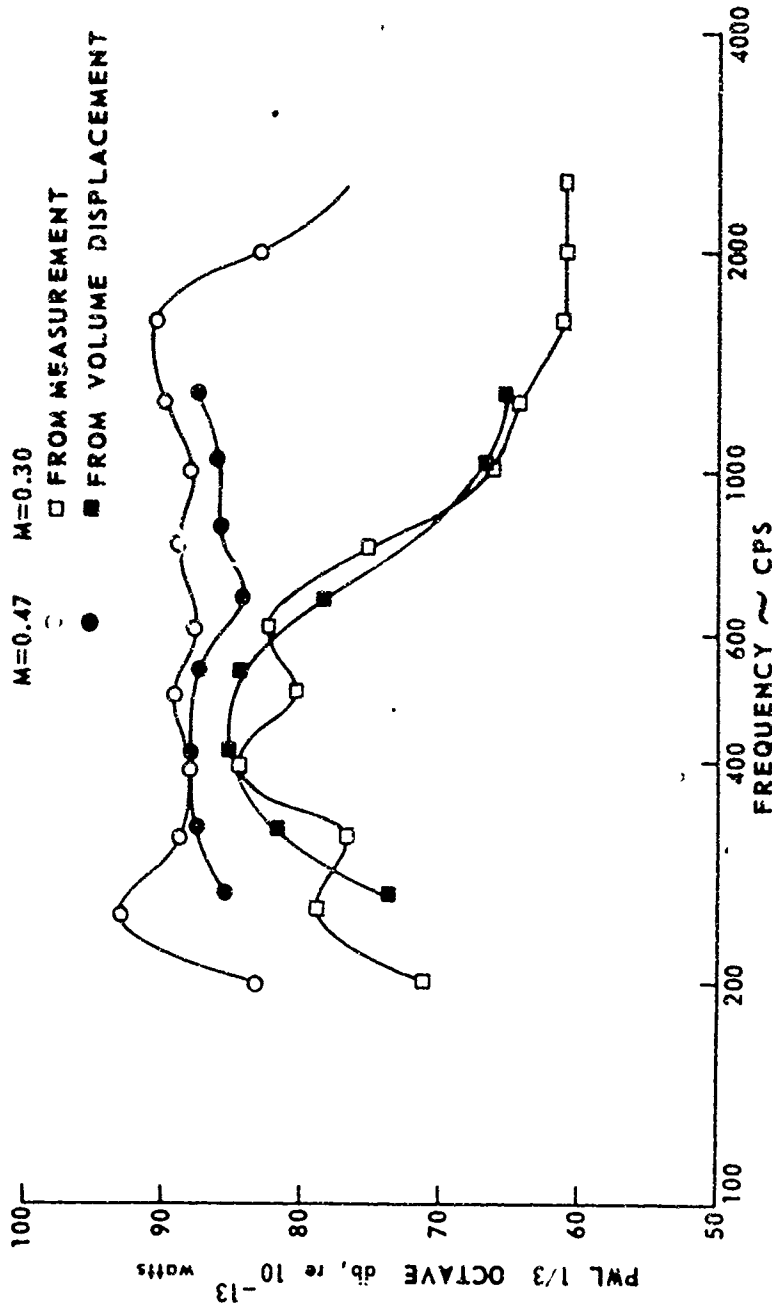
DISPLACEMENT CORRELATION OF THE  
36" x 6.5" x .040" PANEL

FIGURE 20



Modal Radiation in K-Space

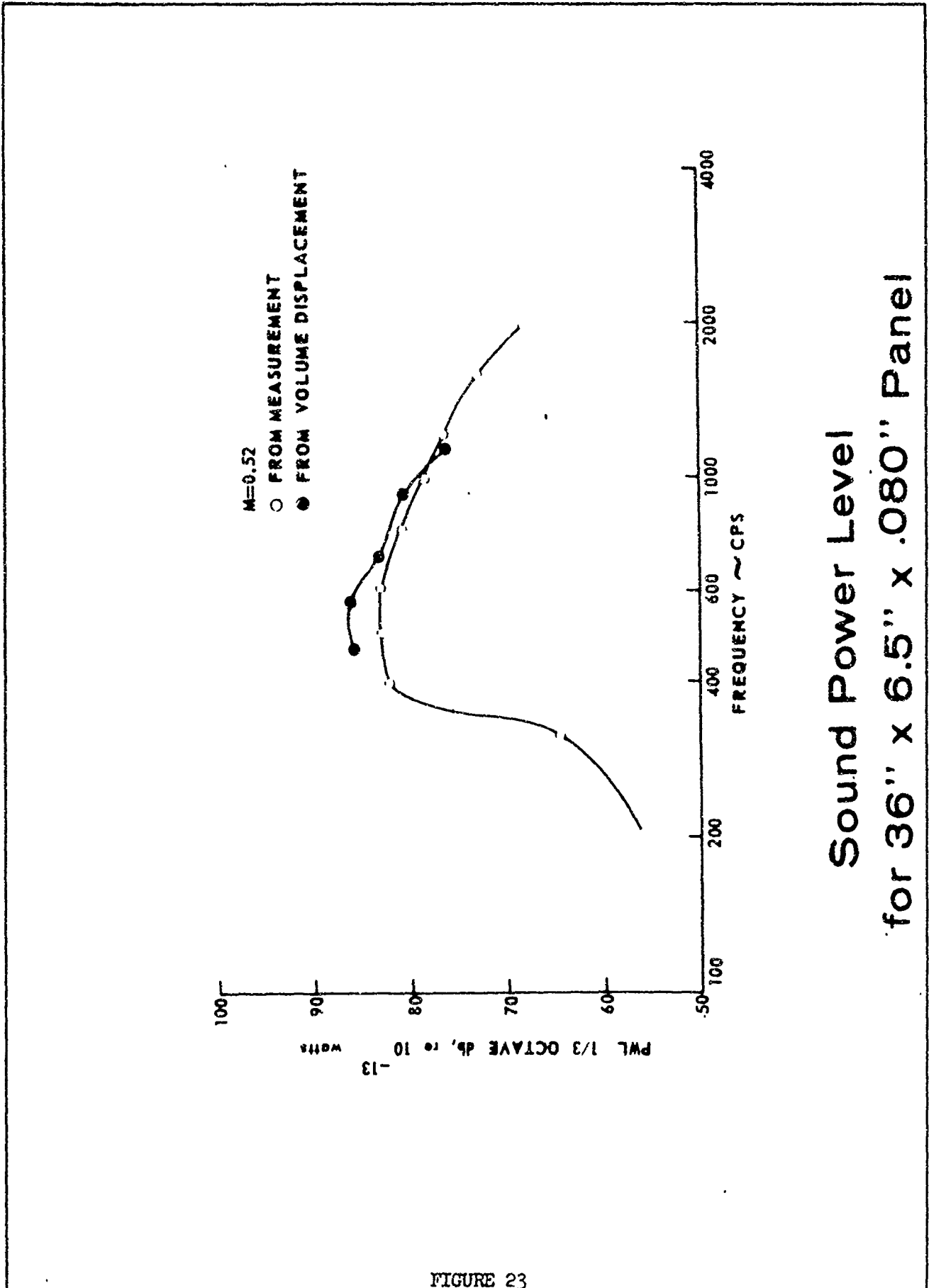
FIGURE 21



Sound Power Level  
for 36" x 6.5" x .040" Panel

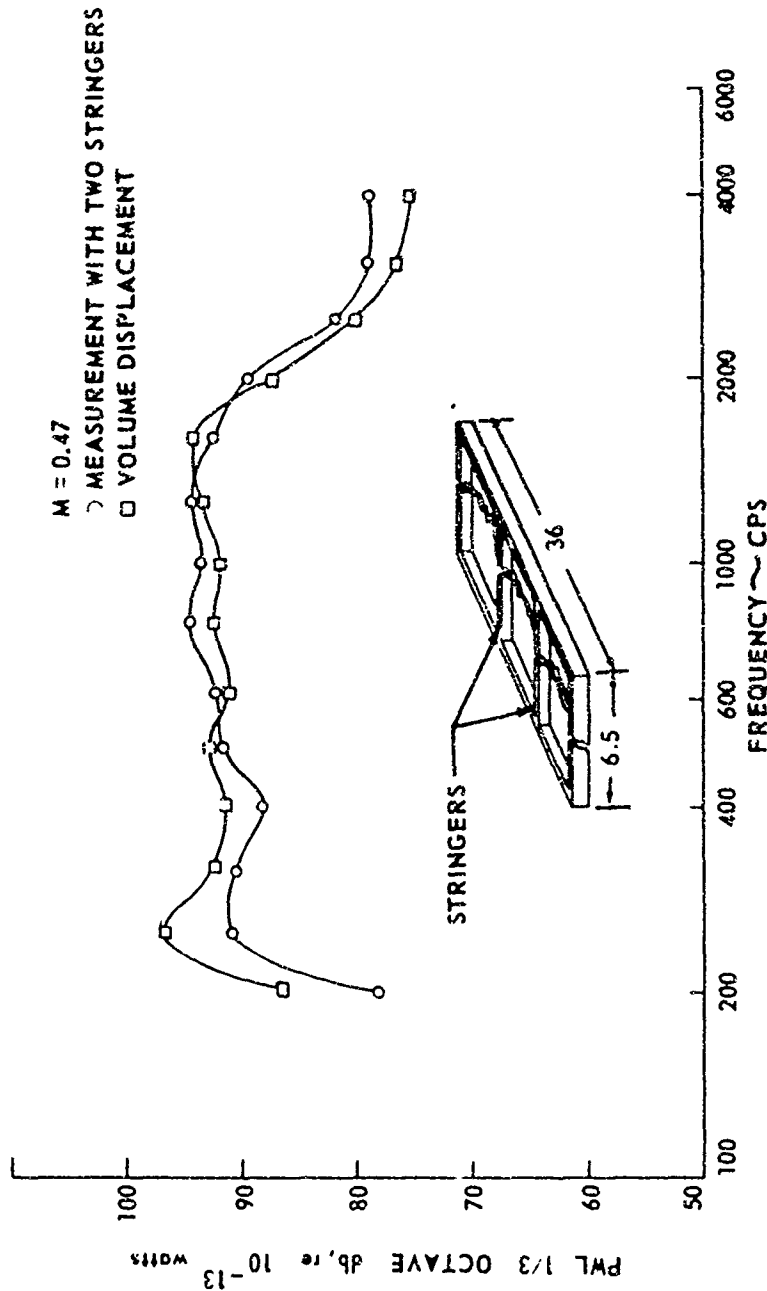
FIGURE 22

SHEET 72



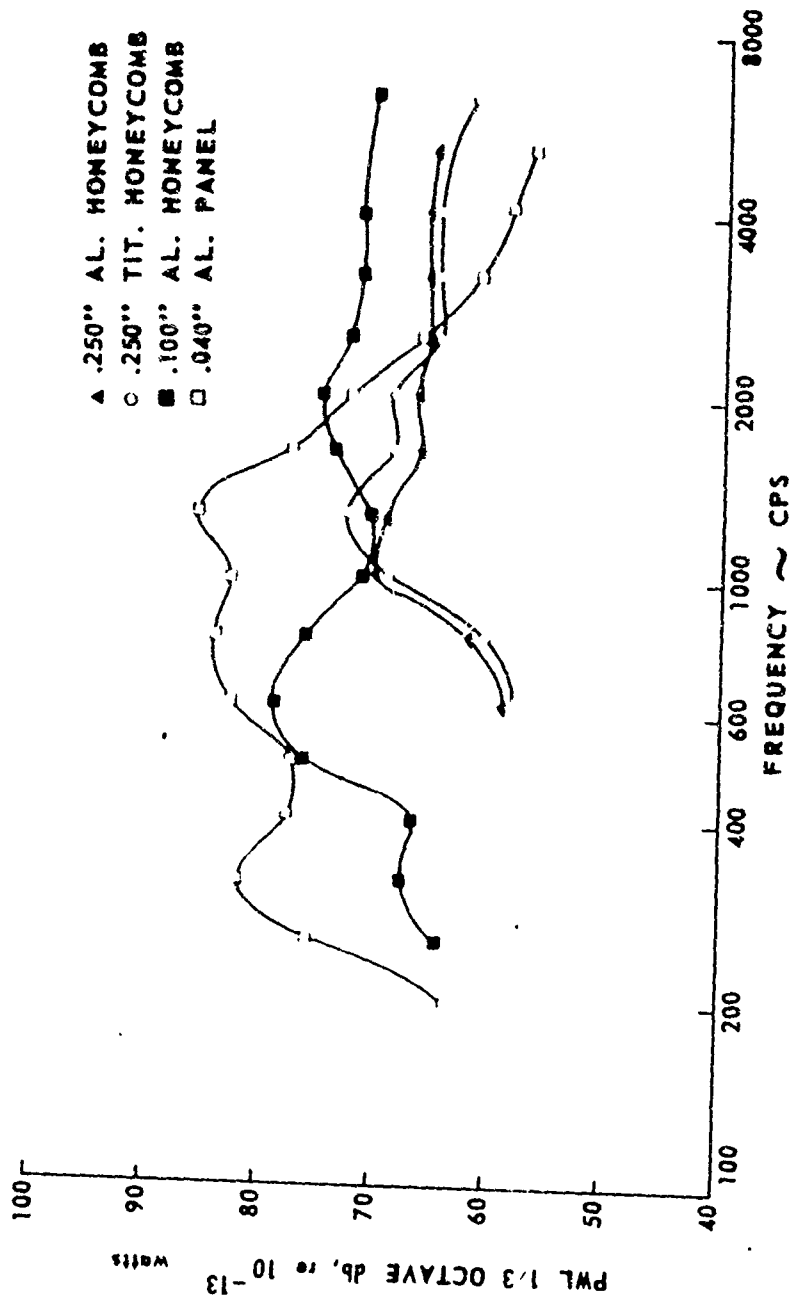
Sound Power Level  
for 36" x 6.5" x .080" Panel

FIGURE 23



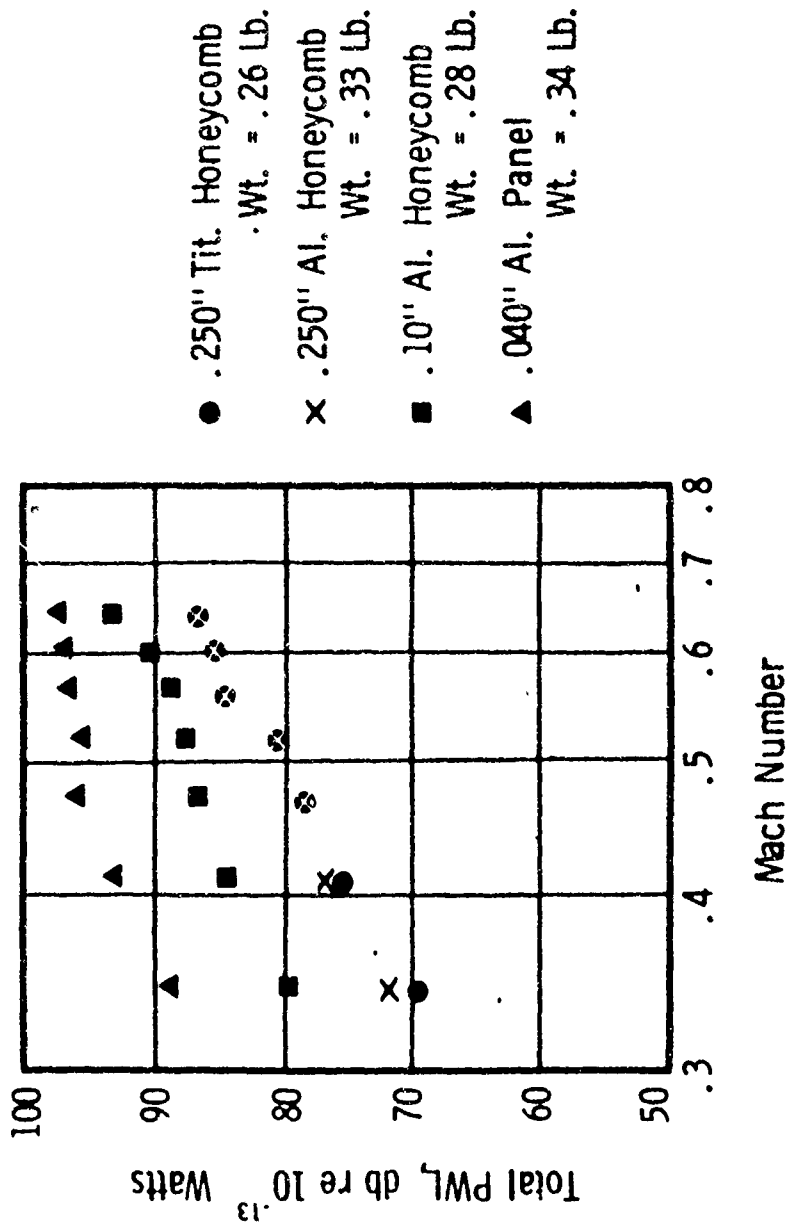
Sound Power Level of 36" x 6.5" x .040"  
Panel with Two Equally Spaced Stringers

FIGURE 24



Sound Power Level for 7" x 12" Panels  
at M = 0.47

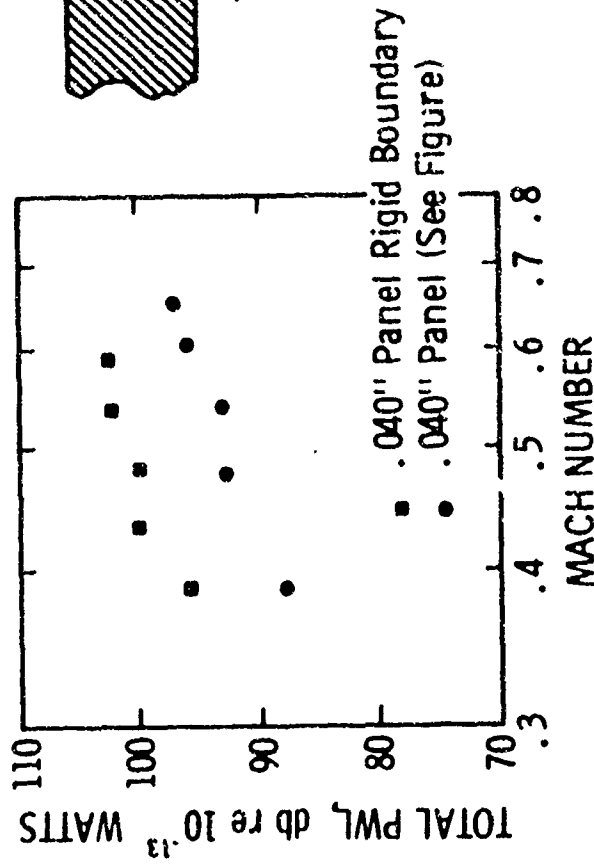
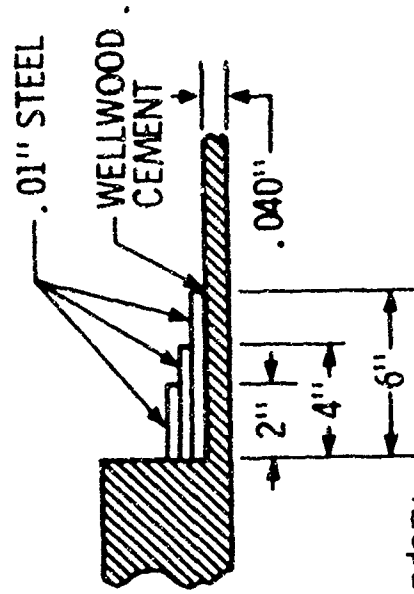
FIGURE 25



**Total Acoustic Power (7" x 12" Panels)**

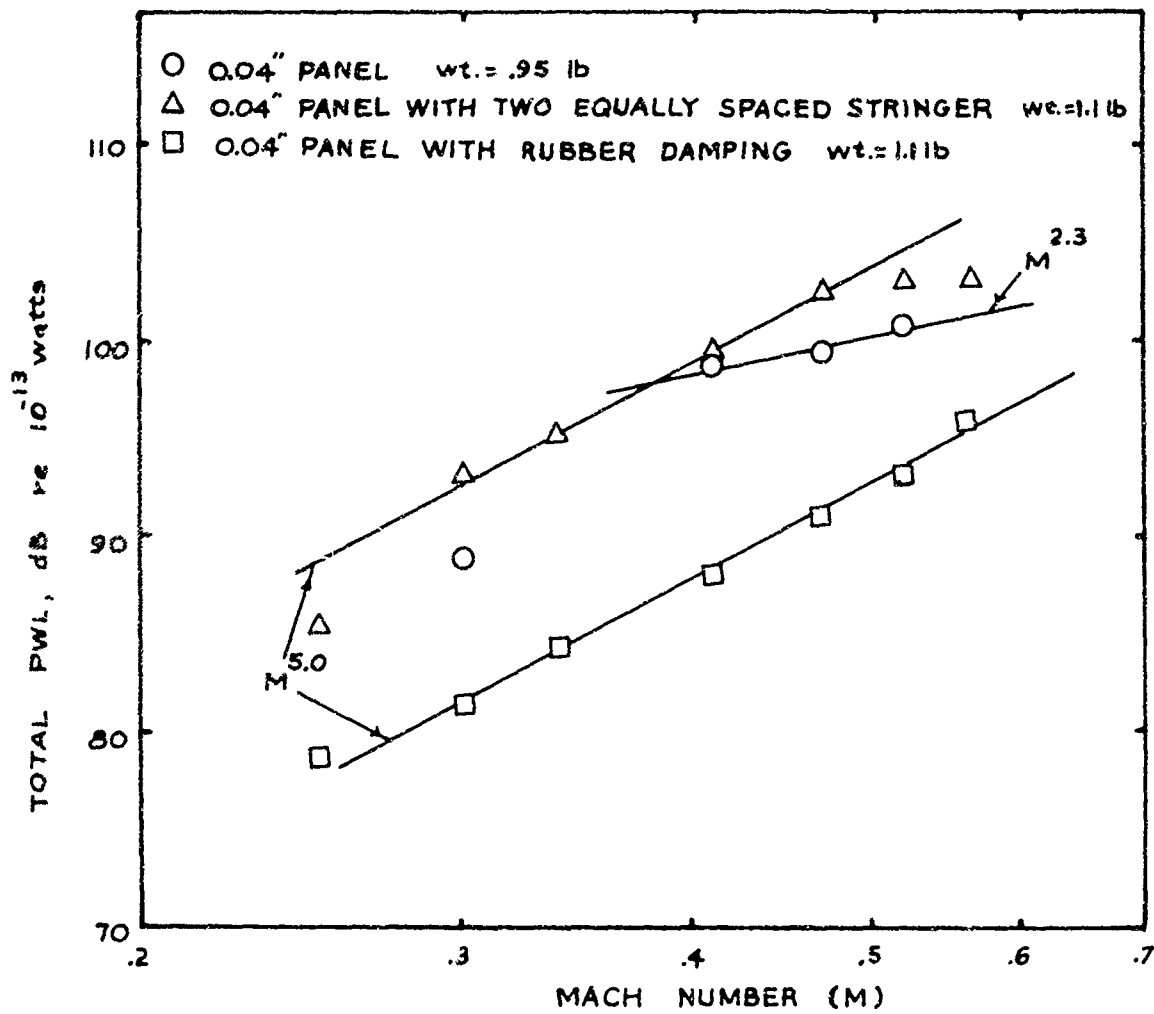
FIGURE 26

SHEET 76

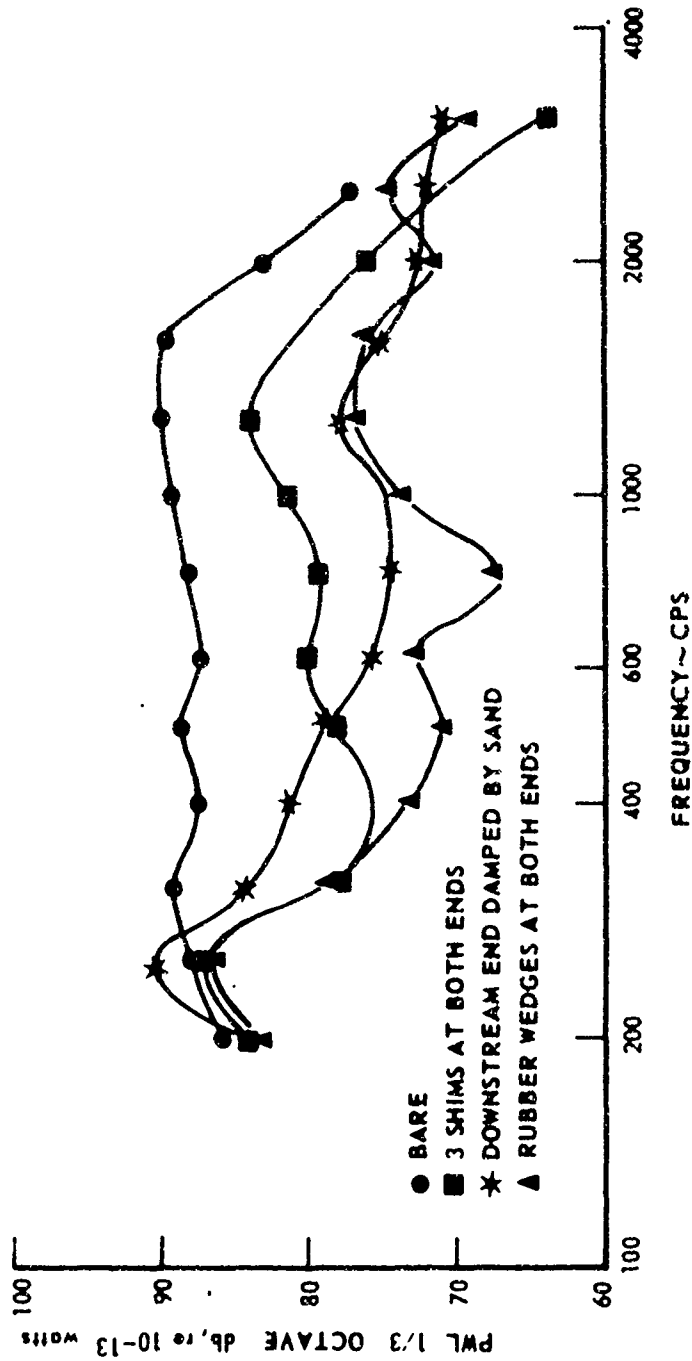


**Total Acoustic Power**  
(36 IN. X 6.5 IN. PANEL)

FIGURE 27



CALC			REVISED	DATE	TOTAL ACOUSTIC POWER (36" X 6.5" PANEL)	D6-9944 - VOL. III
CHECK						FIG. 28
APPD						PAGE
APPD						78
					THE <b>BOEING</b> COMPANY RENTON WASHINGTON	



Sound Power Level For  
36" x 6.5" x .040"  
Panel At M-- 0.47

FIGURE 29

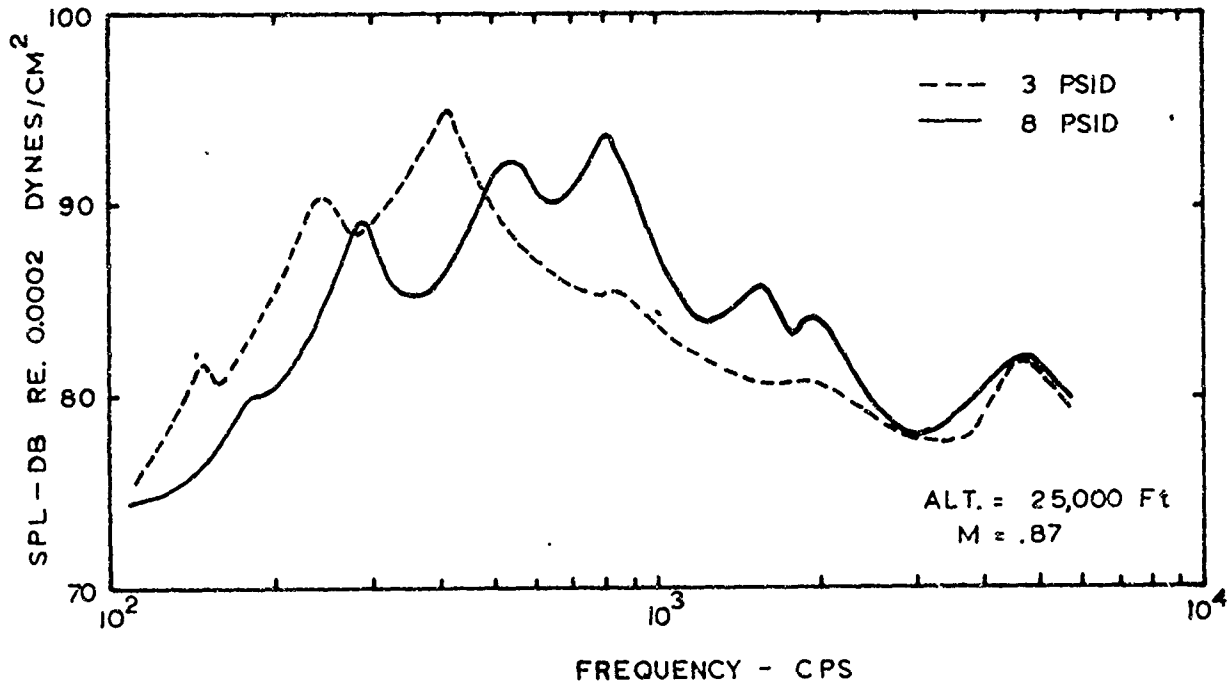
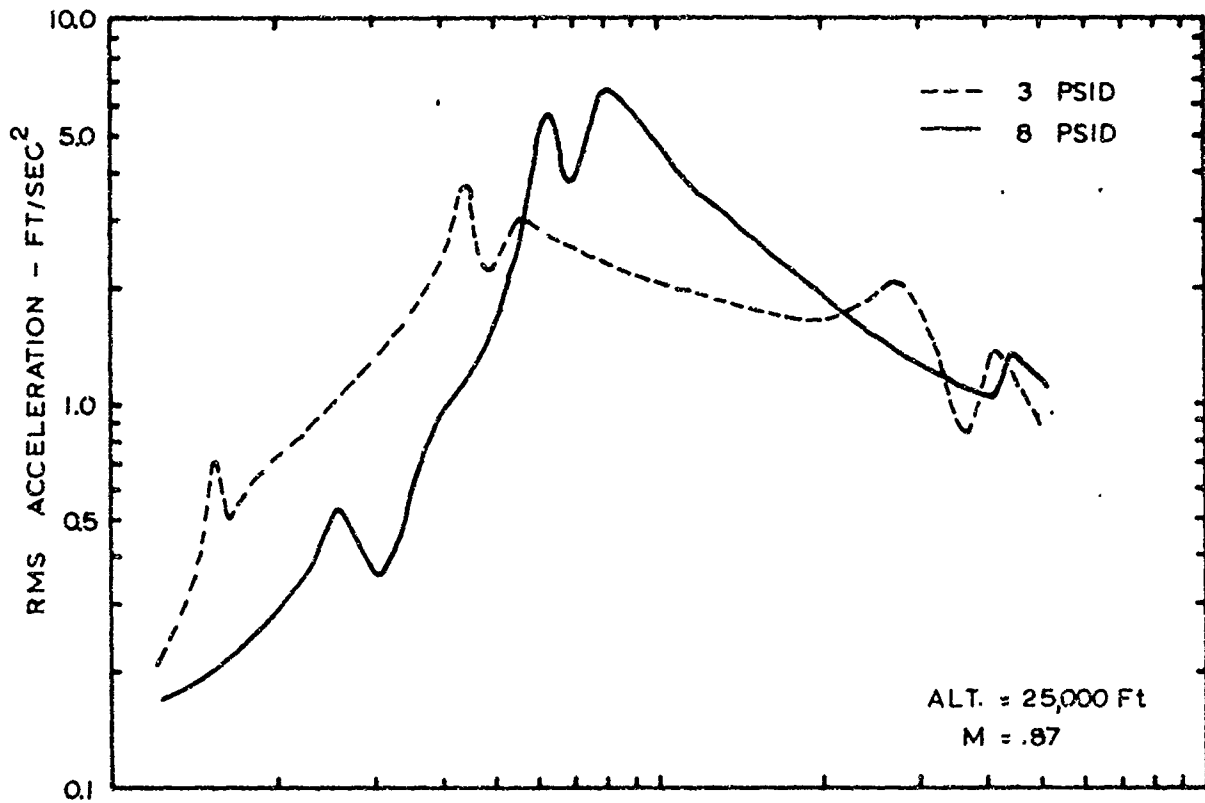


6A69080

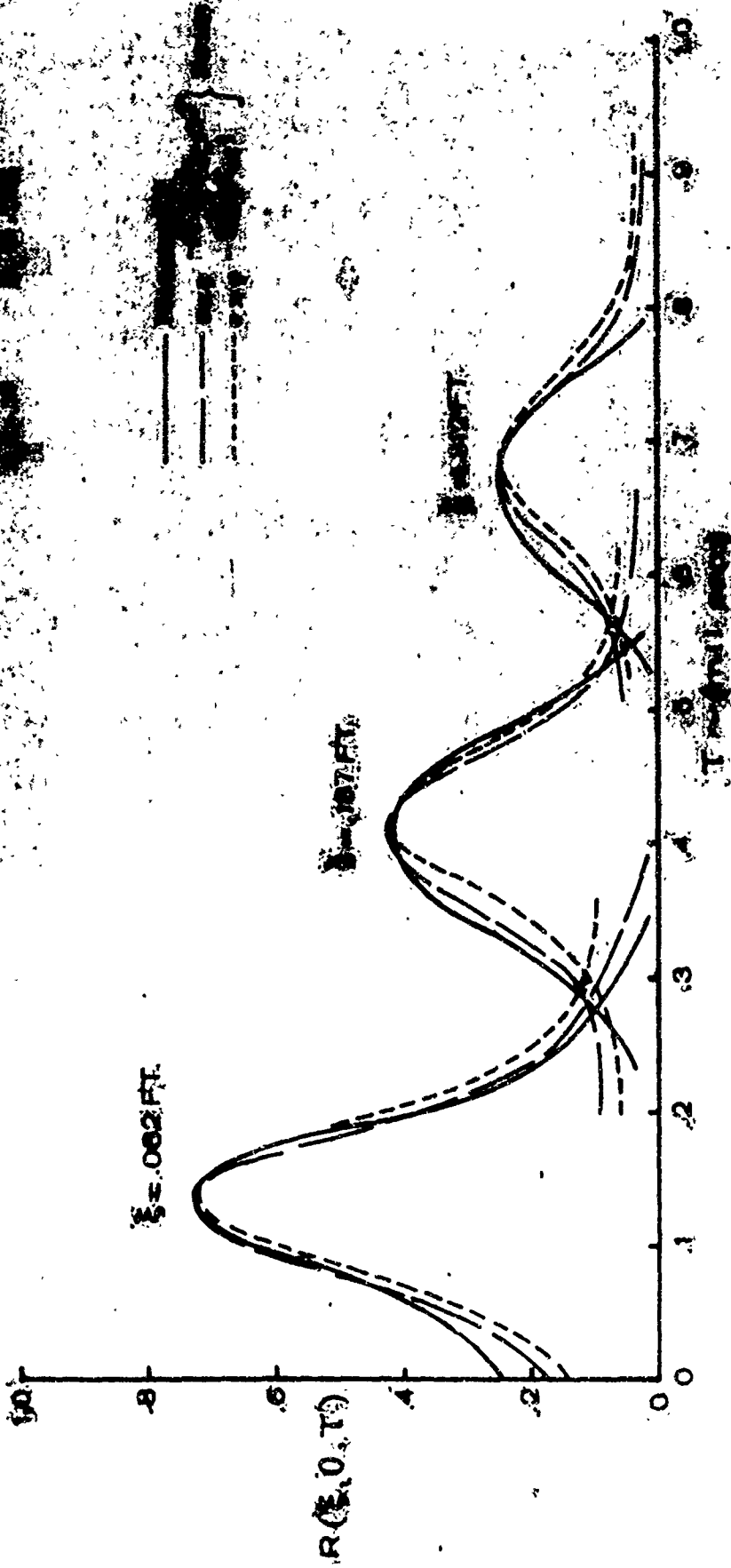
36"x6.5"x.040" Panel With Rubber Wedges

FIGURE 30  
SHEET 80

720 AIRPLANE



CALC			REVISED	DATE	EFFECTS OF CABIN PRESSURIZATION ON SPL AND SKIN ACCELERATION	DF-9944 - VOL. III
CHECK						FIG. 31
APPD						PAGE
APPD						81
					THE <b>BOEING</b> COMPANY RENTON WASHINGTON	



SPACE - TIME CORRELATION OF THE WAVE FUNCTION

TABLE I

EIGENVALUES FOR 36.0" x 6.5" PANELS WITH A RIGID BOUNDARY  
(REF 34)

$$\phi_1(y) = \cos \frac{3\pi}{2} \left( \frac{y}{6.5} - \frac{1}{2} \right) + (1.34 \times 10^{-1}) \cosh \frac{3\pi}{2} \left( \frac{y}{6.5} - \frac{1}{2} \right)$$

$$\phi_2(y) = \sin \frac{5\pi}{2} \left( \frac{y}{6.5} - \frac{1}{2} \right) + (2.79 \times 10^{-2}) \sinh \frac{5\pi}{2} \left( \frac{y}{6.5} - \frac{1}{2} \right)$$

$$\phi_3(y) = \cos \frac{7\pi}{2} \left( \frac{y}{6.5} - \frac{1}{2} \right) - (5.79 \times 10^{-3}) \cosh \frac{7\pi}{2} \left( \frac{y}{6.5} - \frac{1}{2} \right)$$

$$\theta_1(x) = \cos \frac{3\pi}{2} \left( \frac{x}{36} - \frac{1}{2} \right) + (1.34 \times 10^{-1}) \cosh \frac{3\pi}{2} \left( \frac{x}{36} - \frac{1}{2} \right)$$

$$\theta_2(x) = \sin \frac{5\pi}{2} \left( \frac{x}{36} - \frac{1}{2} \right) + (2.79 \times 10^{-2}) \sinh \frac{5\pi}{2} \left( \frac{x}{36} - \frac{1}{2} \right)$$

$$\theta_3(x) = \cos \frac{7\pi}{2} \left( \frac{x}{36} - \frac{1}{2} \right) - (5.79 \times 10^{-3}) \cosh \frac{7\pi}{2} \left( \frac{x}{36} - \frac{1}{2} \right)$$

$$\theta_4(x) = \sin \frac{9\pi}{2} \left( \frac{x}{36} - \frac{1}{2} \right) - (1.20 \times 10^{-3}) \sinh \frac{9\pi}{2} \left( \frac{x}{36} - \frac{1}{2} \right)$$

$$\theta_5(x) = \cos \frac{11\pi}{2} \left( \frac{x}{36} - \frac{1}{2} \right) + (2.50 \times 10^{-4}) \cosh \frac{11\pi}{2} \left( \frac{x}{36} - \frac{1}{2} \right)$$

$$\theta_6(x) = \sin \frac{13\pi}{2} \left( \frac{x}{36} - \frac{1}{2} \right) + (5.20 \times 10^{-5}) \sinh \frac{13\pi}{2} \left( \frac{x}{36} - \frac{1}{2} \right)$$

$$\theta_7(x) = \cos \frac{15\pi}{2} \left( \frac{x}{36} - \frac{1}{2} \right) - (1.08 \times 10^{-5}) \cosh \frac{15\pi}{2} \left( \frac{x}{36} - \frac{1}{2} \right)$$

$$\theta_8(x) = \sin \frac{17\pi}{2} \left( \frac{x}{36} - \frac{1}{2} \right) - (2.25 \times 10^{-6}) \sinh \frac{17\pi}{2} \left( \frac{x}{36} - \frac{1}{2} \right)$$

$$\theta_9(x) = \cos \frac{19\pi}{2} \left( \frac{x}{36} - \frac{1}{2} \right) + (4.07 \times 10^{-7}) \cosh \frac{19\pi}{2} \left( \frac{x}{36} - \frac{1}{2} \right)$$

$$\theta_{10}(x) = \sin \frac{21\pi}{2} \left( \frac{x}{36} - \frac{1}{2} \right) + (9.72 \times 10^{-8}) \sinh \frac{21\pi}{2} \left( \frac{x}{36} - \frac{1}{2} \right)$$

$$\theta_{11}(x) = \cos \frac{23\pi}{2} \left( \frac{x}{36} - \frac{1}{2} \right) - (2.12 \times 10^{-8}) \cosh \frac{23\pi}{2} \left( \frac{x}{36} - \frac{1}{2} \right)$$

$$\theta_{12}(x) = \sin \frac{25\pi}{2} \left( \frac{x}{36} - \frac{1}{2} \right) - (4.12 \times 10^{-9}) \sinh \frac{25\pi}{2} \left( \frac{x}{36} - \frac{1}{2} \right)$$

$$\theta_{13}(x) = \cos \frac{27\pi}{2} \left( \frac{x}{36} - \frac{1}{2} \right) + (8.73 \times 10^{-10}) \cosh \frac{27\pi}{2} \left( \frac{x}{36} - \frac{1}{2} \right)$$

$$\theta_{14}(x) = \sin \frac{29\pi}{2} \left( \frac{x}{36} - \frac{1}{2} \right) + (1.81 \times 10^{-10}) \sinh \frac{29\pi}{2} \left( \frac{x}{36} - \frac{1}{2} \right)$$

$$\theta_{15}(x) = \cos \frac{31\pi}{2} \left( \frac{x}{36} - \frac{1}{2} \right) - (3.77 \times 10^{-11}) \cosh \frac{31\pi}{2} \left( \frac{x}{36} - \frac{1}{2} \right)$$

$$\theta_{16}(x) = \sin \frac{33\pi}{2} \left( \frac{x}{36} - \frac{1}{2} \right) - (7.84 \times 10^{-12}) \sinh \frac{33\pi}{2} \left( \frac{x}{36} - \frac{1}{2} \right)$$

$$\theta_{17}(x) = \cos \frac{35\pi}{2} \left( \frac{x}{36} - \frac{1}{2} \right) + (1.63 \times 10^{-12}) \cosh \frac{35\pi}{2} \left( \frac{x}{36} - \frac{1}{2} \right)$$

$$\theta_{18}(x) = \sin \frac{37\pi}{2} \left( \frac{x}{36} - \frac{1}{2} \right) + (3.39 \times 10^{-13}) \sinh \frac{37\pi}{2} \left( \frac{x}{36} - \frac{1}{2} \right)$$

$$\theta_{19}(x) = \cos \frac{39\pi}{2} \left( \frac{x}{36} - \frac{1}{2} \right) - (7.04 \times 10^{-14}) \cosh \frac{39\pi}{2} \left( \frac{x}{36} - \frac{1}{2} \right)$$

$$\theta_{20}(x) = \sin \frac{41\pi}{2} \left( \frac{x}{36} - \frac{1}{2} \right) - (1.46 \times 10^{-14}) \sinh \frac{41\pi}{2} \left( \frac{x}{36} - \frac{1}{2} \right)$$